AD-A084 261 PURDUE UNIV LAFAYETTE IN TURNER LAB FOR ELECTROCERAMICS F/G 9/1
THE EFFECTS OF SUBSTRATE COMPOSITION OF THICK FILM CIRCUIT RELI--ETC(U)
FEB 80 R W VEST N00019-79-C-0240
UNCLASSIFIED NL

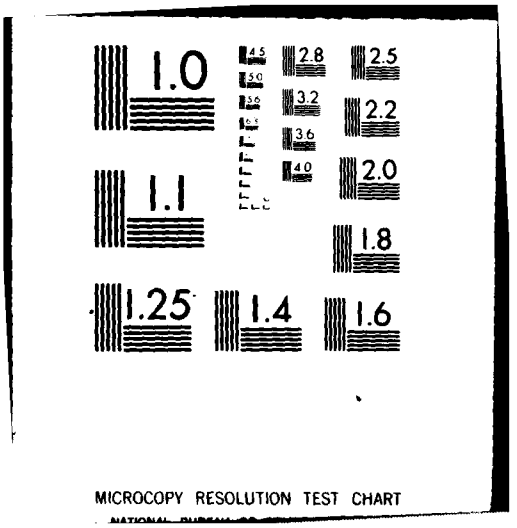
1.0
1.1
1.25
1.4
1.6
1.8
2.0
2.2
2.5
2.8
3.2
3.6
4.0
4.5
5.0
MICROCOPY RESOLUTION TEST CHART

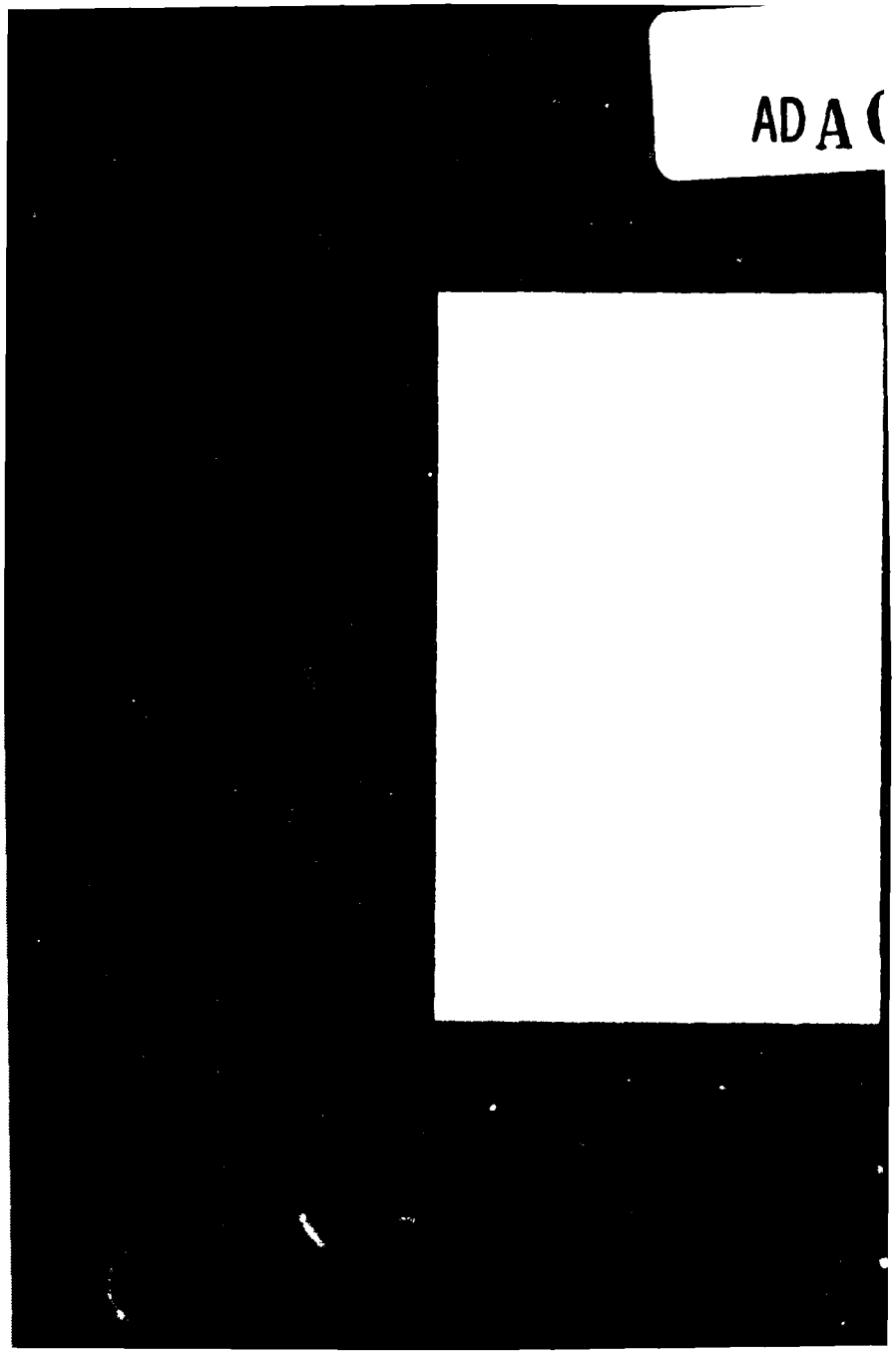
AD A

Accession For
NTIS GRA&I
DDC TAB
Unannounced
Justification
By
Distribution/
Availability Codes
Dist. | Avail and/or special
A

LEVEL II

THE EFFECTS OF SUBSTRATE COMPOSITION ON THICK FILM CIRCUIT RELIABILITY

R. W. Vest

28 February 1980

Final Technical Report

For the period 2/1/79-1/31/80

Contract No. N00019-79-C-0240

Prepared for

NAVAL AIR SYSTEMS COMMAND

DTIC
ELECTE
S MAY 19 1980 D
D

APPROVED FOR PUBLIC RELEASE;
DISTRIBUTION UNLIMITED

FOREWORD

Research described in this report constitutes one year of effort under Contract No. N00019-79-C-0240 with the Naval Air Systems Command, Department of the Navy, under the technical cognizance of James Willis. The research was conducted in the Turner Laboratory for Electroceramics, School of Materials Engineering and School of Electrical Engineering, Purdue University, West Lafayette, Indiana 47907, under the direction of Professor R. W. Vest. Contributing to the project were Messrs. J. M. Himelick, P. Palanisamy, R. L. Reed and C-T Tarn.

SECURITY CLASSIFICATION OF THIS PAGE (When Data Entered)

REPORT DOCUMENTATION PAGE

READ INSTRUCTIONS BEFORE COMPLETING FORM

1. REPORT NUMBER

2. GOVT ACCESSION NO. AD-A084 262

3. RECIPIENT'S CATALOG NUMBER (9)

4. TITLE (and Subtitle) (6)
THE EFFECTS OF SUBSTRATE COMPOSITION ON THICK FILM CIRCUIT RELIABILITY

5. TYPE OF REPORT & PERIOD COVERED
Final Rept.
~~2/1/79-1/31/79~~ 1 Feb - 31 Jan 79

6. PERFORMING ORG. REPORT NUMBER

7. AUTHOR(s) (10)
R. W. Vest

8. CONTRACT OR GRANT NUMBER(s) (15)
N00019-79-C-0240

9. PERFORMING ORGANIZATION NAME AND ADDRESS
PURDUE RESEARCH FOUNDATION, PURDUE UNIVERSITY
West Lafayette, Indiana 47907

10. PROGRAM ELEMENT, PROJECT, TASK AREA & WORK UNIT NUMBERS

11. CONTROLLING OFFICE NAME AND ADDRESS (11)
NAVAL AIR SYSTEMS COMMAND, AIR 310B
Washington, D.C. 20361

12. REPORT DATE
28 February 1980

13. NUMBER OF PAGES
107

14. MONITORING ~~AGENCY NAME~~ & ADDRESS (if different from Controlling Office) (12) 119

15. SECURITY CLASS. (of this report)
Unclassified

15a. DECLASSIFICATION/DOWNGRADING SCHEDULE
N/A

16. DISTRIBUTION STATEMENT (of this Report)

APPROVED FOR PUBLIC RELEASE:
DISTRIBUTION UNLIMITED

17. DISTRIBUTION STATEMENT (of the abstract entered in Block 20, if different from Report)

18. SUPPLEMENTARY NOTES

19. KEY WORDS (Continue on reverse side if necessary and identify by block number)

Thick Film Resistors
Ceramic Substrates
Electrical Resistivity
Temperature Coefficient Resistivity
Electronic Glass

20. ABSTRACT (Continue on reverse side if necessary and identify by block number)

The dissolution of an alumina substrate (AlSiMag 614) into the glass phase of a thick film resistor during firing was found to markedly increase the viscosity, and to decrease the surface tension and density of the glass. These changes in glass properties cause an increase in the sheet resistance and a decrease in the TCR of the resistors. The minor constituents in the substrate were found to exert a larger effect on glass properties than their concentration (4%) suggests. The models for microstructure development and

DD FORM 1 JAN 73 1473 EDITION OF 1 NOV 65 IS OBSOLETE
S/N 0102-014-6601

SECURITY CLASSIFICATION OF THIS PAGE (When Data Entered)

410 421

Abstract continued

charge transport in thick film resistors were modified in order to accommodate the effect of the resistor-substrate interaction. The results of this study led to specific recommendations for quality control of substrate chemistry, and for composition of resistor glasses.

TABLE OF CONTENTS

		Page
1.	INTRODUCTION	1
	1.1 General	1
	1.2 Previous Work	1
	1.3 Experimental Materials	3
2.	MICROSTRUCTURE DEVELOPMENT	7
	2.1 High Temperature Viscosity of Glasses	7
	2.1.1 Experimental	7
	2.1.2 Results and Analysis	9
	2.1.3 Influence of Minor Constituents of the Substrate	15
	2.2 Surface Tension of Glasses	17
	2.2.1 Experimental	17
	2.2.2 Results and Analysis	18
	2.3 Density of Glasses	21
	2.4 RuO_2 Ripening	25
	2.4.1 Experimental	25
	2.4.2 Results and Analysis	26
	2.5 RuO_2 Sintering	35
	2.5.1 General	35
	2.5.2 Model and Analysis	35
	2.6 Substrate-Resistor Interactions	42
	2.7 Microstructure Development Model	48
3.	ELECTRICAL EFFECTS	58
	3.1 Resistor Studies	58
	3.2 MIM Studies	65
	3.2.1 General	65
	3.2.2 Fabrication	66
	3.2.3 Anneal Experiments	69
	3.2.4 AC Conductivity and Dissipation Factor	70
	3.2.5 Dielectric Constant and Breakdown	76
	3.2.6 DC Experiments	78

TABLE OF CONTENTS (continued)

	Page
3.2.6.1 Experimental	78
3.2.6.2 Results and Analysis	79
3.3 Charge Transport Model	97
4. SUMMARY AND RECOMMENDATIONS	103
5. REFERENCES	106

LIST OF FIGURES

Figure		Page
2.1	Sphere Viscometer (Schematic)	8
2.2	Viscosity of Glasses Containing Dissolved Substrate, Alumina and NBS Reference Glass	11
2.3	Arrhenius Plot of High Temperature Viscosity of Glasses Containing Dissolved Substrate and Alumina	12
2.4	Effects of Composition and Temperature on Glass Viscosity	14
2.5	Surface Tension of Standard Glass with Various Amounts of Dissolved Alumina and Substrate	19
2.6	Comparison of Measured Viscosities (Lines) with Viscosities Calculated from Sintering Data (Points) . . .	22
2.7	Variation of Glass Density with Composition and Temperature	23
2.8	Ripening of RuO_2 in Glasses at 950°C	27
2.9	RuO_2 Ripening in Glasses at 888°C	29
2.10	RuO_2 Ripening in Glasses at 950°C	30
2.11	RuO_2 Ripening in Glasses at 1000°C	31
2.12	Variation of $C_o\gamma_{sl}K_T$ with Composition and Temperature . .	33
2.13	Liquid-Phase Sintering Model with a Solid-Solid Contact, Completely Immersed in a Liquid	36
2.14	Geometry of Neck Between Particles Undergoing Liquid-Phase Sintering	38
2.15	Comparison of Theory and Experiment for the Dissolution of AlSiMag 614 Substrate in Printed and Fired 5 w/o RuO_2 Resistors (solid lines calculated from Eq. 2.29)	46
2.16	Variation of Resistor Glass Composition with Time and Temperature for Different Initial Composition Glasses . .	47
3.1	Temperature Dependence of Standard Glass Resistors Fired at 800°C	61

LIST OF FIGURES (continued)

Figure		Page
3.2	Temperature Dependence of 4 w/o Substrate Glass Resistors Fired at 800°C	62
3.3	Temperature Dependence of 6 w/o Substrate Glass Resistors Fired at 800°C	63
3.4	Temperature Dependence of 10 w/o Substrate Glass Resistors Fired at 800°C	64
3.5	Parallel Conductivity as a Function of Frequency and Film Thickness for Standard Glass Devices	71
3.6	Parallel Conductivity as a Function of Frequency and Film Thickness for 10 w/o Substrate Glass Devices	72
3.7	Dissipation Factor as a Function of Frequency and Film Thickness for Standard Glass Devices	74
3.8	Dissipation Factor as a Function of Frequency and Film Thickness for 10 w/o Substrate Glass Devices	75
3.9	Current Density as a Function of Voltage for a Standard Glass (15 nm) MIM at 25°C	80
3.10	Current Density as a Function of Voltage for a 10 w/o Substrate Glass (13 nm) MIM at 25°C	81
3.11	Current Density as a Function of Voltage for a 10 w/o Substrate Glass MIM with an Aluminum Top Electrode at 25°C	82
3.12	Current Density as a Function of Voltage for a Standard Glass MIM (15 nm) Before and After Annealing . .	84
3.13	Current Density as a Function of Voltage for Two Standard Glass (10 nm) MIMs Annealed at 380°C	85
3.14	Current Density as a Function of Voltage for a 10 w/o Substrate Glass (13 nm) MIM at Two Temperatures .	86
3.15	Current Density as a Function of Temperature for a 10 w/o Substrate Glass (13 nm) MIM at Four Voltages . . .	87
3.16	Current Density as a Function of Voltage for a 10 w/o Substrate Glass (9.5 nm) MIM at Three Temperatures	89

LIST OF FIGURES (continued)

Figure		Page
3.17	Current Density as a Function of Temperature for a 10 w/o Substrate Glass (9.5 nm) MIM at Three Voltages	90
3.18	Current Density as a Function of Voltage for a 10 w/o Substrate Glass (7 nm) MIM at Three Temperatures	91
3.19	Current Density as a Function of Temperature for a 10 w/o Substrate Glass (7 nm) MIM at Five Voltages . . .	92
3.20	Current Density as a Function of Voltage for a 10 w/o Substrate Glass (7 nm) MIM at Two Temperatures . .	93
3.21	Current Density as a Function of Temperature for a 10 w/o Substrate Glass (7 nm) MIM at 0.5 Volt	95
3.22	TCR at 25°C as a Function of Firing Time at 800°C for Four Resistor Glass Compositions	102

LIST OF TABLES

Tables		Page
I.1	Composition of AlSiMag 614 Substrate	4
I.2	Properties of AlSiMag 614 Substrate	5
II.1	Fulcher Equation Fit for Glass Viscosity (10 - 10^5 Pa·s).	13
II.2	Fulcher Equation Fit for Glass Viscosity (10 - 10^{13} Pa·s)	16
II.3	Variation of K_T with Composition and Temperature	34
II.4	Calculated Initial Stage Neck Growth Kinetics of RuO_2 in the Standard Glass	41
II.5	Dependence of Neck Size on Particle Size and Temperature	43
II.6	Summary of Glass Properties	52
III.1	Volume Percent Conductive in 5 w/o RuO_2 Resistors	59
III.2	Dielectric Constant and Dielectric Breakdown	77

1. INTRODUCTION

1.1 General

The print and fire processing of thick film circuits ensures that there always will be some degree of chemical interaction between the film and the substrate, because all common substrate materials are soluble to some degree in the glasses used in thick film inks. This interaction is primarily responsible for the development of adhesion between the thick film and the substrate, but it also leads to changes in the composition of the glass with the net result that the physical properties of the glass will change. These changes in physical properties of the glass will result in modified kinetics for the various microstructure development processes and all electrical properties of the resistors are related to the microstructure. The goal of this research program was to develop a sufficient level of understanding of the phenomena involved in the substrate-glass interaction so that appropriate models could be developed.

1.2 Previous Work

Previously reported studied [1-3] under this program established the magnitude of the effects resulting from chemical interaction between a thick film resistor and a ceramic substrate, and determined the specific influence on certain important properties of the resistor glass. The rates of dissolution of two substrates, 96% Al_2O_3 (AlSiMag 614) and 99.5% Al_2O_3 (AlSiMag 772), in two lead borosilicate glasses (63 w/o PbO-25 w/o B_2O_3-12 w/o SiO_2 and 70 w/o PbO-20 w/o B_2O_3-10 w/o SiO_2) were measured at various temperatures. The rate limiting steps for each substrate-glass system were determined in all appropriate temperature ranges, and emperical

equations were developed to predict the substrate recession as a function of time and temperature for thick film resistors. The saturation solubility of AlSiMag 614 substrates in 63-25-12 glass was determined as a function of temperature, and these results were combined with the dissolution rate studies in order to test various kinetic models.

Studies of the kinetics of initial stage sintering of glass particles were conducted in order to determine the ratio of surface tension to viscosity for the two standard glasses, and the standard glasses with additions of substrate ingredients. Both the magnitude and the activation energies of this ratio were found to be significantly different for the gasses, confirming the extreme sensitivity of this parameter to small changes in glass composition.

The viscosity of the 63-25-12 glass was measured as a function of amount of dissolved AlSiMag 614 substrate from the softening point to the annealing point. The isothermal viscosity was found to increase by a factor of 20 with 10 w/o dissolved substrate relative to the standard lead borosilicate glass.

The sheet resistance, temperature dependence of resistance, and the current noise were measured for thick film resistors as a function of the amount of substrate dissolved in the resistor for various firing temperatures at 10 minutes firing time, and for various firing times at 800°C. Large variations in these three properties were observed, and the changes were qualitatively correlated with changes in viscosity of the glass. The microstructure development and charge transport models used to correlate the results indicated a retardation of microstructure development in the resistors as the amount of dissolved substrate increased which led to

changing proportions of sintered and non-sintered contacts in the RuO_2 networks within the body of the resistor.

1.3 Experimental Materials

The substrate used in this work was AlSiMag 614, a 96 w/o alumina ceramic consisting of minor quantities of fluxes. The chemical constitution of the substrate is given in Table I.1. The physical, mechanical, thermal, and electrical characteristics of the substrate are summarized in Table I.2. The substrate was found to be quite inert to concentrated HCl, the average weight loss for a 4 hour ultrasonic treatment of the substrate with the acid being 0.1 mg. The substrate, prior to use, was cleaned ultrasonically with concentrated hydrochloric acid, washed with deionized water, and rinsed with acetone.

A lead borosilicate glass composition consisting of 63 w/o PbO, 25 w/o B_2O_3, and 12 w/o SiO_2 is referred to as the standard glass in this work. The standard glass was prepared by mixing and melting the appropriate qualtities of red lead (Pb_3O_4), boric acid (H_3BO_3), and silica (SiO_2) in a platinum evaporating dish. The substrate and the alumina doped glasses were fabricated by mixing and melting the desired proportions of the standard glass along with powdered substrate or alumina. The UHP red lead* had a purity of 99.99%, and the boric acid, the silica, and the alumina were of reagent grade. The decomposition of boric acid into B_2O_3 and H_2O during glass making caused boron loss, because the escaping moisture tends to carry a small amount of B_2O_3 away. In order to account for the losses, a procedure for the wet chemical analysis of lead, boron, silicon, and

---

* Hammond Lead Products, Inc., Hammond, Indiana

TABLE I.1. Composition of AlSiMag 614 Substrate

Constituent	Weight Percent	
	Typical*	Analyzed**
Al_2O_3	96.0	94.7
SiO_2	2.8	3.6
MgO	0.82	1.31
CaO	0.17	0.1
Fe_2O_3	0.09	0.2
Na_2O	0.06	0.001
K_2O	0.03	0.008
TiO_2	0.03	0.02
BaO	--	0.008
Cr_2O_3	--	0.003
Ga_2O_3	--	0.03
Mn_2O_3	--	0.001
ZrO_2	--	0.003

* A typical analysis according to the manufacturer, 3M Company of St. Paul, Minnesota.

** Bulk chemical analyses of the same lot of ceramic at RCA Laboratories, Princeton, New Jersey.

TABLE I.2. Properties of AlSiMag 614 Substrate.

Property		Unit		Value			
Water Absorption		%		0			
Specific Gravity		---		3.70			
Hardness		Moh's Scale		9			
		Rockwell 65 N		78			
Tensile Strength		Psi kg/cm^2		25 000	1 760		
Compressive Strength		Psi Kg/cm		375 000	26 360		
Flexural Strength		Psi kg/cm		46 000	3 230		
Resistance to Impact		Inch-lbs. Meter-Kg		7.0	.081		
Modulus of Elasticity		Psi kg/cm^2		47X10^6	3.30X10^6		
Shear Modulus		Psi kg/cm^2		19X10^6	1.34X10^6		
Poisson's Ratio		---		.22			
Thermal Expansion Linear Coefficient		Per °C	25-300°C	6.4X10^{-6}			
			25-700°C	7.5X10^{-6}			
			25-900°C	7.0X10^{-6}			
Thermal Conductivity	25°C	BTU in. / nr. ft^2 F	Cal. cm / s. cm^2 °C	244	.084		
	300°C			119	.041		
	500°C			75	.026		
	800°C			58	.020		
Volume Resistivity	25°C	Ohm-centimeters		> 10^{14}			
	100°C			2.0X10^{13}			
	300°C			1.1X10^{10}			
	500°C			7.3X10^7			
	700°C			3.5X10^6			
	900°C			6.8X10^5			
Dielectric Strength 60 Hertz AC Test Discs 1/4" thick		volts per mil	kilovolts per mm	210	8.3		
				25°C	300°C	500°C	800°C
Dielectric Constant	1 MHz		---	9.3	9.5	10.8	22.4
Dissipation Factor	1 MHz		---	.0003	.0027	.0131	.0911
Loss Factor	1 MHz		---	.0028	.0257	.1415	2.041

aluminum was developed. By comparing the weighed out composition and the analyzed composition, the boron loss was determined, and the loss was compensated for in the subsequent glass fabrications. The molten glass was then poured into a stainless steel beaker filled with deionized water to frit it. The fritted glasses were crushed in a vibratory agate ball mill until they would pass through a 325 mesh (47μm) screen.

For the RuO_2 ripening studies, a 65.6 m^2/gm lot was obtained from Engelhard.* The RuO_2 used in the formulation of resistor pastes was prepared by drying the ruthenium dioxide hydrate ($RuO_2 \cdot XH_2O$) also obtained from Engelhard. The hydrate was dried in an oven according to a temperature-time profile developed on the basis of differential thermal analysis and thermogravimetric analysis. The dehydration of the hydrate is exothermic, and therefore caution must be exercised to avoid a spontaneous reaction during the dehydration process. The average particle size of the RuO_2 was determined by surface area measurements discussed in Section 2.4.1. Particle shape and approximate size were also obtained by SEM studies. Samples for the SEM studies were prepared by ultrasonically dispersing the powder in methanol, placing a drop of the liquid on an aluminum block, and then letting it dry.

The resistor formulations used in this work were prepared by blending the required quantities of RuO_2 powder, glass powder, and the screening agent. The screening agent was a solution of 10 w/o N-300 ethyl cellulose** in butyl carbitol (diethylene glycol monobutyl ether). The formulations were made by adding approximately 60 v/o of the inorganics to 40 v/o of the screening agent, and thoroughly blending the mixture on a roll mill.

---

* Engelhard Minerals & Chemicals Corp., Newark, New Jersey

** Hercules Incorporated, Wilmington, Delaware

2. MICROSTRUCTURE DEVELOPMENT

2.1 High Temperature Viscosity of Glasses

2.1.1 Experimental

The high temperature viscosity of glasses as a function of the amount of dissolved substrate was determined by the sphere method [4]. The velocity (v) of an inert sphere in a liquid due to a load (L) is related to the viscosity (η) of the liquid by

$$\eta = LgF_a/3v\pi d \qquad (2.1)$$

where

g = acceleration due to gravity

F_a = Faxen correction factor equal to

$[1 - 2.104(d/D) + 2.09(d/D)^3 - 0.95(d/D)^5]$

d = diameter of the sphere

D = diameter of the crucible

A gold sphere was used in this work due to its inertness towards the glasses and air, and because a gold sphere is easier to fabricate than a platinum sphere.

A schematic representation of the high temperature viscometer assembly is shown in Fig. 2.1. The gold sphere, 0.9 cm in diameter, was suspended from the sample pan of an automatic recording microbalance by means of a platinum wire. The balance had an automatic range of 100 milligrams and an accuracy of 10 micrograms. Weight changes less than a milligram were sensed by an LVDT, whose signal was proportional to the beam displacement, and the amplified signal was recorded as a function of time. The LVDT

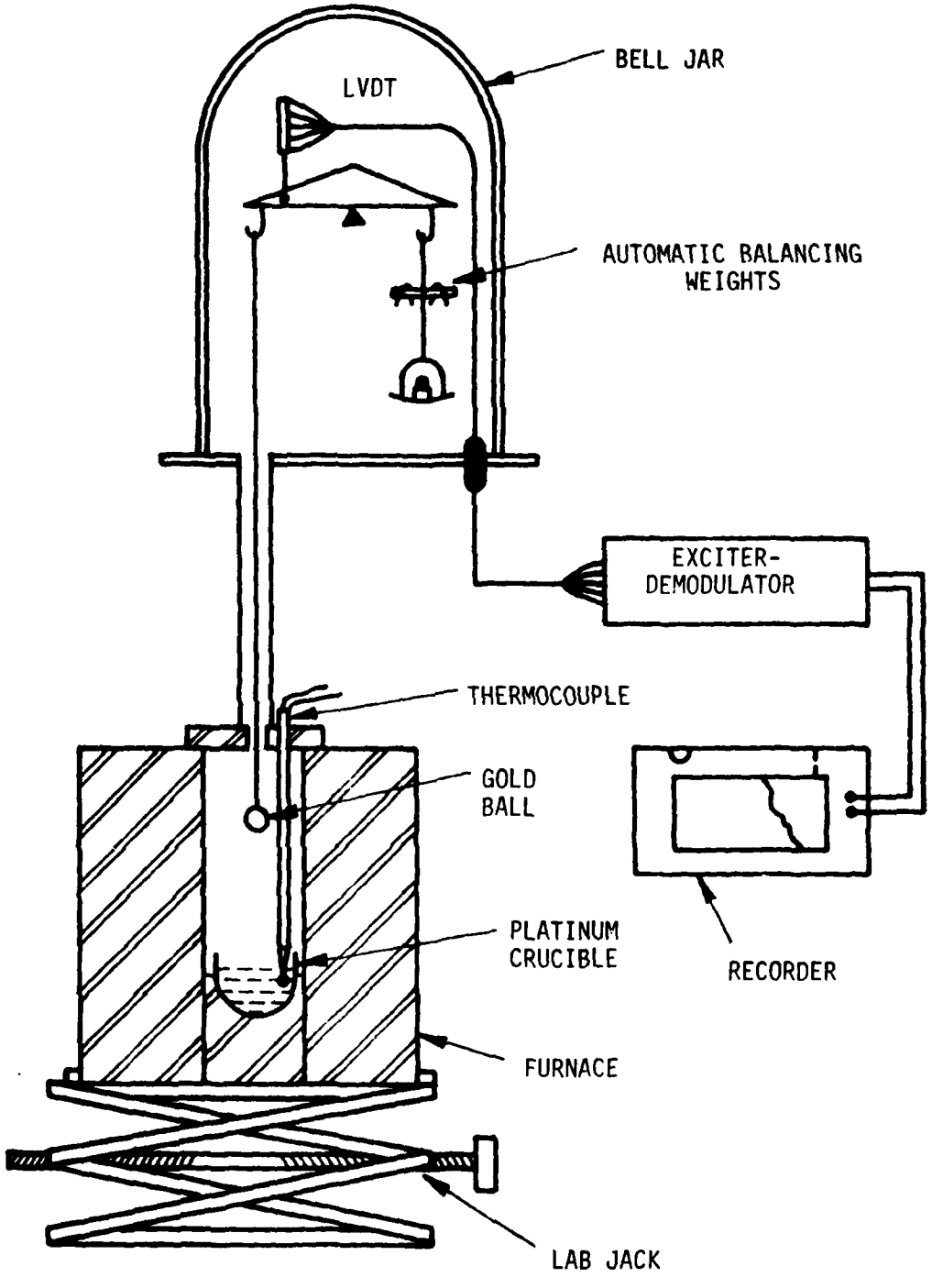

Figure 2.1. Sphere Viscometer (Schematic).

core was placed vertically on the balance beam, and its coil was supported independently so that the chart recorder could be calibrated from beam displacement. The experimental glass, contained in a platinum crucible 6.5 cm in diameter and 4.0 cm in depth, was placed in a pot furnace which could be positioned vertically by means of a jack. The glass temperature was measured by a Pt/Pt + 10% Rh thermocouple with the hot junction immersed in the glass.

To initiate a viscosity measurement, the glass sample was heated to 900°C and held for two hours to release entrapped air bubbles. The required temperature was then set, and sufficient time allowed to achieve thermal equilibrium. The furnace was raised until the gold sphere touched the glass as indicated by the deflection of the beam. The furnace was further raised until the sphere was immersed 0.5 cm below the glass level. After balancing to measure the weight of the sphere immersed in the glass, a net force, either upward or downward, was applied by either adding or removing a known amount of weight from the tare pan. The process was repeated for varying weights in order to obtain load versus velocity plots for both upward and downward movements of the ball. The average of the slopes of these lines was utilized in the viscosity calculations using Eq. 2.1. The reliability of the viscometer and the procedure was established by making measurements on a viscosity standard, NBS 711 glass, obtained from the National Bureau of Standards. All the viscosity measurements were made in ambient air with $P_{H_2O} \approx 2$ kPa.

2.1.2. Results and Analysis

The viscosity results of the Standard glass (63 w/o PbO-25 w/o B_2O_3-12 w/o SiO_2) along with 6, 10, and 14 w/o AlSiMag 614 substrate doped

glasses and 8 w/o Al_2O_3 doped glass, as well as the NBS 711 glass are shown in Fig. 2.2. The range of viscosity measured was from 10 to 10^5 Ps·s, and the temperature interval investigated from 580 to 850°C. The excellent agreement between the viscosity of NBS 711 glass determined in this work and that recommended by the Bureau is also shown in Fig. 2.2. The observation that the isothermal viscosities of the glass compositions increase with increase in substrate content is consistent with the low temperature beam bending viscosity results previously reported [3]. The difference in temperatures corresponding to a viscosity of 10^4 Pa·s for the standard and 14 w/o substrate glasses is about 75°C, whereas the difference at 10 Pa·s in about 250°C, indicating that the activation energy is a strong function of temperature for these glasses. The temperature dependence of viscosity is given as an Arrhenius plot in Fig. 2.3. The activation energy is seen to decrease with increasing temperature for all the glasses. A better fit of the data was obtained using the Fulcher equation [5], and the results of these calculations are given in Table II.1; the coefficients of determination (r^2) are better than .9998 and the standard deviations (σ) are small.

The viscosity-temperature characteristics of the standard glass + substrate system over the viscosity range of 10^{13} to 10 Pa·s determined by the beam bending and sphere methods are combined in Fig. 2.4. Only a few representative data points of the beam bending measurements and all the data from the sphere method were used in the construction of Fig. 2.4. Although neither of the two measurements could cover the 10^5 and 10^7 Pa·s range, the consistency of the two methods is excellent.

Least squares fits of the viscosity data over the 10-10^{13} Pa·s range to the Fulcher equation were performed, and the results are given in

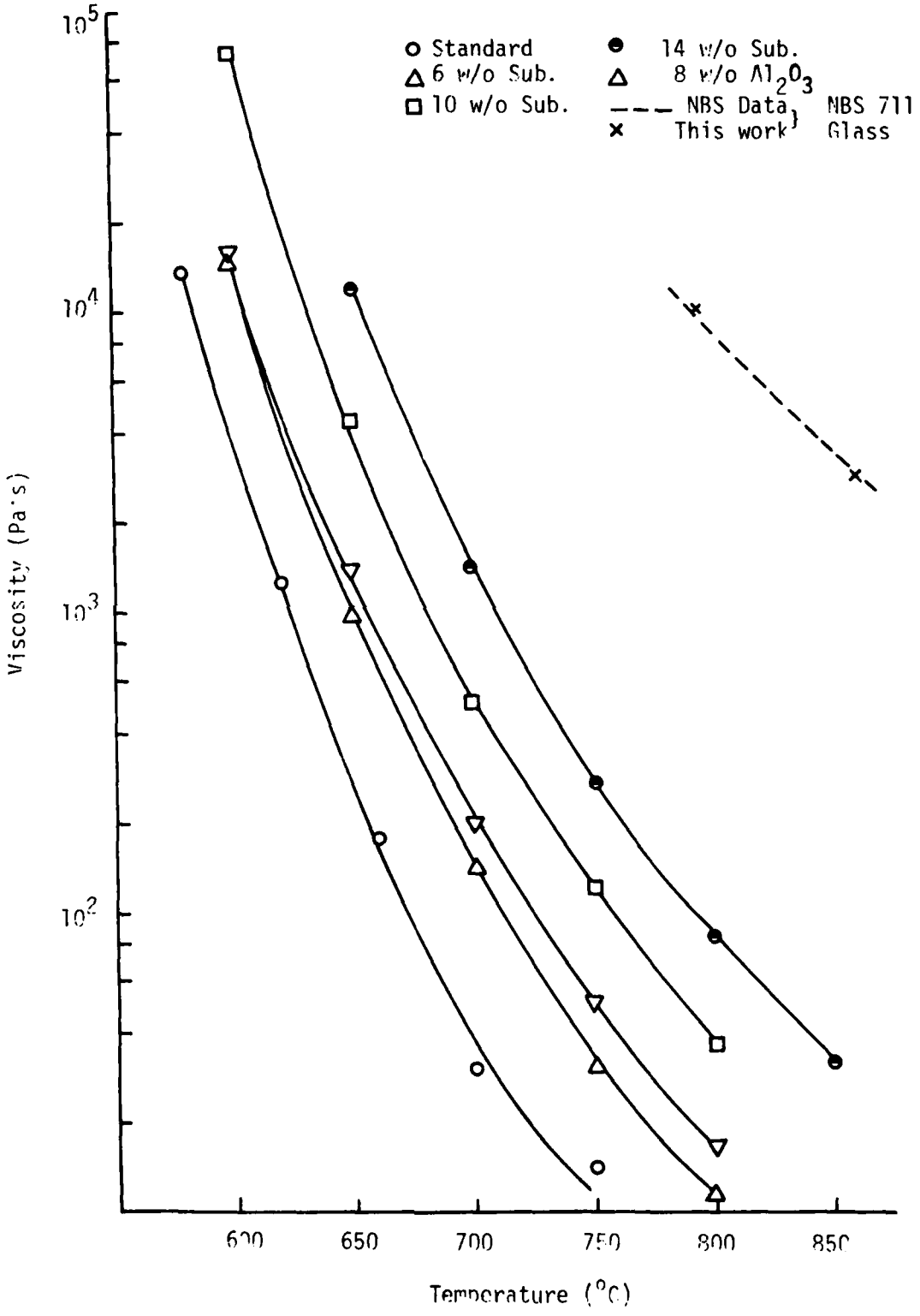

Figure 2.2. Viscosity of Glasses Containing Dissolved Substrate, Alumina and NBS Reference Glass

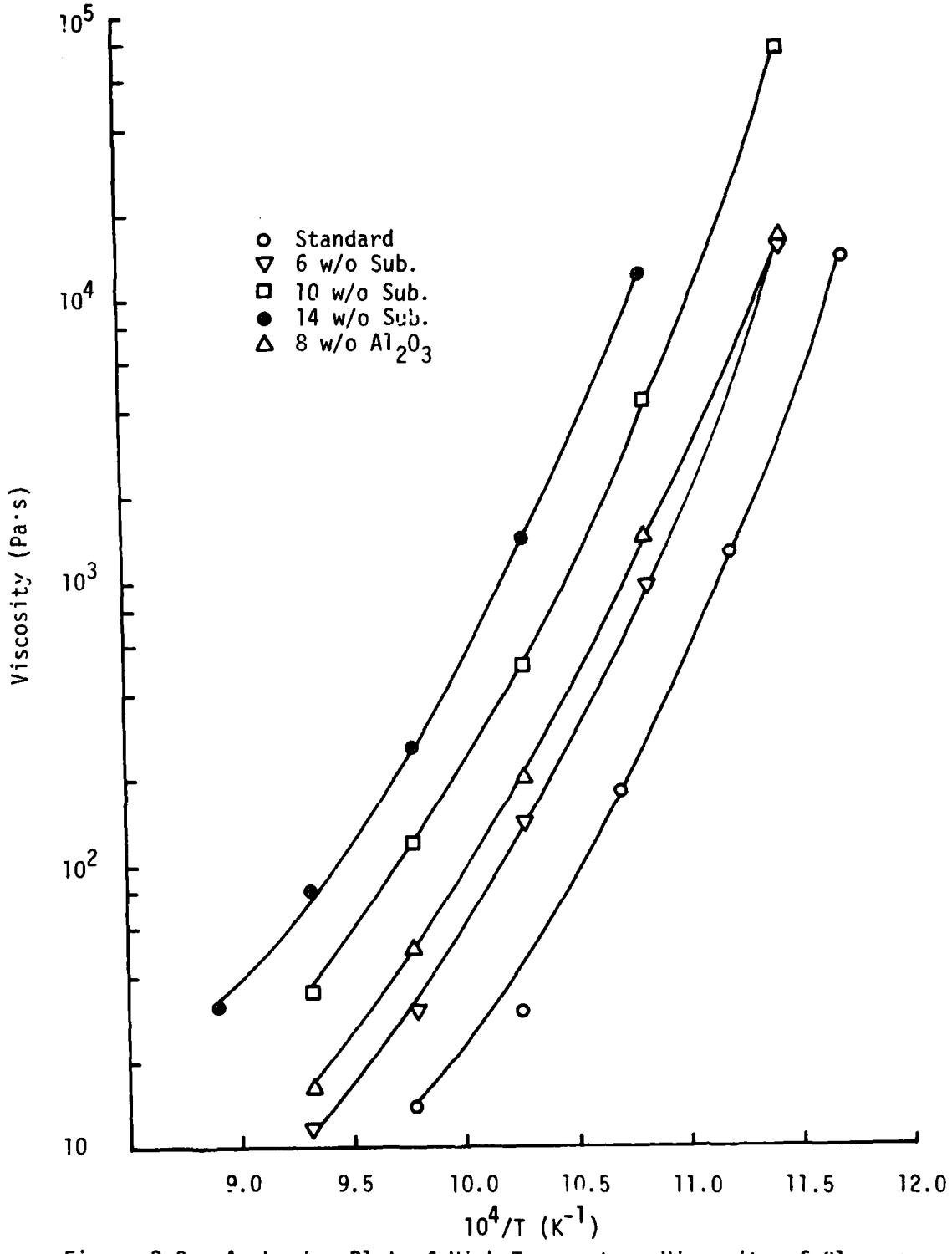

Figure 2.3. Arrhenius Plot of High Temperature Viscosity of Glasses Containing Dissolved Substrate and Alumina

TABLE II.1. Fulcher Equation Fit for Glass Viscosity
($10 - 10^5$ Pa·s)

$\text{Log } \eta = A'' + B''/(T - T_o)$ (η in Pa·s and T in K)

Composition	r^2	σ	A"	B"	T_o
Standard Glass	.9998	.0431	- 1.0010	615.695	736.69
6 w/o Sub. Glass	.9999	.0387	- 1.0026	716.243	737.78
10 w/o Sub. Glass	.9999	.0329	- 1.0022	945.335	714.44
14 w/o Sub. Glass	.9999	.0195	- 1.0011	1003.810	727.15
8 w/o Al_2O_3 Glass	.9998	.0428	- 1.0430	813.211	720.63

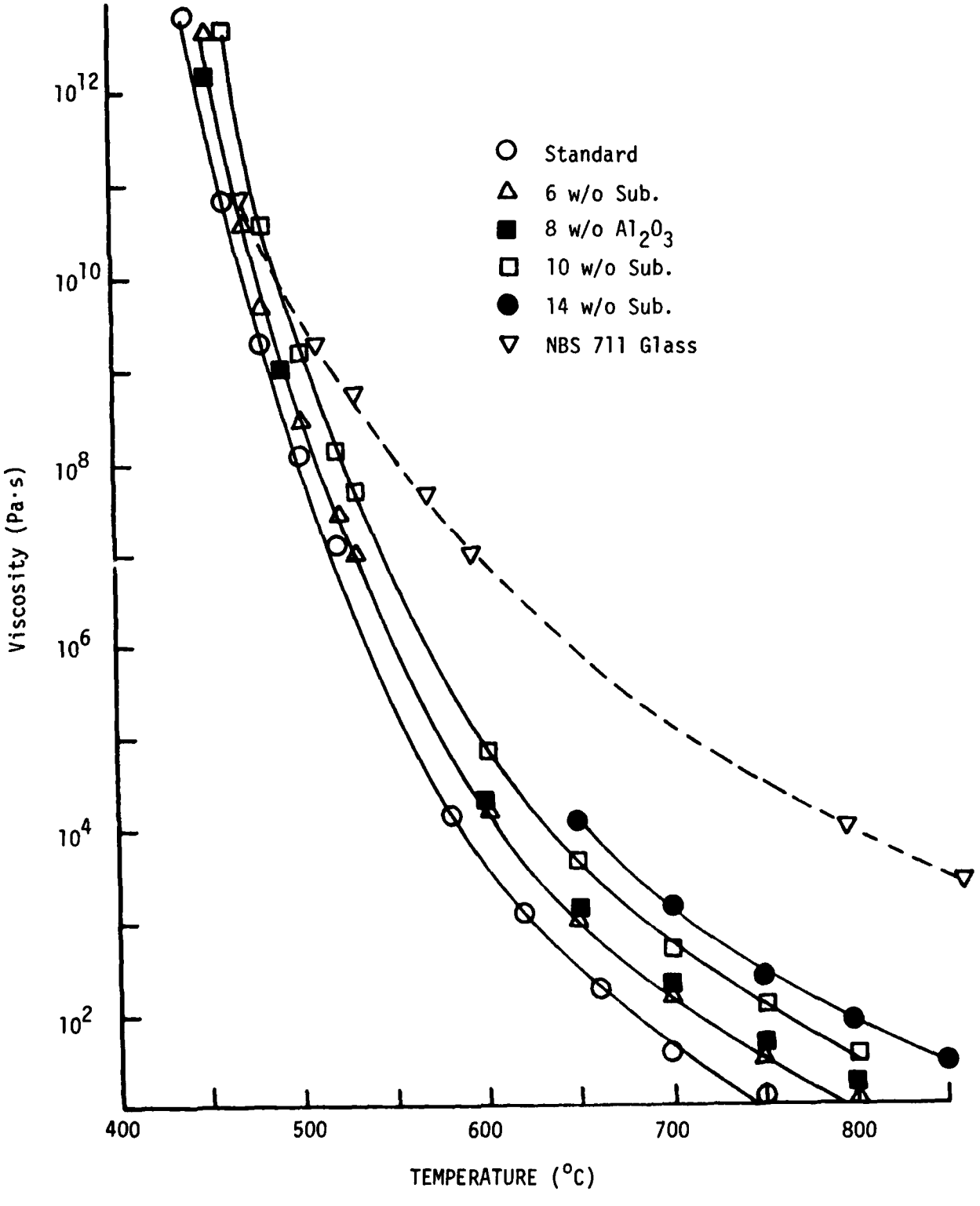

Figure 2.4. Effects of Composition and Temperature on Glass Viscosity.

Table II.2 The deviations at the low and high viscosities were systematic and high, indicating the inadequacy of the Fulcher equation in describing this system over the entire viscosity range. Although some glass compositions, such as NBS 711, could be represented very well by the Fulcher equation, a good fit over a wide range of viscosity data cannot be expected for any simple equation. Purely empirical expressions with four or five constants would give a better fit to the data, but such equations could be extremely misleading if an extrapolation of the data to other temperatures or a comparison between glass compositions was made. This is due to the continuous and rapid variation of activation energy with variation in temperature or viscosity as evident in the entire viscosity range shown by Fig. 2.3. The variation in the activation energy could be due to changes in the energy required to transport structural units of glass from one side to another or due to a change in the free volume which is essential for viscous flow. The size and composition of the flowing structural units could also be functions of temperature. In order to represent the high temperature viscosity as a function of weight percent dissolved substrate (P) and temperature, an empirical equation of the following form was derived by fitting the η values calculated from the Fulcher fits (Table II.1) to the Arrhenius equation:

$$\eta = (3.56 - 1.739\ P + 0.3798\ P^2) \times 10^{-7} \exp(18046/T) \qquad (2.2)$$

2.1.3 Influence of Minor Constituents of the Substrate.

The effect of composition on the glass viscosity can be qualitatively predicted if the composition-structure relationship of the glass system is known. The composition of AlSiMag 614 is given in Table I.1, and it can

TABLE II.2. Fulcher Equation Fit for Glass Viscosity ($10 - 10^{13}$ Pa·s)

$\text{Log } \eta = A'' + B''/(T - T_o)$ (η in Pa·s and T in K)

Composition	r^2	σ	A"	B"	T_o
Standard Glass	.9992	.1095	- 1.1627	1154.968	628.82
6 w/o Sub. Glass	.9996	.0778	- 1.1338	1199.303	631.09
10 w/o Sub. Glass	.9998	.0553	- 1.0605	1335.815	627.83
8 w/o Al_2O_3 Glass	.9996	.0805	- 1.1309	1287.192	620.92

be seen that this ceramic body contains approximately 96 w/o Al_2O_3, 3 w/o SiO_2, and smaller quantities of MgO, CaO, and other oxides. Additions of Al_2O_3 to sodium silicate glasses [6] and lead silicate glasses [7] are known to increase the viscosity. Alumina, being an intermediate glass former, can enhance the network structure by increasing the bridging-to-nonbridging oxygen ratio. The low as well as the high temperature viscosity data presented in Fig. 2.4 are consistent with these predictions. Silica, being a network former, is also expected to increase the viscosity.

The high temperature viscosity of the 8 w/o Al_2O_3 glass falls in between those of the 6 w/o sub. glass and the 10 w/o sub. glass as shown in Fig. 2.2. Considering the viscosity range of 10^{13} to 10 Pa·s, the 8 w/o Al_2O_3 glass exhibits a viscosity-temperature function slightly different from those of the other compositions as illustrated in Fig. 2.4. This difference may be because of variations in glass structure due to the alkaline earth oxides of the substrate.

2.2 Surface Tension of Glasses

2.2.1 Experimental.

The surface tension of glasses as a function of the amount of dissolved substrate were determined by the modified dipping cylinder method [8]. A hollow platinum cylinder, 1.3 cm in diameter and 1.3 cm in height with a wall thickness of 0.013 cm, was used in this study. The apparatus for the surface tension measurement is similar to the viscometer assembly shown in Fig. 2.1. The platinum cylinder was suspended by a platinum wire from the sample pan of the microbalance. The glass was thermally equilibrated, and the furnace raised until the bottom of the cylinder was 0.2 cm below the

glass level. The furnace was then slowly lowered and the maximum pull exerted by the glass on the cylinder determined by adding weights until the breakaway was indicated by the deflection of the beam. The surface tension (γ) was calculated using the following equation:

$$\gamma = \frac{gW}{4R}\left[1 - \frac{2.8284\delta}{\sqrt{hR}} - \frac{0.6095\delta}{R} + \frac{3\delta^2}{hR} + \frac{2.585\delta^2}{\sqrt{hR}} + \frac{0.371\delta^2}{R^2}\right]$$

in which

g = acceleration due to gravity

W = maximum pull exerted on the cylinder

R = mean radius of the cylinder

δ = half thickness of the cylinder

$h = W/R^2\ \rho_g$, ρ_g = density of glass

2.2.2 Results and Analysis

The surface tension results for five glass compositions are presented in Fig. 2.5. The standard glass exhibits a negative temperature coefficient of surface tension for the entire range of temperature investigated. The coefficient is strongly temperature dependent changing from 1.1 mN/m-°C at 600°C to 0.033 mN/m-°C at 900°C. These observations are consistent with an earlier study [9] which reported similar decreases in surface tension with increases in temperature for a PbO-B_2O_3-SiO_2 glass.

The addition of substrate or alumina increased the isothermal surface tension of the standard glass, and changed the temperature coefficient of surface tension as well. The surface tension values for the 8 w/o alumina glass are the same, within experimental error, as those of the 10 w/o substrate glass. The surface tension-temperature curves for all the substrate

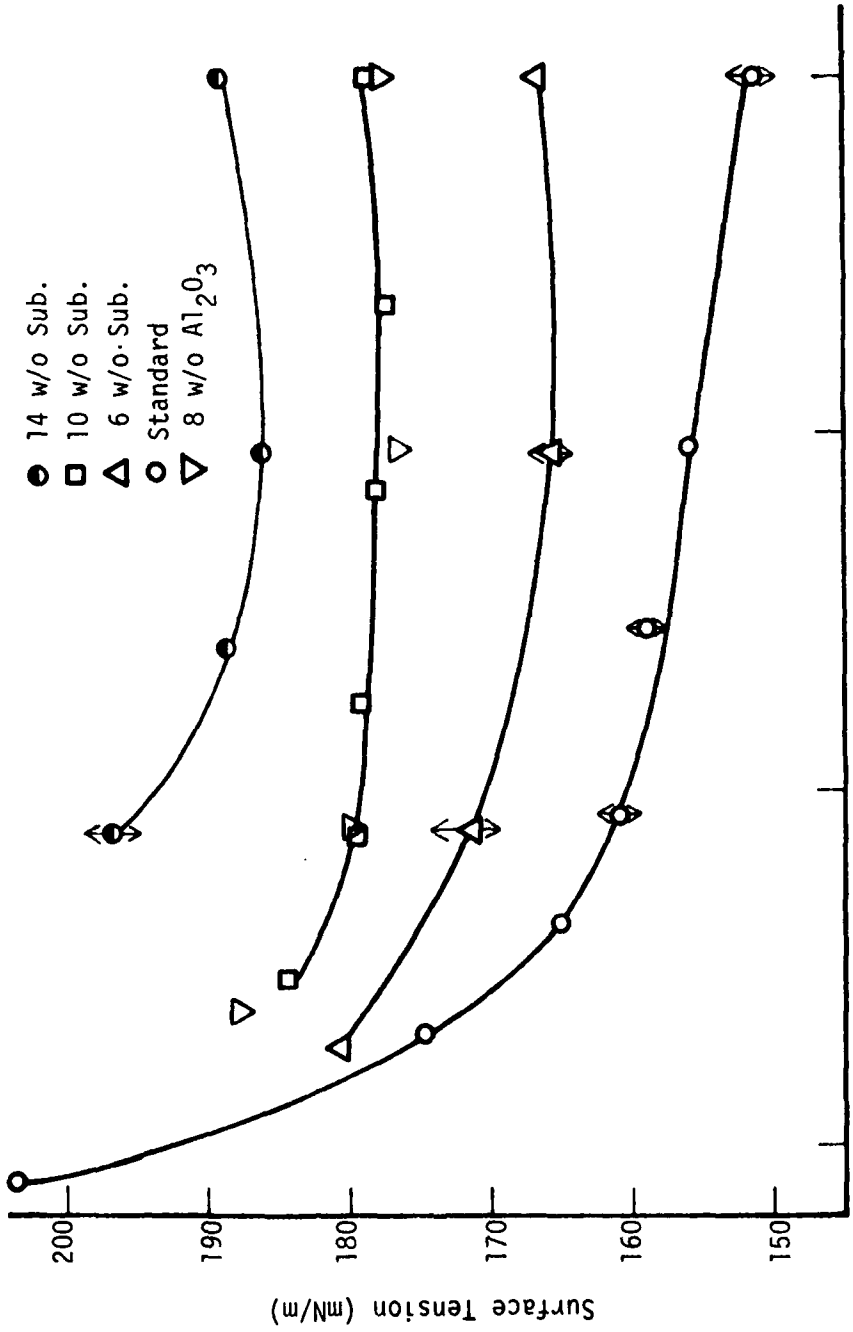

Figure 2.5. Surface Tension of Standard Glass with Various Amounts of Dissolved Alumina and Substrate.

or alumina doped glasses exhibited a minimum at about 800°C. The display of both positive and negative temperature coefficients has been reported for the $PbO-SiO_2$ system [8] and for the $BaO-B_2O_3-SiO_2$ system [10]. Additions of Al_2O_3 to a soda-lime-magnesia-silica glass have been reported [11] to increase the surface tension, and the substitution of Al_2O_3 for SiO_2 in this glass system was found [12] to increase the surface tension. These results are consistant with the present observations on the lead borosilicate system that Al_2O_3 increases the surface tension, and that Al_2O_3 has a more pronounced effect than SiO_2 on the surface tension.

Surface tension values near the softening point of the glass would be useful in estimating the kinetics of glass spreading and the microrearrangement of the conductive, but the dipping cylinder method is ineffective for temperatures below the flow point of glass. Therefore, the low temperature surface tension was evaluated by combining the low temperature viscosity data from the beam bending measurements [3] with the data on surface tension to viscosity ratio calculated from the initial stage sintering studies [2]. Due to the large temperature coefficient of viscosity ($\simeq$ 0.7 Pa·s/°C in the sintering range) of the glasses, the accuracy of this method is not high because even a small error in temperature can cause an appreciable error in the calculated values of the surface tension. The surface tension values were calculated for all the experimental γ/η data using viscosity calculated from Fulcher fits to the viscosity data (Table II.2). Assuming that the surface tension is constant in the sintering range, an average γ was calculated for each glass composition. Using the average γ, η values were calculated from the γ/η ratio and superimposed on the Fulcher lines. The average γ values and the superposition of calculated η on the Fulcher

lines are shown in Fig. 2.6. The surface tension does not show any systematic variation with composition, and the differences may be due to uncertainties in the experimental data.

2.3 Density of Glasses

The dissolution of substrate in bulk glass was shown to proceed through molecular diffusion and free convection [2, 3]. Free convection could be caused by gradients in temperature, surface tension, or density due to the dissolution of substrate in the glass. Convection due to temperature differences caused by the reaction can be considered negligible because the experiments were done at temperatures above 760°C where any thermal gradients caused by the dissolution are likely to be balanced by heat radiation from the bulk glass. Surface tension effects need not be considered for these experiments because the substrates were completely immersed in the glass.

The density was determined as a function of composition and temperature in the sphere viscometer utilizing Archimede's principle:

$$\text{Glass density} = \frac{(\text{wt of gold sphere in air}/\text{wt in glass})}{\text{weight in air}} \times \text{density of gold} \qquad (2.3)$$

The density results for the standard glass and four other compositions doped with AlSiMag 614 substrate or alumina are given in Fig. 2.7. The density (ρ) for each glass can be represented as a linear function of temperature in the range measured. The densities in gm/cc, are:

$$\text{Standard glass:} \quad \rho = 5.2607 - 1.1068 \times 10^{-3} T \qquad (2.4)$$

$$\text{6 w/o sub. glass:} \quad \rho = 4.6997 - 7.6200 \times 10^{-4} T \qquad (2.5)$$

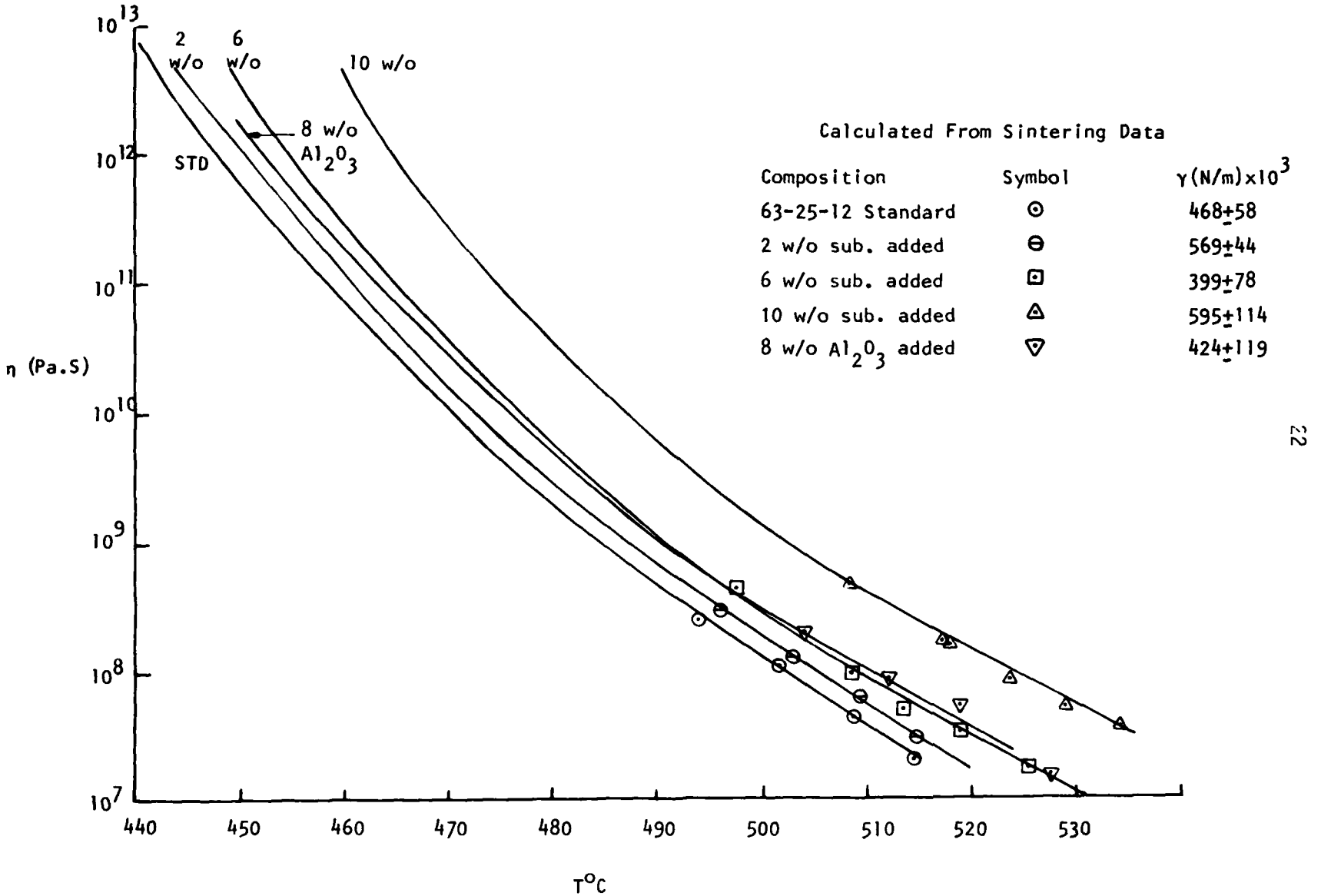

Figure 2.6. Comparison of Measured Viscosities (Lines) with Viscosities Calculated from Sintering Data (Points).

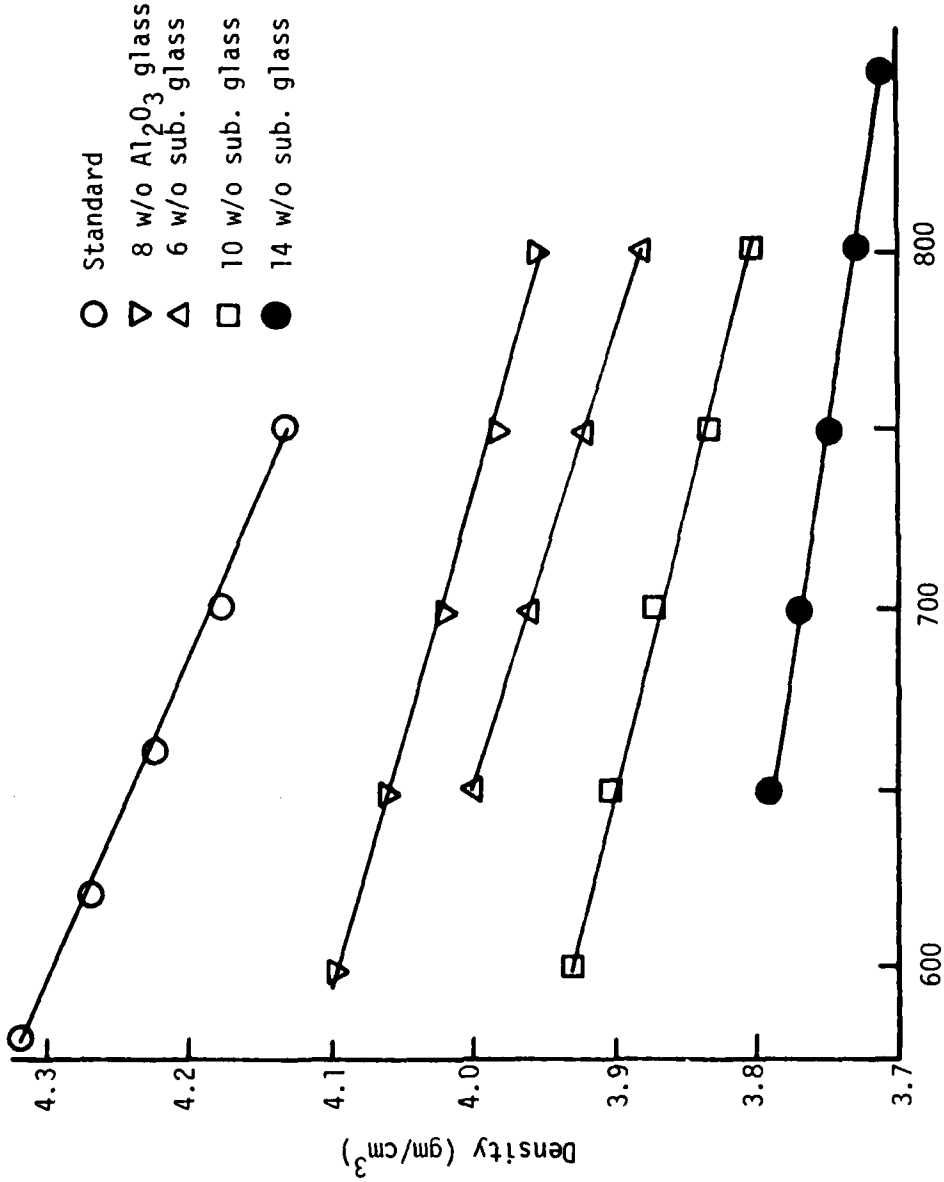

Figure 2.7. Variation of Glass Density with Composition and Temperature.

10 w/o sub. glass: $\rho = 4.5096 - 6.6000 \times 10^{-4} T$ (2.6)

14 w/o sub. glass: $\rho = 4.1457 - 3.8800 \times 10^{-4} T$ (2.7)

8 w/o Al_2O_3 glass: $\rho = 4.7163 - 7.1400 \times 10^{-4} T$ (2.8)

The decrease in density of glass due to substrate dissolution could be responsible for natural convection following the molecular diffusion process during the dissolution of substrate in bulk glasses. The temperature coefficient of density, for the temperature range investigated, is seen to decrease with increasing additions of substrate.

The density of a liquid may be approximated to be an additive property of its constituents. However, nonlinear behavior would be observed if the constituents differ greatly in density or if there is a change in the structure of the liquid due to the addition. Additivity factors for room temperature density based on percent by weight of PbO, B_2O_3, SiO_2, and Al_2O_3 have been reported [6] to be 9.6, 1.9, 2.3, and 4.1, respectively. Addition of Al_2O_3 to a high lead glass would be expected to decrease the density, and addition of SiO_2 should bring the density down even further. Thus the additivity factors qualitatively explain the fact that the addition of substrate lowers the density more than the addition of an equal amount of pure Al_2O_3. However, the differences cannot be accounted for by considering additivity factors alone; possible differences in glass structure, as indicated by the anomalous behavior of the viscosity of 8 w/o Al_2O_3 glass, may be responsible for the observed anomaly in density.

2.4 RuO_2 Ripening

2.4.1 Experimental.

RuO_2-glass composites consisting of 20 or 30 w/o RuO_2 were prepared by blending the powdered components in a jar placed on rollers. The RuO_2 powder was prepared by drying the hydrate, and the glass frit was reduced to -325 mesh in an agate ball mill prior to blending.

Approximately 1 gram of the composite was exposed to the given temperature for a known length of time and then quenched in deionized water. The quenched samples were decomposed by a HCl + HF treatment followed by a centrifugal separation of the RuO_2 solids from the solution. The RuO_2 is inert to HCl + HF mixtures. The RuO_2 particles were then washed with deionized water and dried.

The average particle size of the RuO_2 was determined by measuring the surface area by the BET [13] method utilizing a Monosorb* Surface Area Analyzer. The Monosorb, essentially a thermal conductivity detector, measures the quantity of adsorbate gas adsorbed on or desorbed from the sample surface by sensing the change in the thermal conductivity of an adsorbate-carrier gas mixture flowing over the solid particles. A 30 v/o nitrogen (adsorbate) in helium (carrier) was used in this work. Selective adsorption or desorption of the adsorbate causes a momentary change in the gas composition and hence a change in the thermal conductivity of the mixture. The integrated signal due to the change in thermal conductivity is proportional to the amount of adsorbate adsorbed or desorbed. From the amount of nitrogen adsorbed, the surface area was calculated using the BET

---

* Quantachrome Corp., Greenvale, New York

relationship [13]. From the specific surface area, the average particle size was calculated by assuming that the particles were spherical.

2.4.2 Results and Analysis

The results of the surface area measurements on RuO_2 samples held for varying times in the standard, 2 w/o, 4 w/o, and 10 w/o substrate doped glasses at 950°C are given in Fig. 2.8. The extensive measurements of RuO_2 particle growth in the standard and 10 w/o substrate glasses showed that after a rapid decrease, the surface area decreased very slowly at longer times. The results also indicate that the ripening process is considerably retarded by the addition of substrate to the standard glass. The amount of RuO_2 relative to the glasses was varied from 20 to 30 w/o for the standard and 10 w/o substrate doped glasses, and the effect of this variation on the ripening kinetics is seen to be insignificant. For ripening at 888 and 1000°C, composites made of RuO_2 and the standard, 4 w/o, 10 w/o, and 14 w/o substrate doped glasses were used in order to cover a wider glass composition range.

Greenwood [14] developed an expression to describe the growth of dispered particles in a saturated solution by a diffusion mechanism. Lifshitz and Slyozov [15] and Wagner [16] have developed a more rigorous model (known as 'LSW Theory') to predict the kinetics of ripening of solid particles dispersed in a continuous matrix. If diffusion controlled solution-precipitation is the rate limiting step for the process of ripening, the average particle radius obeys the following time dependence.

$$[\bar{r}(t)]^3 - [\bar{r}(0)]^3 = \left[\frac{8}{9}\frac{C_o \gamma_{sl} V_o^2 D}{MRT}\right] t \qquad (2.9)$$

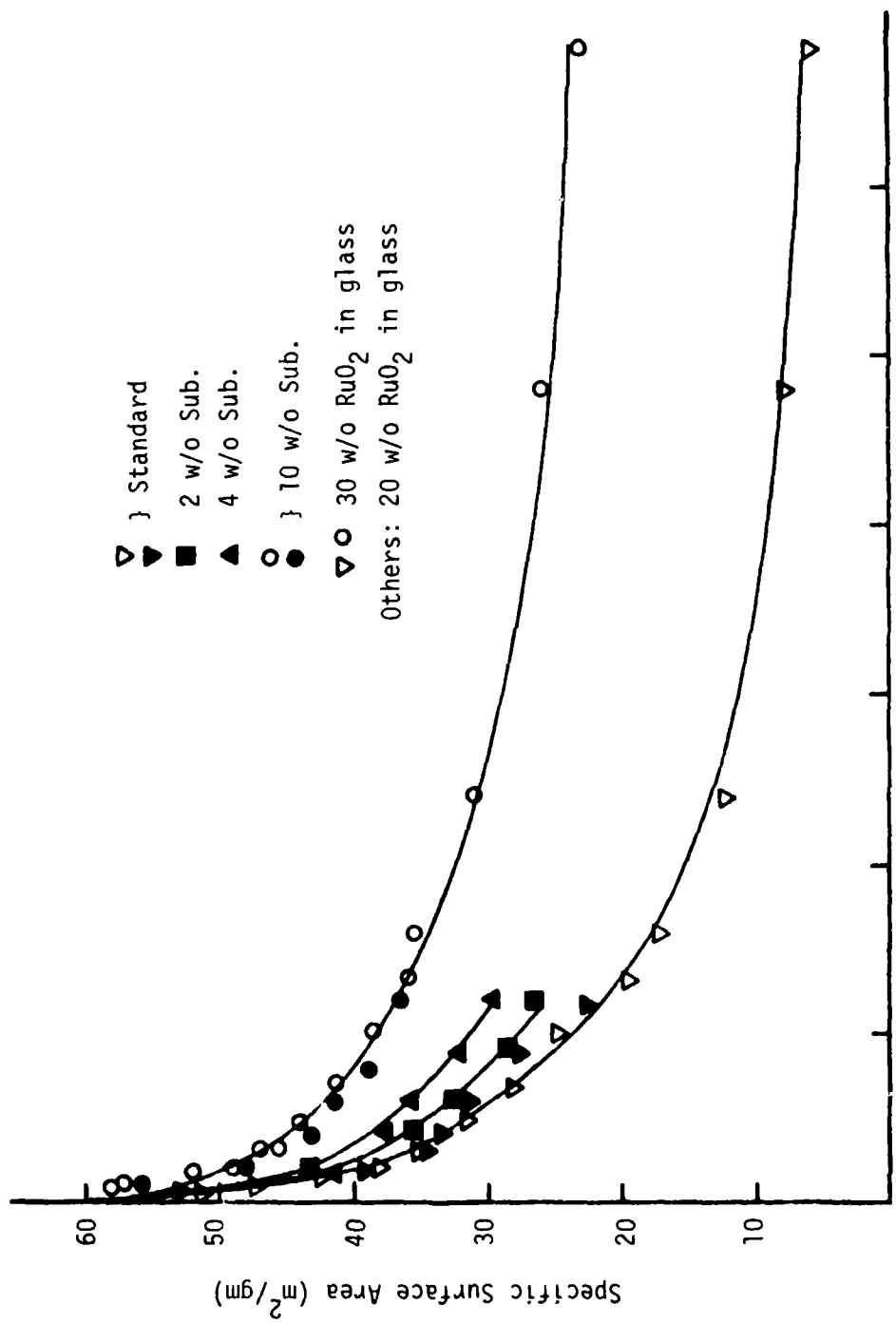

Figure 2.8. Ripening of RuO_2 in Glasses at 950°C.

In Eq. 2.9, $\bar{r}(t)$ is the average particle radius at time t, $\bar{r}(0)$ is the average particle radius at time zero, C_o is the equilibrium solubility of the solid in the liquid, γ_{sl} is the solid-liquid interfacial energy, V_o is the molar volume, and D is the diffusion coefficient of the slowest moving species. If the growth occurs by a phase boundary reaction controlled solution-precipitation process, the average particle radius increases according to,

$$[\bar{r}(t)]^2 - [\bar{r}(0)]^2 = \left[\left(\frac{8}{9}\right)^2 \frac{C_o \gamma_{sl} V_o^2 K_T}{MRT}\right] \qquad (2.10)$$

where K_T is the transfer coefficient. As a result of the ripening process, the number of particles per unit volume, N, steadily decreases with time,

$$\frac{N(t)}{N(0)} = (\bar{r}(t) - \bar{r}(0))^{-3} \qquad (2.11)$$

Equations (2.9) to (2.11), the more readily applicable forms of the LSW theory, were suggested by Fischmeister and Grimwall [19].

Least squares fits of the experimental data to Eqs. 2.9 and 2.10 for varying glass compositions at three different temperatures indicated that the interface reaction is the slowest step of mass transport in this system. Plots of $([\bar{r}(t)]^2 - [\bar{r}(0)]^2)$ versus time are straight lines for all the three temperatures investigated, as shown in Figs. 2.9 through 2.11. The slopes of the lines are proportional to $C_o\ \gamma_{sl}\ K_T$; at 950°C, the slope is reduced by a factor of four by the addition of 10 w/o substrate to the standard glass. The values of $C_o\ \gamma_{sl}\ K_T$ were calculated from the slopes, and least squares analyses were performed on the data to obtain the following equations:

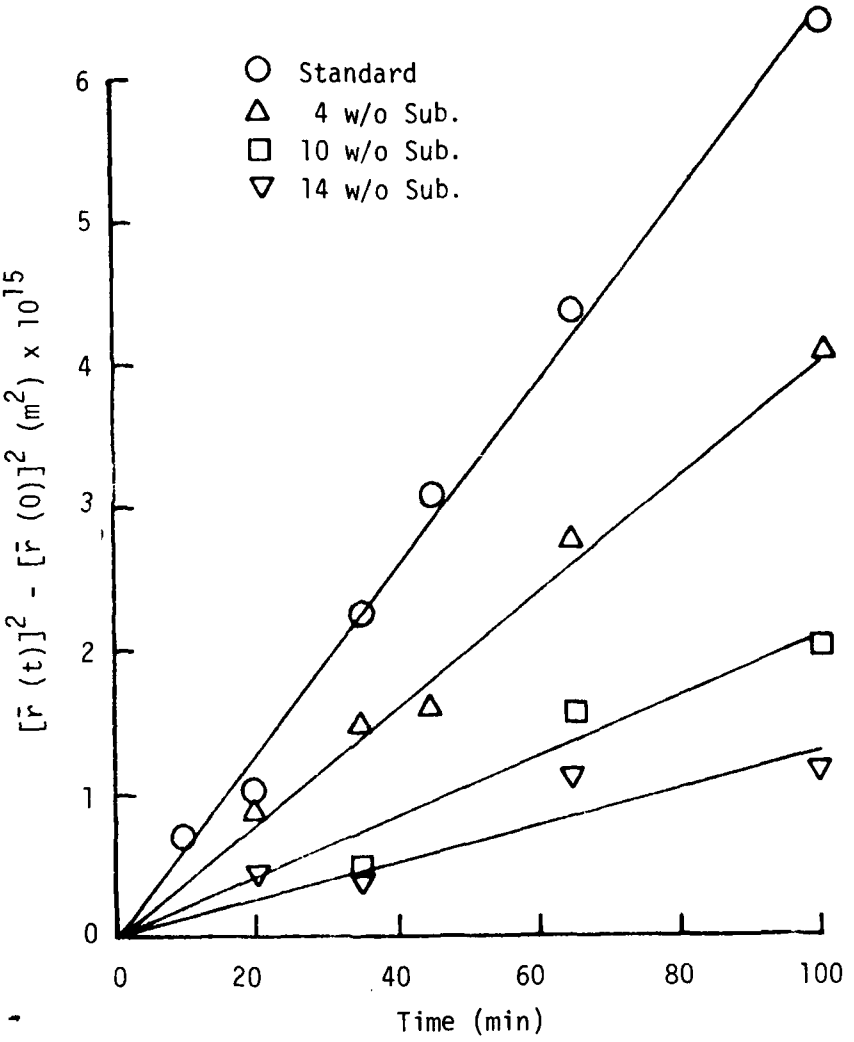

Figure 2.9. RuO_2 Ripening in Glasses at 888°C.

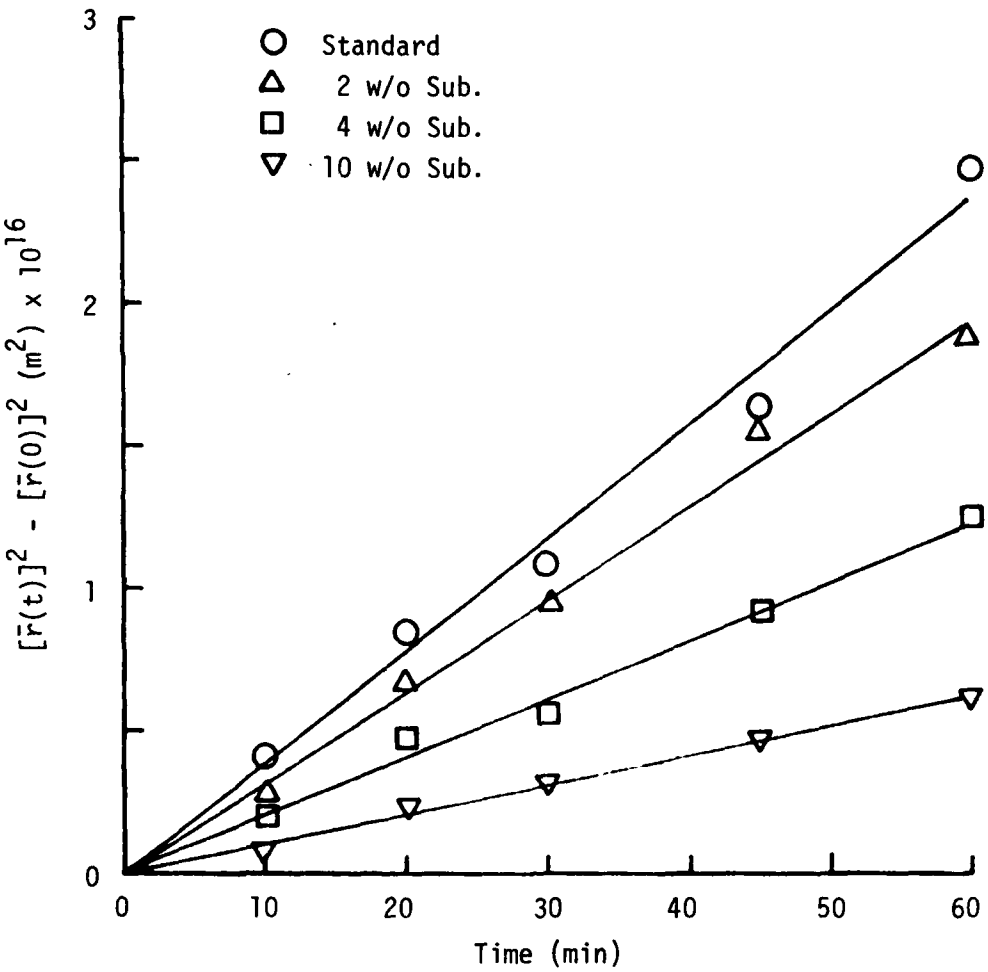

Figure 2.10. RuO_2 Ripening in Glasses at 950°C.

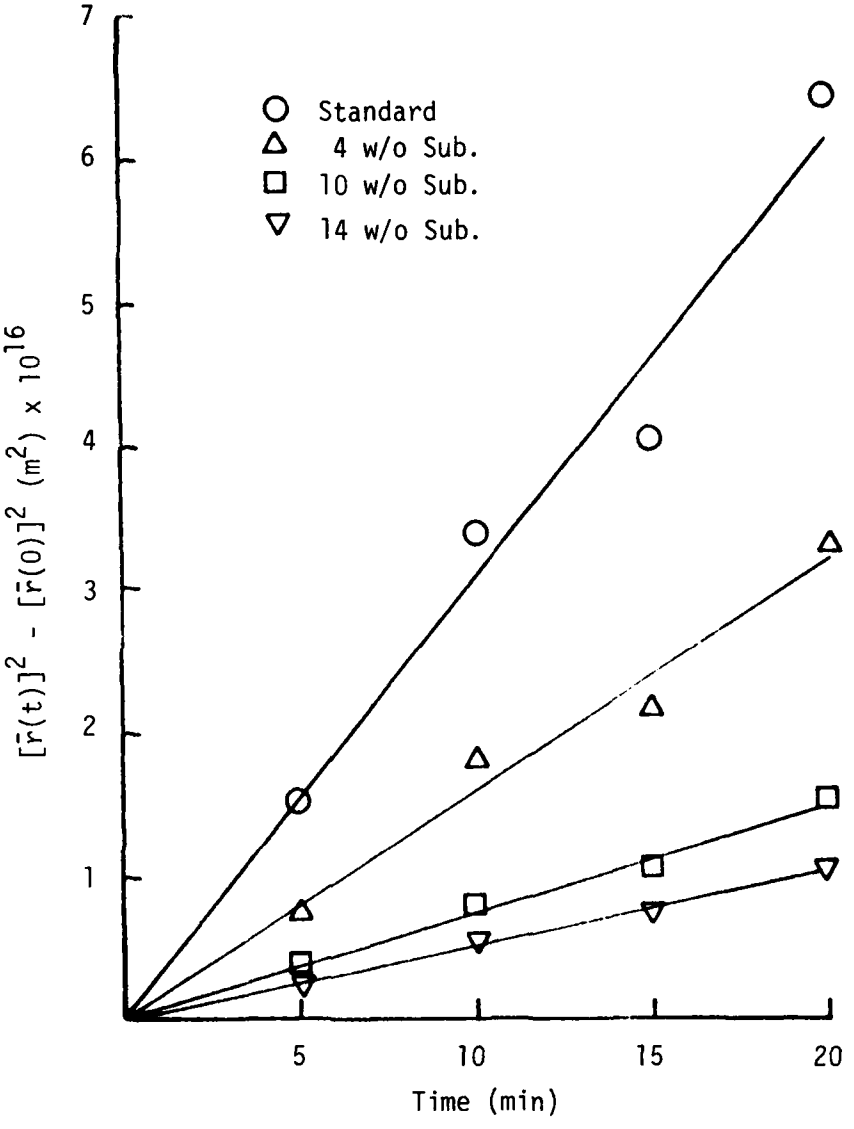

Figure 2.11. RuO_2 Ripening in Glasses at 1000°C.

$$\text{Standard glass:}\quad C_o\,\gamma_{sl}\,K_T = 8.577\text{X}10^{6}\exp[-(51601\pm6416)/T] \qquad (2.12)$$

$$\text{4 w/o sub. glass:}\quad C_o\,\gamma_{sl}\,K_T = 6.533\text{X}10^{5}\exp[-(49187\pm7559)/T] \qquad (2.13)$$

$$\text{10 w/o sub. glass:}\quad C_o\,\gamma_{sl}\,K_T = 9.206\text{X}10^{4}\exp[-(47637\pm6796(/T] \qquad (2.14)$$

$$\text{14 w/o sub. glass:}\quad C_o\,\gamma_{sl}\,K_T = 5.305\text{X}10^{5}\exp[-50085/T] \qquad (2.15)$$

Here C_o is in gm/cc, γ_{sl} in J/cm^2, and K_T in cm/s. An average Q/R of -49626 J/mole was selected to represent all the four compositions because the differences in the Q/R of the individual glasses were within one standard deviation. Using the average Q/R, an average value of the pre-exponential for each glass was calculated. Utilizing these results, an empirical equation for $C_o\,\gamma_{sl}\,K_T$ as a function of weight percent substrate (P) and temperature was derived.

$$C_o\,\gamma_{sl}\,K_T = \left[\frac{17.29 \times 10^{5}}{1 + .172\,P + .00686\,P^{2}}\right]\exp(-49626/T) \qquad (2.16)$$

The $C_o\,\gamma_{sl}\,K_T$ values obtained from the slopes and from Eq. (2.16) are compared in Fig. 2.12.

Knowing C_o from the RuO_2 solubility measurements [3] and taking γ_{sl} to be 20 μJ/cm^2 as was suggested [18] to represent the solid-liquid interfacial energy of the MgO-CaO-SiO_2 system, K_T was calculated as a function of composition and temperature. The calculated values of K_T are listed in Table II.3. The transfer coefficient for any given temperature goes through a maximum near 4 w/o substrate doping. This anomalous behavior is probably due to the assumption that the interfacial energy is independent of glass composition. RuO_2 solubility results [3] show that the activity of RuO_2 in glass increases rapidly with glass composition up to 2 w/o substrate doping; the interfacial energy may exhibit a composition dependence similar to

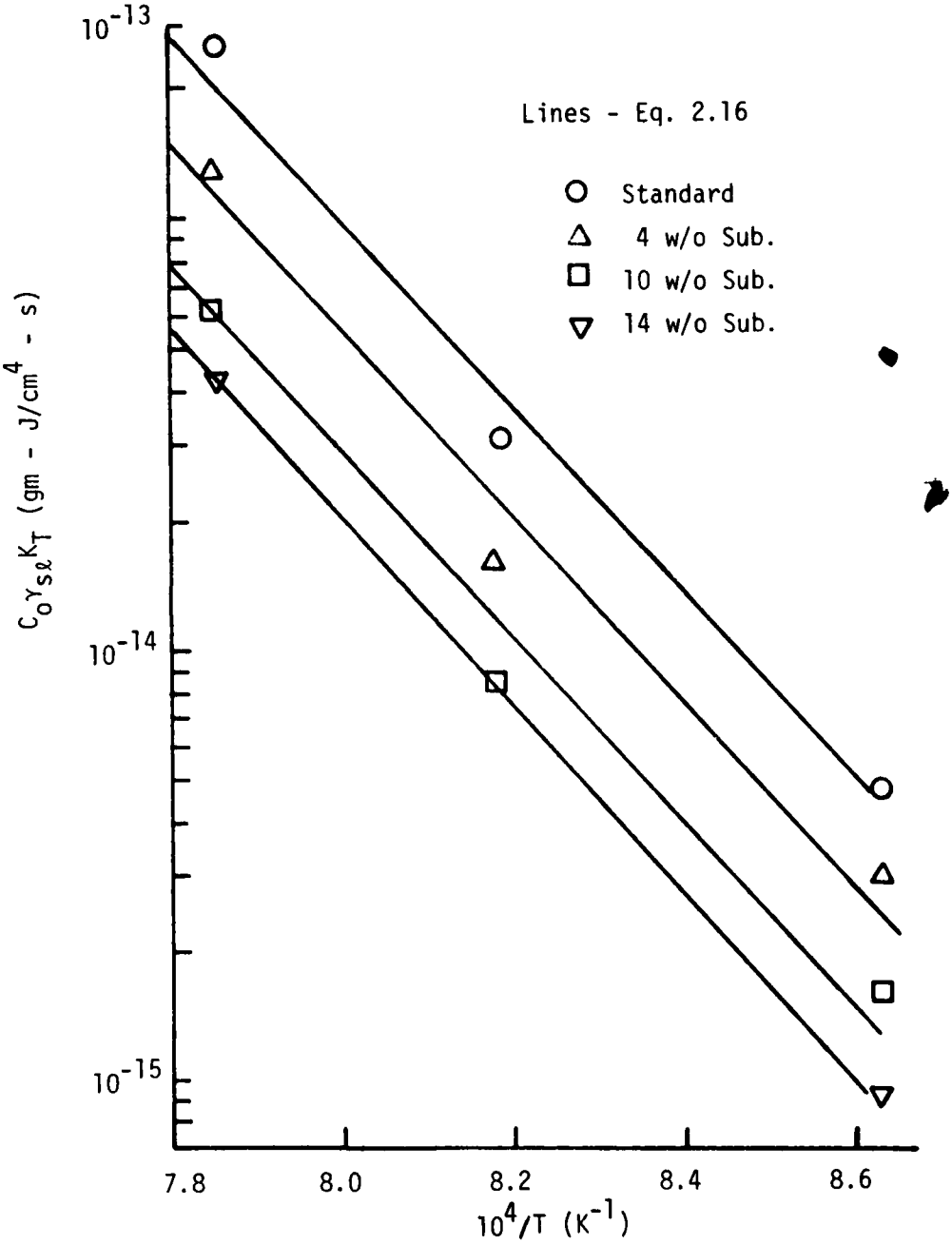

Figure 2.12. Variation of $C_o\gamma_{s\ell}K_T$ with Composition and Temperature.

TABLE II.3. Variation of K_T with Composition and Temperature.

Composition	K_T(m/sec) X 10^7 at		
	888°C	950°C	1000°C
Standard Glass	5.61	28.3	191.0
4 w/o Sub. Glass	6.55	31.2	229.0
10 w/o Sub. Glass	3.45	16.0	107.0
14 w/o Sub. Glass	2.13	--	76.0

that of the activity of RuO_2. Although the transfer coefficient could not be determined precisely from the ripening results, the product $C_o \gamma_{sl} K_T$ is sufficient to predict RuO_2 sintering kinetics based on a liquid-phase sintering model presented in the following section.

2.5 RuO_2 Sintering

2.5.1 General

In order to develop an adequate model for the influences of the substrate on microstructure development and electrical properties of thick film resistors, it is necessary to know the influence of the dissolved substrate on conductive sintering. In the initial stages of the sintering process, necks develop between adjacent RuO_2 conductive particles; as the sintering process proceeds, the necks grow until adjacent particles coalesce to form particles. The primary driving force for sintering is the reduction in interfacial area between the conductive phase and the glass phase.

Earlier studies [19] have shown that the kinetics of the RuO_2 sintering process could not be measured directly because of the extremely small size of the RuO_2 particles, but rates consistent with experimental observations were calculated from RuO_2 ripening results based on a solution-precipitation mechanism. It was also observed that the presence of AlSiMag 614 substrate dissolved in the resistor glass decreased the rate of RuO_2 ripening, but quantitative studies of the effect of glass composition were not made.

2.5.2 Model and Analysis

Consider a pair of spherical particles in contact, completely immersed in a liquid, as shown in Fig. 2.13.

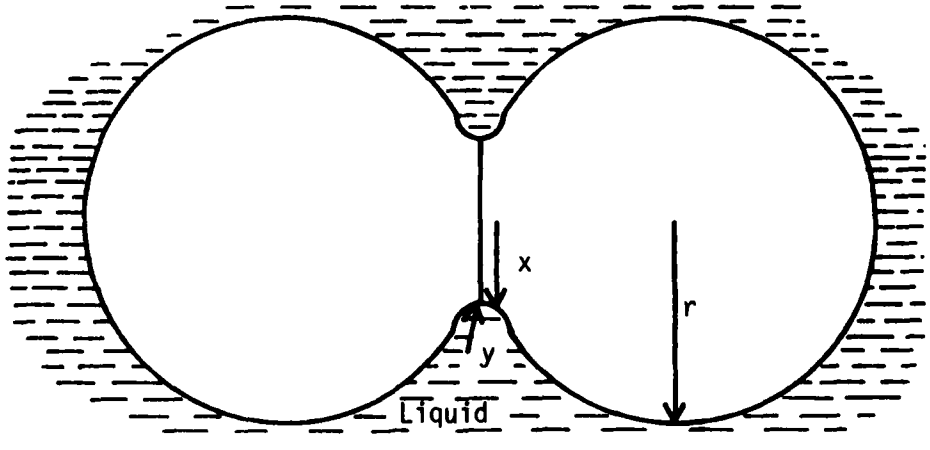

Figure 2.13. Liquid-Phase Sintering Model with a Solid-Solid Contact, Completely Immersed in a Liquid.

If r is the radii of the particles, the concentration of species at the solid-liquid interface away from the neck region relative to that at a flat interface can be written as [20]:

$$\ln \frac{C_1}{C_o} = \frac{2\gamma_{sl} M}{r\rho RT}$$

$$C_1 - C_o \simeq \frac{2\gamma_{sl} M C_o}{r\rho RT} \tag{2.17}$$

If x and y are the principal radii of curvature of the neck, the concentration of species in the neck region relative to that at a flat interface is given by

$$\ln \frac{C_2}{C_o} = \frac{\gamma_{sl} M}{\rho RT}\left[\frac{1}{x} - \frac{1}{y}\right]$$

$$\simeq -\frac{\gamma_{sl} M}{y\rho RT} \qquad \text{for } x >> y$$

$$C_2 - C_o = -\frac{\gamma_{sl} M C_o}{y\rho RT} \tag{2.18}$$

Here C_1, C_2, and C_o are the concentrations on the free-surface, neck, and flat interface, respectively; M is the molecular weight of the solid; and ρ is the density of the solid. Combination of Eqs. (2.17) and (2.18) gives

$$\Delta C = C_1 - C_2 = \frac{\gamma_{sl} M C_o}{\rho RT}\left[\frac{2}{r} - \frac{1}{y}\right]$$

$$\Delta C \simeq \frac{\gamma_{sl} M C_o}{y\rho RT} \qquad \text{for } r >> y \tag{2.19}$$

If the neck growth between the particles is limited by the interface reaction, the rate of mass transfer, J(gm/s), can be written as

$$J = K_T A \Delta C \tag{2.20}$$

in which K_T (cm/s) is the transfer coefficient, A(cm^2) is the interfacial area, and ΔC (gm/cm^3) is the concentration difference between the free-surface and the neck area.

For transport limited by redeposition at the neck, the interfacial area, A, in Eq. (2.20) is the neck area, and from Fig. 2.14,

$$A \simeq 1/2(2\pi y)(2\pi x)$$
$$= 2\pi^2 xy$$

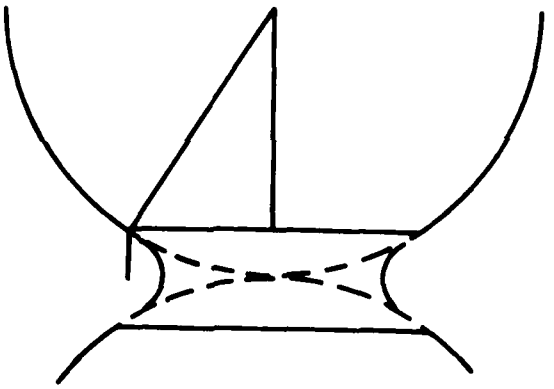

Figure 2.14. Geometry of Neck Between Particles Undergoing Liquid-Phase Sintering.

Substituting for A and ΔC in Eq. (2.20) gives,

$$J = \frac{2\pi^2 x K_T \gamma_{sl} MC}{\rho RT}$$

By conservation of mass,

$$J = dV_n\rho/dt$$

in which

$$V_n = \text{neck volume}$$

From Fig. 2.14,

$$V_n \simeq 1/2\ \pi x^2(2y)$$

and

$$y = (r - a) \simeq r(1 - \cos\theta) \simeq 2r\,\frac{\theta^2}{4} \simeq \frac{x^2}{2r}$$

therefore

$$J \simeq d\left(\frac{\pi x^4}{2r}\right)\rho/dt$$

$$= \frac{2\pi\rho x^3}{r}\,dx/dt$$

$$x^2dx = \frac{\pi K_T \gamma_{sl} MC_o r\,dt}{\rho^2 RT}$$

and finally

$$\left(\frac{x}{r}\right)^3 = \frac{3\pi K_T \gamma_{sl} MC_o r^{-2} t}{\rho^2 RT} \qquad (2.21)$$

This mechanism does not lead to shrinkage of a powder compact:

$$\frac{\Delta L}{L_o} = 0 \qquad (2.22)$$

If the neck growth is controlled by the diffusion of species through the liquid, the rate of mass transfer will be given by

$$J = \frac{D\ A\ \Delta C}{0.78r} \qquad (2.23)$$

in which $D(cm^2/s)$ is the diffusion coefficient of the slowest moving species in the liquid, and 0.78r is the average diffusion length which is taken to be equal to 1/8 of the periphery of the projected particle. Substituting

for A and ΔC in Eq. (2.23), and by proceeding as for the interface controlled situation, gives

$$\left(\frac{x}{r}\right)^3 = \frac{3\pi D\gamma_{sl}MC_o r^{-3}t}{0.78\rho^2 RT}$$

$$\simeq \frac{4\pi D\gamma_{sl}MC_o r^{-3}t}{\rho^2 RT} \qquad (2.24)$$

$$\frac{\Delta L}{L_o} = 0 \qquad (2.25)$$

The effects of composition and temperature on the ripening of RuO_2 in glass was given by Eq. (2.16). By assuming that the transfer coefficient is the same for the ripening and the neck growth processes, the kinetics of neck growth between RuO_2 particles can be computed by combining Eqs. (2.21) and (2.16). The resulting equation is

$$x^3 = \frac{3\pi Mrt}{\rho^2 RT} \frac{17.29 \times 10^5 \exp(-49626/T}{(1 + 0.172P + 0.00686P^2)} \qquad (2.26)$$

The time required for completion of the initial stage sintering ($x/r = 0.3$) of RuO_2 particles of different sizes in the standard glass is given as a function of temperature in Table II.4. At 800°C it takes about 165 seconds to complete the initial stage sintering for particles of 5 nm (50 Å) radius; whereas for particles of 1 μm radius, it takes nearly 2 1/2 months to achieve the same ratio of neck to particle radius. The effect of temperature on the neck growth process, as indicated by the high activation energy for ripening, is tremendous. For example, the time required by 5 nm particles to complete the initial stage sintering is increased by a factor of 100 if the temperature is lowered from 800 to 700°C.

TABLE II.4. Calculated Initial Stage Neck Growth Kinetics of RuO_2 in the Standard Glass.

Temperature °C	Time(s) for x/r = 0.3				
	r = 5 nm	r = 10 nm	r = 100 nm	r = 1 μm	r = 10 μm
650	$2.60X10^5$	$1.04X10^6$	$1.04X10^8$	$1.04X10^{10}$	$1.04X10^{12}$
700	$1.73X10^4$	$6.92X10^4$	--	--	--
750	$1.50X10^3$	$6.01X10^3$	--	--	--
800	$1.65X10^2$	$6.58X10^2$	--	--	--
850	1.65X10	6.58X10	--	--	--
900	3.49	1.39X10	$1.39X10^3$	$1.39X10^5$	$1.30X10^7$

The effect of glass composition on the neck growth kinetics is indicated by Eq. (2.26). Additions of 4, 10, and 14 w/o substrate to the standard glass increase the time required for the completion of initial stage sintering by factors of approximately 2, 3.5, and 5, respectively.

Equation (2.26) also indicates that for a given glass composition, temperature, and time, the neck size would be proportional to 1/3 power of the particle size. The neck size calculated as a function of RuO_2 particle size and sintering temperature for a 10 minute sintering in the standard glass is given in Table II.5. A comparison of Tables II.4 and II.5 indicates that although larger particles take longer times (proportional to the square of their size) to complete the initial stage sintering ($x/r = 0.3$), they can achieve, for a given time, a larger neck radius (proportional to $r^{1/3}$) than the smaller particles.

2.6 Substrate-Resistor Interactions

The results of substrate dissolution in resistor films and in bulk glasses were presented in previous reports [1-3]. The enhanced dissolution of the substrate in the films was suggested to be due to the agitation caused by bubble release during resistor firing. Direct observation of resistor films during hot-stage firing clearly showed that the films were in a state of agitation over a considerable period of the firing cycle. The dissolution of the substrate in resistor films is envisioned to proceed by the diffusion of substrate material through a thin boundary layer into the bulk of the film which is kept uniform in composition by the agitation. The steady state recession of the substrate thickness (Y) for such a process can be given by [21]:

TABLE II.5. Dependence of Neck Size on Particle Size and Temperature

Temperature °C	Neck Size x in nm for t = 10 min.				
	r = 5 nm	r = 10 nm	r = 100 nm	r = 1 μm	r = 10 μm
650	0.199	0.250	0.539	1.161	2.502
700	0.490	0.617	1.330	2.865	6.174
750	1.106	1.394	3.002	6.468	13.94
800	> 1.5*	2.914	6.277	13.52	29.14
850	> 1.5	> 3.0	12.28	26.46	57.02
900	> 1.5	> 3.0	22.68	48.86	105.2

* Neck growth calculations using Eq. (2.26) valid for $x/r \leq 0.3$ only.

$$\frac{dY}{dt} = D^* \frac{(P_o - P)}{\delta} \tag{2.27}$$

in which D* is the diffusion coefficient of the species in the boundary layer; P_o is the saturation solubility (w/o) of substrate in the glass phase; P is the w/o substrate in the glass; and δ is the boundary layer thickness which is a function of the fluid-dynamic conditions in the film.

The thickness of the boundary layer for laminar flow over a flat plate is given [22] by

$$\delta = \frac{4.64\ x}{\sqrt{Re_x}} \ ; \ Re_x = \frac{x\nu\rho}{\eta} \tag{2.28}$$

in which x is the distance from the leading edge of the plate, Re_x is the Reynolds number at x, and ν, ρ, and η, are the velocity, density, and viscosity of the fluid, respectively. Applying Eq. (2.28) to the situation of a resistor film on a substrate gives:

$$\delta = \text{constant} \cdot \sqrt{\frac{\eta}{x\nu\rho}}$$

Here η is the resistor viscosity which is approximately equal to the glass viscosity in this work, x is a characteristic length equal to the bubble size, ν is the velocity of the bubble, and ρ is the density of the resistor. The bubble velocity, by Stoke's law, is inversely proportional to the viscosity. Assuming that the number and size of the bubbles are independent of resistor composition and temperature, and by neglecting the changes in the density of the resistor, the boundary layer thickness can be expressed by

$$\delta = \text{constant} \cdot \eta$$

so that Eq. (2.27) becomes

$$\frac{dY}{dt} = C\ D^*(P_o - P)n \qquad (2.29)$$

Here P_o is a function of temperature, P is a function of Y, and D* and n are functions of both P and temperature. An average value of the constant C was determined by fitting the substrate dissolution in film data [2, 3] to Eq. (2.29). The fitting was done by first expressing the experimental data in the form of an analytical expression and then by an iterative process to get Y as a function of time. Knowing C from the above analysis, P_o from the solubility studies [3], D* from measurements of dissolution in bulk glass as a function of composition and temperature [3], and n from the high temperature viscosity results as a function of composition and temperature (Eq. (2.2)), a composition-time profile can be constructed for any given temperature and initial composition.

The experimental dissolution data for 760, 840, and 920°C are compared with the calculated profiles in Fig. 2.15. The theoretical expression gives a good fit to the experimental data for 840°C, and it fits the high and low temperature data reasonably well. The composition-time profiles calculated using Eq. (2.29) for three initial resistor glass compositions are given in Fig. 2.16. For processing at 920°C, the profiles for all three starting compositions are almost identical for times greater than half a minute. A similar behavior is observed at 840°C for initial substrate contents up to 5 w/o. At 760°C, a significant difference in the profiles for the standard and the 10 w/o substrate glass resistors is observed due to the slow dissolution kinetics at this temperature. At temperatures below 640°C, the substrate-resistor interaction is insignificant.

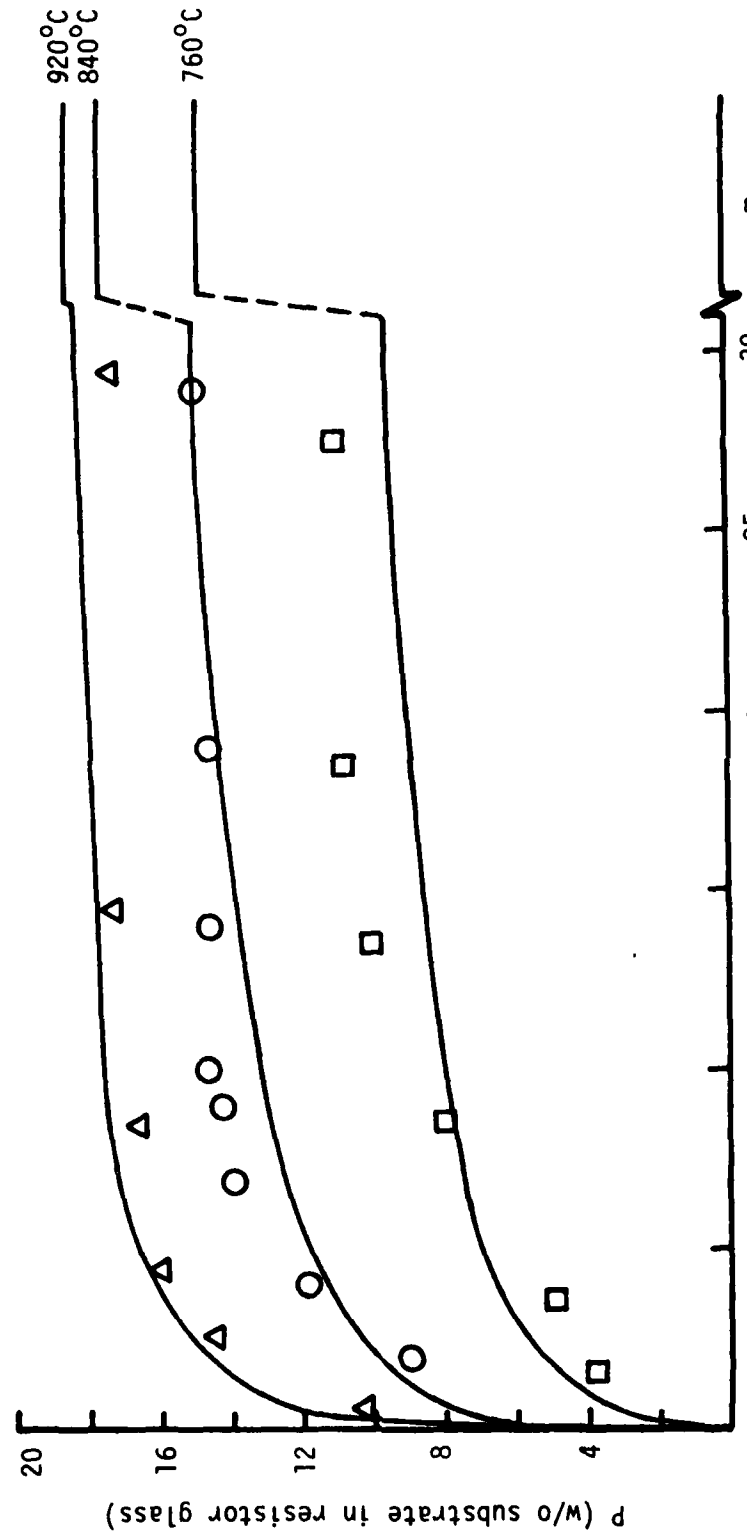

Figure 2.15. Comparison of Theory and Experiment for the Dissolution of AlSiMag 614 Substrate in Printed and Fired 5 w/o RuO_2 Resistors (solid lines calculated from Eq. 2.29).

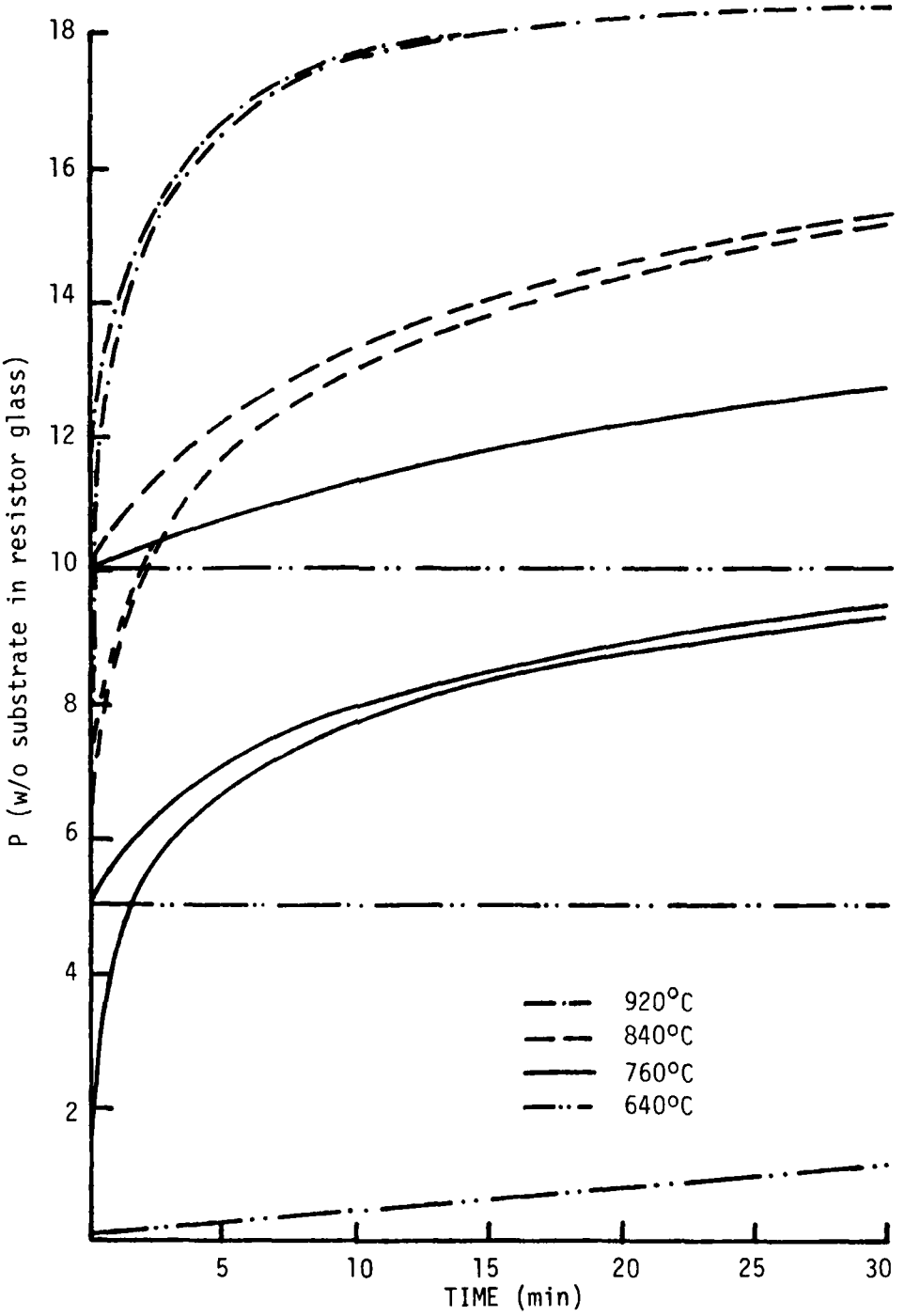

Figure 2.16. Variation of Resistor Glass Composition with Time and Temperature for Different Initial Composition Glasses.

The T-t-P profiles of Fig. 2.16 indicate that at the normal peak firing temperature ($\sim 850^{\circ}C$), unless the starting resistor glass is nearly saturated with the substrate (or Al_2O_3), the final glass composition will be insensitive to the initial composition. In order to minimize the interaction between the substrate and the resistor, the resistor glass may be doped with Al_2O_3 to reduce the reactivity of the glass while still maintaining the necessary fluidity for various microstructure development processes.

2.7 Microstructure Development Model

Previous studies [23] of microstructure development in RuO_2-lead borosilicate glass thick film resistors led to a model which described a sequential process during resistor firing. As the temperature moves above $400^{\circ}C$, glass particles which are adjacent to the smaller RuO_2 particles begin to flow and spread over and between the RuO_2 particles, while glass particles which are adjacent to other glass particles begin to form sintered necks. The glass particles, with RuO_2 particles held on their surfaces by partial wetting, tend to become more spherical in order to minimize their surface area. In the temperature range $450\text{-}500^{\circ}C$, both sintering and spreading processes become more rapid, and any RuO_2 particles which were initially in contact with a glass particle and separated from each other by a distance less than their diameter will be rapidly pulled together by a rearrangement process. As the sintering of the glass proceeds, the centers of adjacent glass particles move toward one another, and individual RuO_2 particles, or agglomerates of particles formed by the rearrangement process, which were held on the surfaces of the glass particles, move with them. When two RuO_2 particles or particle agglomerates come in close proximity due to the motion

generated by the glass sintering, they will be rapidly pulled together and held because the kinetics of the rearrangement process are very fast at these temperatures. As the temperature approaches 550°C, the glass is in the intermediate stage of sintering where closed pores are being formed. In this temperature range, the glass-vapor interfacial area is decreasing very rapidly and with it the driving force for the rearrangement process, which means that the structure of the RuO_2 networks will not change appreciably above 550°C. The final stage of glass sintering begins at temperatures above 550°C and continues for the next two hundred degrees. At the lower temperature part of the region, the compressive stress on the resistor, resulting from the negative pressures in the closed pores as they contract, is the dominant force which leads to motion of the networks, but as the temperature increases, the motion of those pores filled with insoluble gas (bubbles) becomes more and more rapid because of the decreasing viscosity of the glass, and this produces a stirring action of the networks. When two RuO_2 particles in adjacent networks are brought into close proximity by this stirring action, they will remain in contact due to the net compressive force of the collapsing pores, and sintering by a solution-dissolution process will begin. As the temperature passes above 650°C, the sintering between adjacent RuO_2 particles becomes more and more rapid until at 800°C the initial stages of sintering between adjacent RuO_2 particles is completed in less than four minutes. RuO_2 particles which were in contact throughout the high temperature phase of the firing (greater than 700°C) will progress to the intermediate stages of sintering, whereas RuO_2 particles which came into contact with one another very late in the firing sequence will only develop minimal neck diameters, or no neck at all.

Because the motion of networks continues throughout the resistor firing there will be a spectrum of neck diameters between RuO_2 particles varying from necks which approach the size of the initial RuO_2 particles to those in which no neck formation has occurred and a glass film still separates the particles. At still higher temperatures and/or longer times Ostwald ripening becomes important. In this process, RuO_2 surfaces with high radii of curvature will preferentially dissolve into the glass matrix, and the dissolved RuO_2 will diffuse through the glass and reprecipitate on crystalline RuO_2 surfaces with smaller radii of curvature. The ripening will eventually lead to a disruption of the continuity of the RuO_2 networks. One of the goals of this project was to determine the influence of the resistor-substrate interaction on this microstructure development model.

The six physical processes responsible for this sequential microstructural development model are: sintering of the glass; spreading of the glass; rearrangement of the RuO_2 particles in the presence of glass; densification of the glass; sintering of the RuO_2 particles in the presence of glass; and Ostwald ripening of the RuO_2 in the glass. The materials properties which determine the kinetics of these six processes are: viscosity of the glass; surface tension of the glass; density of the glass; interfacial energy between the glass and RuO_2; solubility of RuO_2 in the glass; and surface energy of RuO_2. Five of these six materials properties, the exception being the surface energy of RuO_2, depend on the glass composition and will, in general, be influenced by the resistor-substrate interaction. The interfacial energy between the glass and RuO_2 is not a property which can be directly measured, but its change with glass composition should be small. The solubility of RuO_2 in the glass as a function of the amount

of dissolved substrate was determined under a previous contract [3]. The glass viscosity, surface tension, and density were measured as a function of amount of dissolved substrate during the present contract; the results of these studies are summarized in Table II.6.

The kinetics of the first three microstructure development processes (sintering of the glass, spreading of the glass, and rearrangement of the RuO_2 particles in the presence of glass) all depend on the ratio of surface tension to viscosity of the glass. The effect of glass composition on the surface tension to viscosity ratio was determined by neck growth measurements [2]. A statistical analysis gives the following dependence of the ratio (in m/s) on composition and temperature:

$$\frac{\gamma}{\eta}\left[\frac{15.217 - P}{72.46 + 1.544\ P^2}\right] \times 10^{32} \exp(-70690 \pm 2740/T) \qquad (2.30)$$

in which P is the w/o substrate dissolved in the glass. Equation 2.30 is valid only for temperatures below 570°C, but the three processes of interest are completed below that temperature. The ratio is decreased by a factor of 10 at any given temperature by the addition of 10 w/o substrate to the standard glass. However, due to the high activation energy required for the viscous flow sintering, and increase of 20°C in temperature of the glasses brings the ratio down by a factor of 10. Moreover, glass sintering is completed at around the softening point ($\sim$ 530°C) of the glass, and the interaction between the substrate and the glass at such low temperatures can be considered negligible (Fig. 2.16). The effects of substrate-resistor interactions on glass spreading and rearrangement of RuO_2 can also be considered insignificant because these two processes are also completed at

TABLE II.6. Summary of Glass Properties

Glass Composition	Viscosity at 850°C (Pa·s)	Surface Tension at 850°C mN/m	Reference Temperature (°C)				Density (gm/cc)	
			Annealing Point, T_a $\eta=10^{12}$ Pa·s	Softening Point, T_s $\eta=10^{6.6}$ Pa·s	Flow Point, T_f $\eta=10^{4}$ Pa·s	Melting Point $\eta=10$ Pa·s	At 25°C	At 850°C
Standard (63-25-12)	3.9	153.5	447.8	528.0	587.0	770	4.550	4.10
2 w/o Sub.	--	--	449.4	532.0	--	--	--	--
4 w/o Sub.	--	--	449.5	532.3	--	--	4.330	--
6 w/o Sub.	7.2	165.0	455.3	537.2	607.4	820	4.275	3.84
8 w/o Sub.	--	--	458.6	545.8	--	--	--	--
10 w/o Sub.	20.5	178.0	465.4	560.0	630.2	910	4.100	3.77
14 w/o Sub.	48.6	186.5	--	--	667.0	985	--	3.71

temperatures too low for any considerable substrate dissolution in the glass to occur.

The fourth microstructure development process, glass densification, can take place either by pore collapse if the gas in the pore is soluble in the glass, or by bubble release if the gas is insoluble in the glass. Densification by pore collapse is essentially complete at temperatures below 500°C, which are too low for any significant interaction between the glass and the substrate. In the case of densification by bubble release, which has been shown to occur over a considerable period of the firing cycle, the rate of densification depends on the rate of generation and the rate of elimination of the bubbles. The rate of movement of the bubbles towards the resistor-air interface under the influence of gravity can be determined [23] using Stoke's law

$$V_b(\rho_g - \rho_b)g = 6\, r_b\, \eta\, v \tag{2.31}$$

in which g is the gravitational constant; V_b, ρ_b, and r_b are the volume, density, and radius of the bubble, respectively; ρ_g and η are the glass density and viscosity, respectively; and v is the velocity of the bubble. If it is assumed that $\rho_g >> \rho_b$, Eq. 2.31 can be solved for bubble velocity to give:

$$v = \frac{2\, g r_b^2}{9} \left(\frac{\rho_g}{\eta}\right) \tag{2.32}$$

Since the final stage of RuO_2 network development occurs at the maximum firing temperature and depends on the stirring action caused by bubble motion, changes in the ratio of glass density to viscosity caused by substrate

dissolution must be considered. For resistors fired at 840°C for 15 minutes, the resistor glass will dissolve up to 14 w/o substrate according to Fig. 2.16. The data given in Table II.6 show that the ratio of glass density to viscosity decreases by a factor of 14 in going from the standard glass to the 14 w/o substrate glass at 850°C. A decrease in the bubble velocity by a factor of 14 would cause a significant decrease in the number of RuO_2 particles which come into contact late in the firing process. Thus, the distribution of neck diameters between RuO_2 particles will shift toward large neck diameters as a result of the resistor-substrate interaction. This effect is accentuated by the minor constituents of the substrate because a given amount of substrate dissolved in the glass is more effective in lowering the density (Fig. 2.7) and raising the viscosity (Fig. 2.3) than an equivalent amount of pure Al_2O_3. An alternate way of considering the effect of substrate dissolution on glass densification by bubble release is to calculate the escape time as a function of bubble size. For a 25 μm thick resistor, the maximum bubble radius that can be accommodated is 12.5 μm, and the escape time for this size is zero. A bubble of 5 μm radius will have to travel a maximum distance of 15 μm before it is released. Based on these arguments, the maximum time (τ) for release of a bubble can be determined as a function of bubble size by integrating Eq. 2.32.

$$\tau = \left(\frac{9}{2g}\right)\left(\frac{25 - 2r_b}{r_b^2}\right)\frac{\eta}{\rho_g} \tag{2.33}$$

$$\tau = 459\left(\frac{25 - 2r_b}{r_b^2}\right)\frac{\eta}{\rho_g} \tag{2.34}$$

Equation 2.34 gives τ in seconds for r_b in μm, η in Pa·s, and ρ_g in gm/cm^3.

The 14 to 1 ratio in η/ρ_g when going from the 14 w/o substrate glass to the standard glass at 850°C translates directly to the ratio of times required for release of the same size bubble. If Eq. 2.34 is solved for r_b at τ = 15 minutes, a nominal firing time at 850°C, the smallest bubble that would be released from the standard glass is 3.0 μm, while the smallest bubble released from the 14 w/o substrate glass would be 7.9 μm. Thus, the resistor-substrate interaction would lead to a much higher residue of bubbles in the fired resistor.

The fifth microstructure development process, sintering of the RuO_2 in the presence of glass, was discussed in Section 2.5. The model developed was based on a solution-precipitation mechanism, and it was argued that the most probable rate limiting step was redeposition at the neck. A consideration of the effect of the resistor-substrate interaction on the kinetics of this process led to Eq. 2.26; using the appropriate properties of RuO_2 in this equation gives:

$$x^3 = \left[\frac{5.327 \times 10^6}{1 + 0.172P + 0.00686P^2}\right] \frac{rt}{T} \exp(-49626/T) \qquad (2.35)$$

where x is the neck radius (cm) between RuO_2 particles of radius r(cm) held for time t (sec) at temperature T(K) in standard glass with P (w/o) dissolved substrate. The rate of neck growth is slowed by the resistor-substrate interaction, but the effect is not large. For example, for the same time, temperature and particle size, Eq. 2.35 predicts that the neck will be larger by a factor of 1.7 if the RuO_2 sintering occurs in the standard glass rather than 14 w/o substrate glass.

The final microstructure development process, the ripening of RuO_2 particles in the glass, was directly measured as a function of the amount of dissolved substrate in the glass, and the results were discussed in Section 2.4. It was concluded that the growth occurred by a phase boundary reaction controlled solution-precipitation process, and that the square of the average particle radius increased linearly with time according to Eq. 2.10. The parameters in the proportionality constant which depend on glass composition and temperature were evaluated, with the result given by . 2.16. Combining Eqs. 2.10 and 2.16 and inserting the appropriate properties of RuO_2 gives:

$$[\bar{r}(t)]^2 - [\bar{r}(0)]^2 = \left[\frac{5.024 \times 10^5}{1 + 0.172P + 0.00686P^2}\right]\frac{t}{T} \exp(-49626/T) \qquad (2.36)$$

According to Eq. 2.36, the ripening process is retarded by the resistor-substrate interaction because the rate of growth ($d\bar{r}(t)/dt$) will decrease by a factor of 5 as P increases from zero to 14. However, the ripening process is not a major contributor to the final resistor microstructure. For example, Eq. 2.36 predicts that after firing at 850°C for 15 minutes in the standard glass the average particle size of RuO_2 will have increased less than 1% for initial particle sizes greater than 11.5 nm.

The discussions in the preceding paragraphs of this section lead to the conclusion that the microstructure development model must be modified to take into account the resistor-substrate interaction, and that the primary modification must be in the kinetic equations for glass densification by bubble release (Eqs. 2.32 and 2.33). A minor modification must be

made to the equation for RuO_2 sintering kinetics (Eq. 2.35), while the other processes which constitute the microstructure development model are relatively uneffected by the resistor-substrate interaction.

3. ELECTRICAL EFFECTS

3.1 Resistor Studies

Four resistor pastes were prepared containing 5 w/o RuO_2 powder to 95 w/o glass powder. The glasses were the standard 63:25:12, and the substrate glasses containing 4, 6, and 10 w/o AlSiMag 614 substrate dissolved in the standard glass. A low weight percent conductive was chosen so that the maximum interaction between the substrate and each resistor glass could be observed. Since the densities of the glasses were different, the volume percent RuO_2 in each resistor ink was calculated and the results are given in Table III.1. Even though the volume percent only decreases by .32%, the sheet resistance could vary substantially because of the steep characteristic of the blending curve for low concentrations of RuO_2.

The organic screening agent was a solution of 10 w/o N-300 ethyl cellulose binder in 90 w/o butyl carbitol (diethylene glycol monobutyl ether) solvent. The pastes were made by blending approximately 40 v/o of the mixed powders with 60 v/o screening agent. Initial blending was done by hand before transferring to a roll mill. The spacing between rolls and the roll speed was kept constant during blending. The inks were left on the roll mill until the standard deviation of fired test resistors gave reasonably low values. Du Pont 9885 platinum-gold conductive was chosen to terminate the resistors based on the results of previous experiments [3].

Four resistors were placed on a ceramic tile (which was used for all subsequent resistor firings) and heated to .'0°C for 10 minutes to remove the solvent and any moisture that might have been adsorbed since screening. The tile with the resistors was placed in a box furnace for the appropriate

TABLE III.1. Volume Percent Conductive in 5 w/o RuO_2 Resistors

Glass	RuO_2 Resistors		Resistor Density gm/cm^3
	Weight Percent	Volume Percent	
STD	5	3.28	4.63
4 w/o Subst.	5	3.13	4.42
6 w/o Subst.	5	3.09	4.36
10 w/o Subst.	5	2.96	4.19

time, then removed and air cooled to room temperature. Substrates were weighed to determine the weight of the resistive film (difference from its pre-screened condition), and the resistor length and width were measured using a calibrated stage on a stereo microscope. Employing the density of the appropriate glass, the resistor volume was calculated. Dividing by the length and width gave an average thickness of the film. The firing temperature was set at 800°C and the firing time was varied from 3 to 22 minutes. At least three resistors of each glass composition were fired for each data point at a given time.

In addition to the measurements of hot and cold TCR described in a previous report [3], sample resistance and temperature were simultaneously recorded by an X-Y chart recorder. A constant current was established in the resistor by a high voltage supply and a precision metal film resistor. Thus, the voltage drop across the inner terminals of the device under test was directly proportional to its resistance. Because the sample resistances, in some cases, were relatively high, an operational amplifier was used as an impedance matching network to avoid circuit loading. Thermal equilibrium was maintained by submerging samples in a beaker of silicone oil and placing this assembly in an environmental chamber. The chamber was capable of thermostatic temperature regulation from -55 to +125°C. Sample temperature was measured by a chromel-alumel thermocouple clipped to the bottom of the resistor substrate.

Five resistors of each glass composition that were fired at 800°C for varying lengths of time were tested. The firing times were chosen so that the resistors would be in different stages of microstructure development. The results of these measurements are summarized in Figs. 3.1-3.4, where

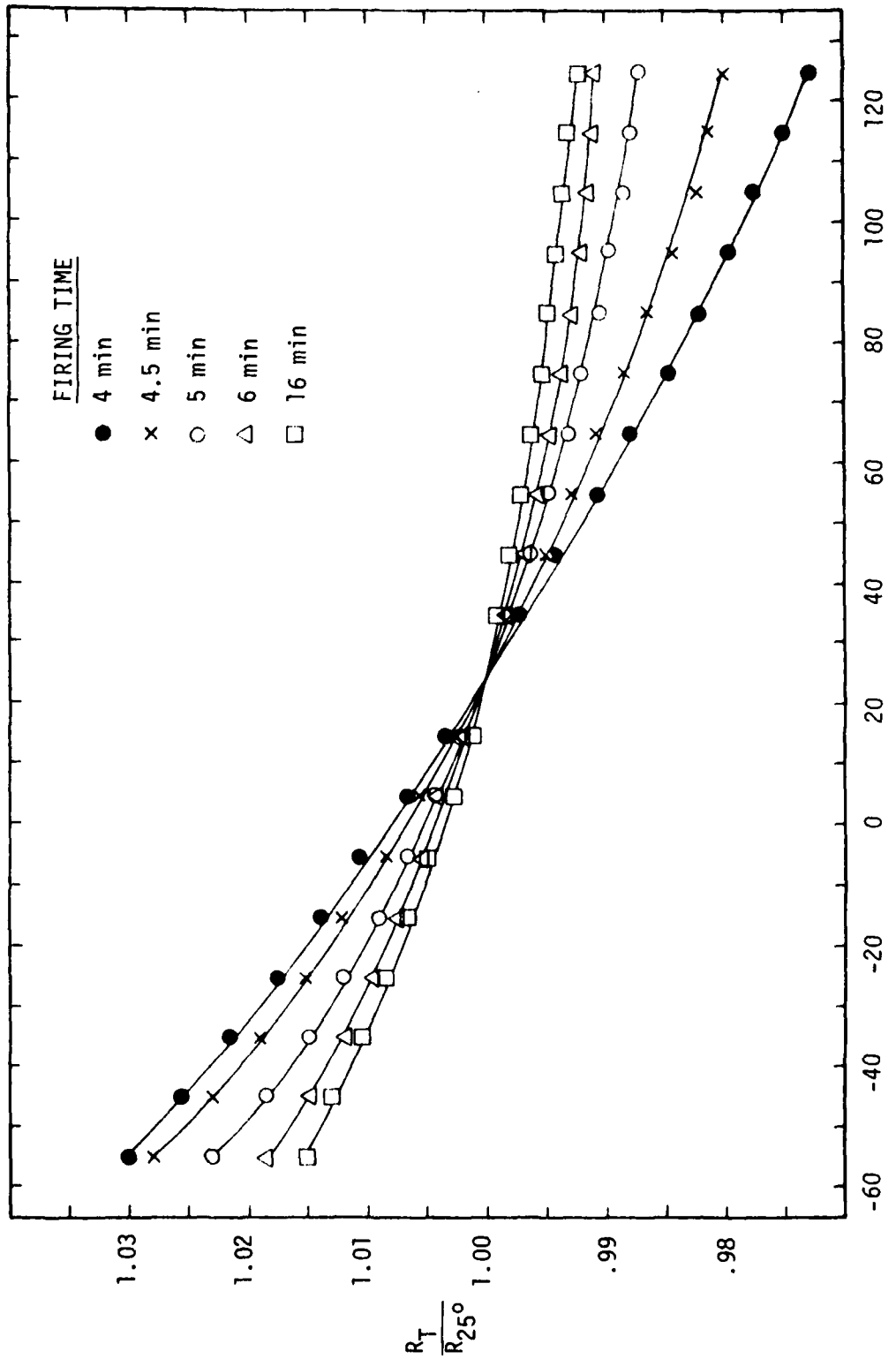

Figure 3.1. Temperature Dependence of Standard Glass Resistors Fired at 800°C.

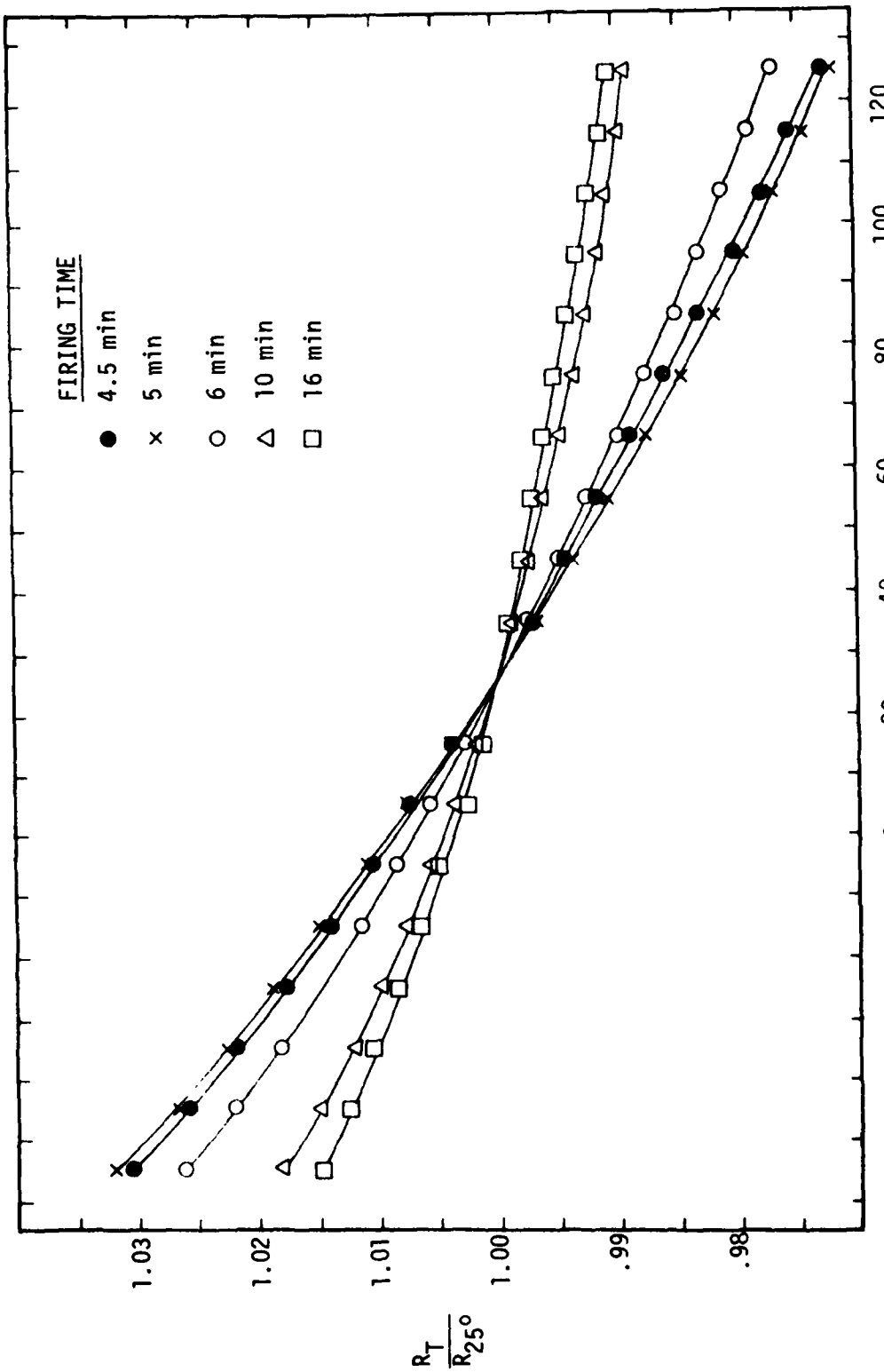

Figure 3.2. Temperature Dependence of 4 w/o Substrate Glass Resistors Fired at 800°C.

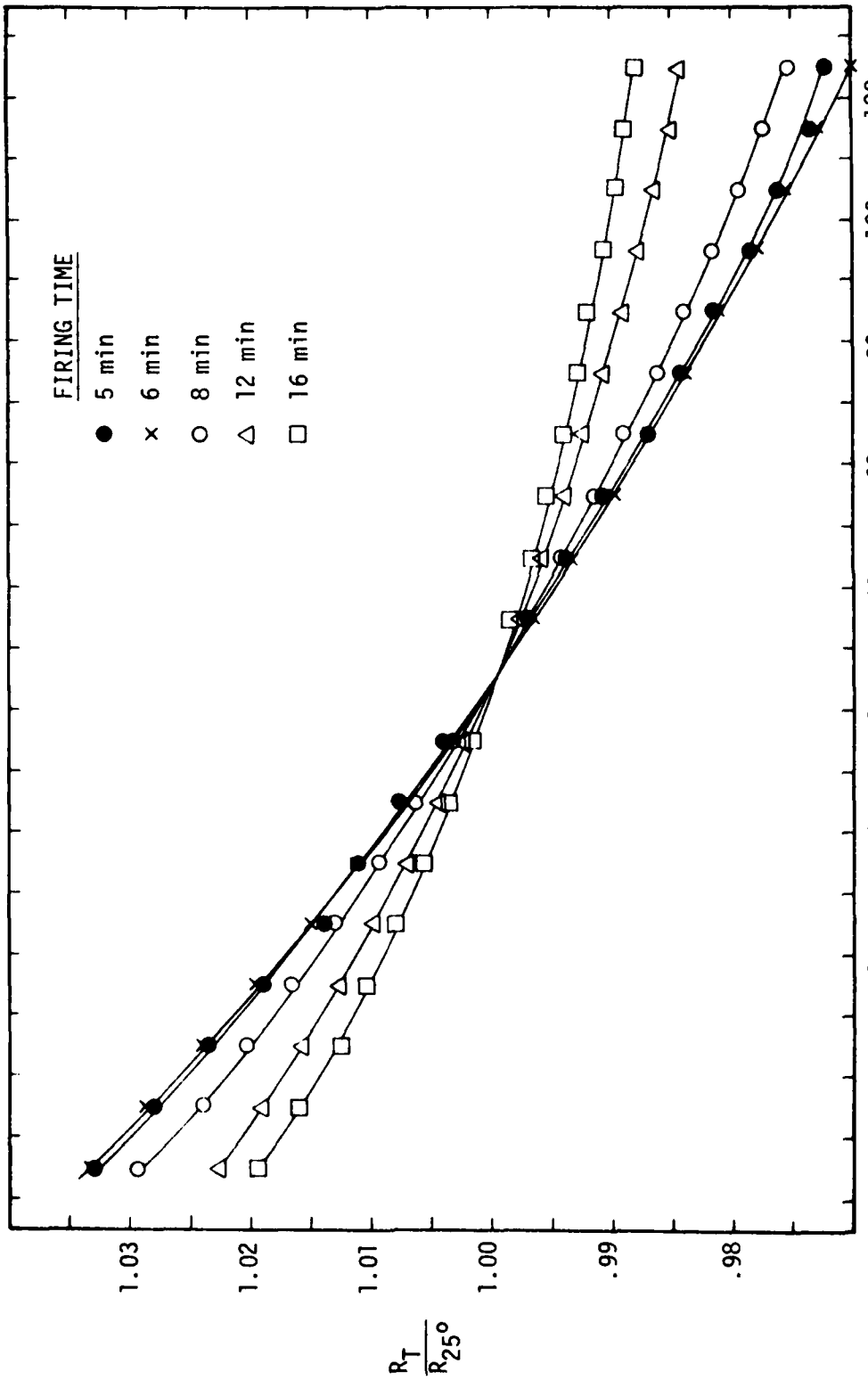

Figure 3.3. Temperature Dependence of 6 w/o Substrate Glass Resistors Fired at 800°C.

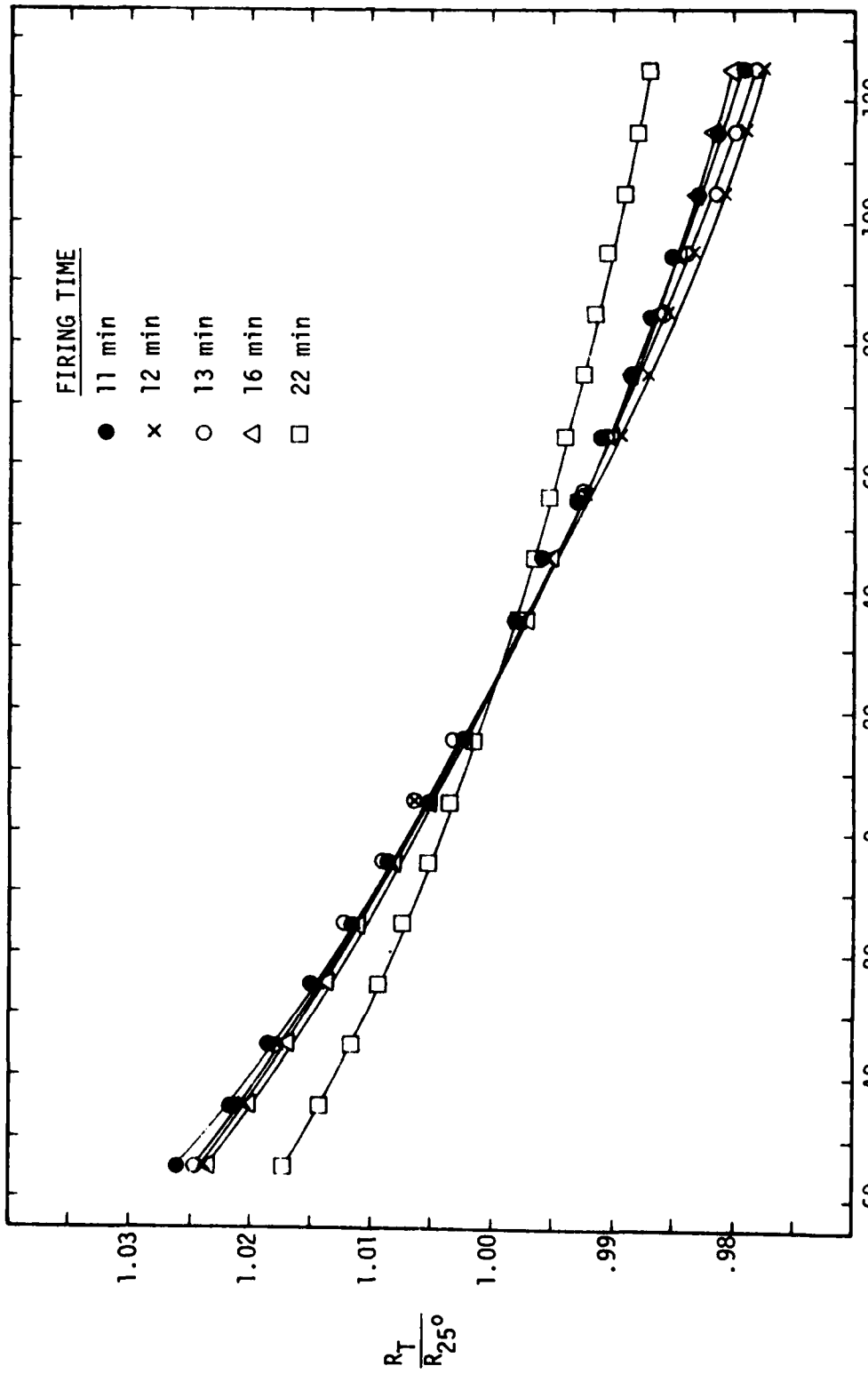

Figure 3.4. Temperature Dependence of 10 w/o Substrate Glass Resistors Fired at 800°C.

resistance normalized to its value at 25°C is plotted as a function of temperature. Each of these figures have very similar characteristics. The resistors fired for short times have a larger temperature dependence as demonstrated by the steeper slope of the resistance-temperature curves. As firing proceeds, the slope decreases. A second observation concerning these results is that each curve is concave up, implying that a minimum in resistance will occur at some temperature. For these formulations and firing schedules, it appears that resistance minimum temperature is above 125°C. If the conduction mechanism that dominates charge transport changes, for example, from a thermally activated process to a metallic conduction process, a minimum in resistance would be expected.

3.2 MIM Studies

3.2.1 General

Thick film resistors contain multi-stranded networks of conducting particles [23]. A large number of these particles will be joined by sintered necks, but a significant fraction will be separated by a thin layer of glass, thus forming non-sintered contacts. As a result of the firing process, the non-sintered contacts will have a continuous range of glass barrier thicknesses, from a few atomic layers to several thousand atomic layers. In addition, there could also be compositional variations and impurities present in the glass films due to substrate dissolution during firing. Because of the variance of the film thickness and composition, electrical conduction through the non-sintered contact may occur by more than one mechanism. For example, a tunneling mechanism may be important for very thin films, but as the tunneling resistance increases exponentially with film thickness, another mechanism such as Schottky or Frenkel-Poole emission may dominate.

In order to develop a complete model for charge transport it is necessary to be able to predict the conduction through the non-sintered contacts as a function of film thickness and glass composition. The achievement of this goal was complicated by the fact that there are no experimental techniques available to measure the conduction mechanisms in these "micro" contacts as they appear in thick film resistors. However, the geometry of a non-sintered contact is similar to a parallel plate capacitor, where the conducting particles represent the metal plates, and the glass layer corresponds to the dielectric. Thus, the MIM structure lends itself very well to the study of conduction in thin films. Ideally, the metal electrodes of the MIM device should be the same composition as the conducting phase in the thick film resistors (RuO_2 in our case). This ideal geometry could not be realized because RuO_2 cannot be deposited as a coherent film by any known means, and gold electrodes were substituted. The principal effect of changing electrode materials will be the differences in work functions, which enters into several charge transport mechanisms.

3.2.2 Fabrication

The glass films for the MIM devices were deposited by rf sputtering from a specially prepared target. Two glass compositions were used in the MIM devices: the standard glass (63 w/o PbO-25 w/o B_2O_3-12 w/o SiO_2), and the standard glass with 10 w/o AlSiMag 614 substrate dissolved in it. The targets were made by melting the glass in a platinum crucible followed by casting in a stainless steel mold. The targets were examined for cracks, devitrification, or impurities, and then annealed at 450°C for a minimum of two hours to relieve any strains which may have been introduced from the

casting operation. The final step in target preparation was to bond the glass with a conducting epoxy cement to an aluminum blank which could be mounted in the sputtering system.

Because of the extremely thin films (typically < 35 nm) that were sputtered, substrate preparation was a very critical step in the fabrication of the MIM devices. Polished, single-crystal silicon wafers (commonly used in integrated circuit fabrication) were chosen for the substrate material. Following an initial cleaning procedure, the wafers were oxidized at 1100°C for one hour. The resulting 110 nm SiO_2 layer was needed to isolate the lower electrode of the MIM structure from the silicon, both electrically and physically. Following the oxidation step, the wafers were metallized on one side by vacuum evaporating a layer of chromium [$\sim$ 50 nm) immediately followed by a layer of gold ($\sim$ 50-100 nm) to serve as the bottom electrode. The chromium interlayer was used to aid adhesion between the SiO_2 and gold. The wafers were placed in an rf sputtering unit approximately 5 cm from the target with a movable shutter positioned between the two. To initiate a sputtering run, the vacuum chamber was backfilled to 1.6-2.1 Pa with a 50:50 mixture of Ar and O_2, and the plasma ignited. After the plasma had been on long enough to insure that a constant composition was being sputtered from the glass target, the shutter was opened for the length of time required to produce the desired film thickness.

Employing the same vacuum system and procedures used for the Cr-Au bottom electrodes, gold counter-electrodes were deposited in a dot pattern on the glass film by evaporating through a metal mask. Chromium was not used for the counter-electrodes because the structure desired was Au-glass-Au, not Au-glass-Cr, and the chromium was not needed for adhesion to the glass.

Following metallization, the wafers were scribed with a diamond stylus into chips approximately 0.5 cm X 0.5 cm and each chip was etched to remove the glass from the edges, thus allowing the bottom electrode to be exposed. Following the etching procedure, devices were annealed at 440°C for 15 minutes in an oxygen atmosphere; the experiments used to determine the optimum anneal time and temperature will be discussed in Section 3.2.3. Samples that were to be temperature cycled were mounted on 8-pin, gold coated headers using a small quantity of conducting epoxy.

The sputtered glass thickness was measured with an optical interference instrument using monochromatic sodium light (λ = 589 nm). The film thickness, s, was determined by the amount of offset in the interference lines relative to the separation of adjacent lines. The error in measuring very thin films (< 35 nm) can be quite large; however, this proved to be the only available way of measuring s. Profilometry techniques were unsatisfactory due to the scratching of the soft glass by the stylus, interferometer measurements require a more complete understanding of the refractive index to be useful, and capacitance measurements require a knowledge of the variation of the dielectric constant with thickness.

It was found that there was a good correlation between sputtering time and film thickness, especially for the thicker films (> 50 nm). Holding the power and pressure constant, a constant sputtering rate could be achieved, and the sputtering time required for a desired thickness was easily calculated. However, as the sputtering times were shortened, the sputtering rate varied due to flucuations in the rf power during the initial tuning and to a change in the sputtering efficiency resulting from initial charging of the target and substrate.

In addition to the MIM devices, bulk glass capacitors were made from the two glass compositions, standard and standard with 10 w/o substrate added. The glasses were melted in platinum crucibles at 900°C and poured into heated stainless steel molds. The molds were allowed to cool to room temperature, and the casting examined for cracks, bubbles, or devitrification. Good quality glass blanks were then annealed at 450°C for a minimum of two hours in air. Cylinders, 16.3 mm and 7.5 mm diameter, were cut from the blanks using a diamond core drill, and then sliced into 0.3 to 0.8 mm thick sections using a slow speed diamond saw. The samples were then polished and provided with evaporated gold electrodes.

3.2.3 Anneal Experiments

After the gold counter electrode deposition, the films were annealed to reduce some of the damage done during the sputtering operation. Sputtering is a high energy process which can induce stresses in the film due to the impact of accelerated ionized particles, and some of the constituent oxides in the target may dissociate during deposition even though maintaining a partial pressure of oxygen during sputtering will reoxidize a portion of these. In addition, the density of the film may be lower than that of the bulk glass because of the random orientation of depositing glass units.

Annealing times and temperatures were selected with reference to the results of the studies of viscosity as a function of temperature and composition presented in Section 2.1.2. The devices were annealed by placing the chips in a fused quartz boat, and heating in a fused quartz-lined furnace at 380°C to 440°C under a constant oxygen flow. The anneal times investigated at 380°C were 30 minutes, 1, 2, 4, 6, and 8 hour accumulative, that

is, a one hour anneal was the initial 30 minutes plus a second 20 minute anneal after electrical testing.

Devices under test were placed on a vacuum chuck in a light-tight, grounded metal box. A micropositioner with a spring-loaded probe was used to make contact to the lower electrode at a corner of the sample where the glass had previously been etched away. A second micropositioner with a spring-loaded probe was used to make contact to the top electrodes of the devices. The complex admittance of each device was measured from 100 Hz to 100 kHz with a transformer ratio arm bridge.

The results of the anneal experiments were presented in an earlier report [3]. Overall, there was an improved electrical behavior for annealed devices over unannealed ones. The capacitance changed very little, but the conductivity and the dissipation factor decreased as the anneal time increased. After a certain amount of annealing had been done, further processing had little effect. Based on these results, two anneal time-temperature cycles were selected for this work: 30 minutes at 380°C or 15 minutes at 440°C.

3.2.4 AC Conductivity and Dissipation Factor

The parallel conductance and capacitance of the MIM devices were measured from 100 Hz to 100 kHz. Figures 3.5 and 3.6 are plots of the parallel conductivities versus the log of the frequency for various thicknesses of the glass and 10 w/o substrate glass films respectively. The slope of each curve is approximately one. In general, the conductivity increased as the thickness decreased, with the only exceptions to this trend being the 7 nm, 10 w/o substrate glass film and the standard bulk glass.

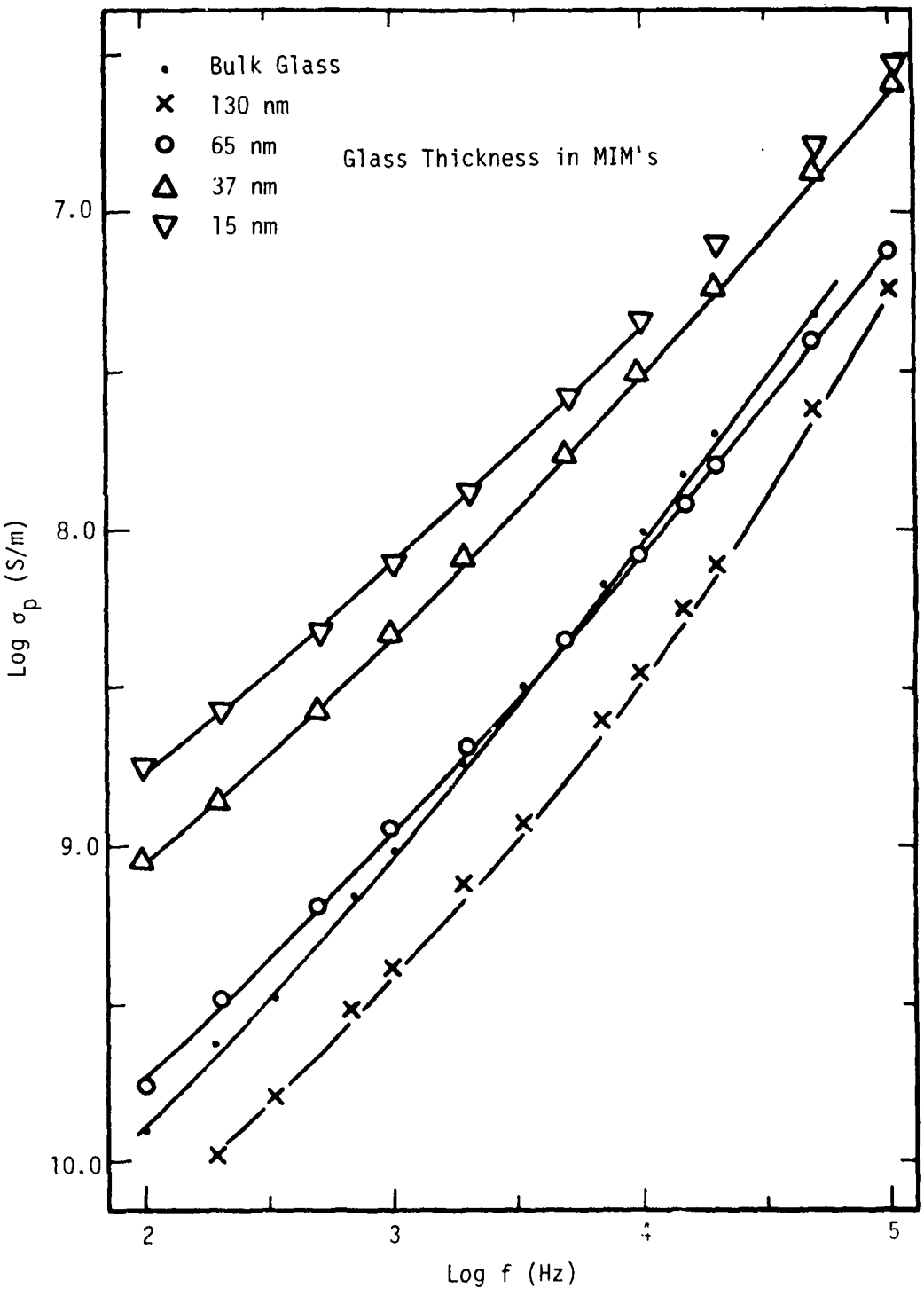

Figure 3.5. Parallel Conductivity as a Function of Frequency and Film Thickness for Standard Glass Devices.

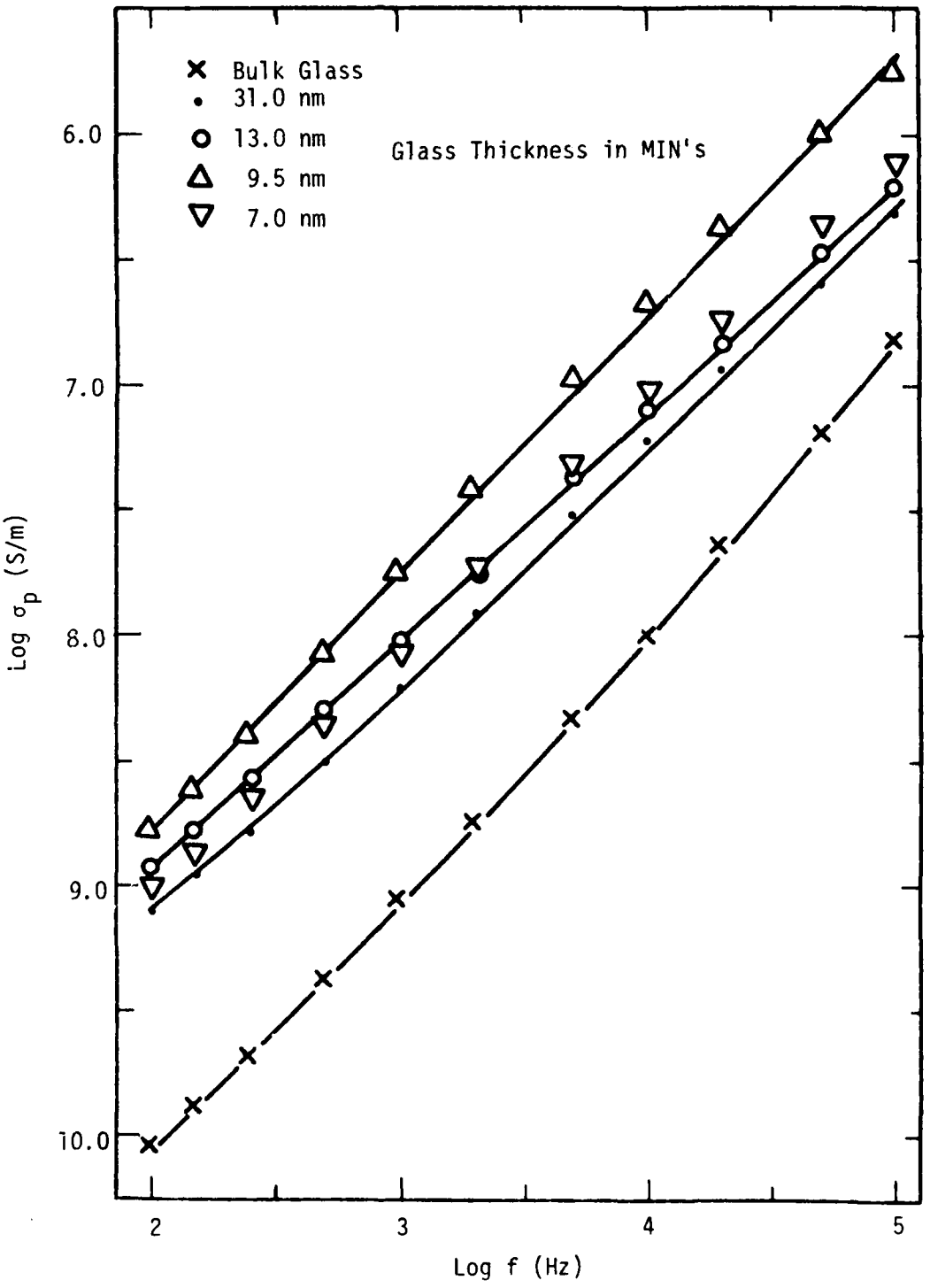

Figure 3.6. Parallel Conductivity as a Function of Frequency and Film Thickness for 10 w/o Substrate Glass Devices.

The three thinnest 10 w/o substrate glass samples were sputtered for 2 minutes, 1 minute, and 40 seconds, yielding calculated film thicknesses of 13.0, 9.5, and 7.0 nm respectively. Because the conductivity of the film calculated to be 7.0 nm thick was lower than that for the film calculated to be 9.5 nm thick, it would have been desirable to make a direct measurement of film thickness; however, the films were too thin to get good interference patterns. It is, therefore, possible that the actual film thicknesses were different from those calculated. It is also possible that the change in conductivity was caused by a change in the physical properties of the glass because compositional variation of the glass within the area of the electrodes becomes more probable for ultra-thin films.

The dissipation factor curves of Figs. 3.7 and 3.8 for the standard and 10 w/o substrate glass devices reveal an increasing D as film thickness decreased. For the standard glass, there was approximately a 1 1/2 order-of-magnitude difference between the bulk sample and the 15 nm sputtered film. In addition, the bulk and 130 nm samples both displayed a broad minimum. The 65 nm sample also appeared to be approaching a minimum at a frequency just above 100 kHz, while the 37 and 15 nm films demonstrated a much stronger decreasing dependence of D on frequency. The dissipation factor for the 10 w/o substrate glass in Fig. 3.8 displayed a somewhat different character than the corresponding curves for the standard glass. The 10 w/o bulk glass was similar to the standard glass samples in that it also had a minimum, but the sputtered films had both minima and maxima over the frequency range tested. The minimum occurred at $\sim$ 400 Hz for the 7.0 nm, and $\sim$ 180 Hz for the 9.0 nm films. The maximum occurred at $\sim$ 5600 Hz for the 31 nm, $\sim$ 12,600 Hz for the 7 nm, and $\sim$ 20,000 Hz for the 9 nm films.

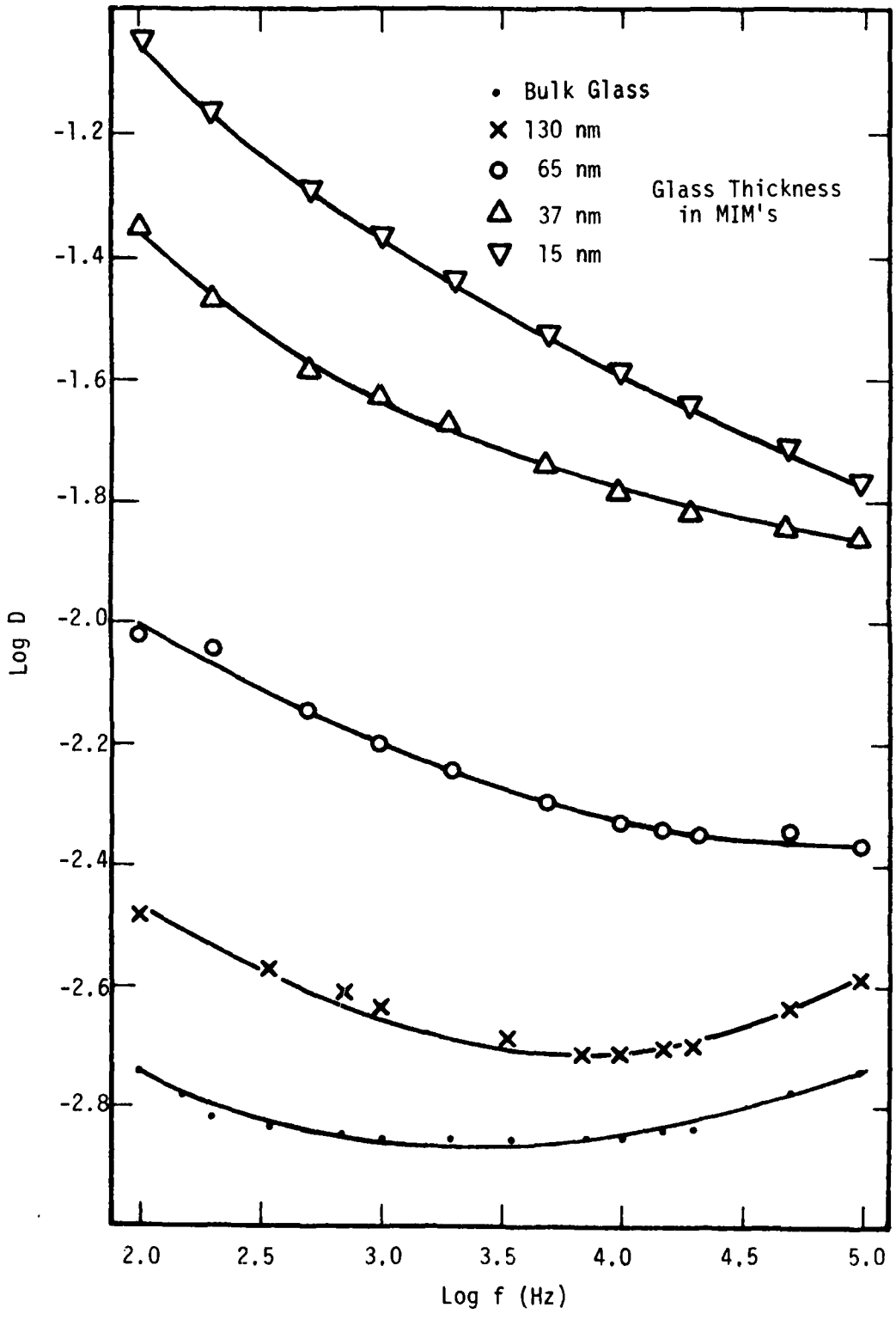

Figure 3.7. Dissipation Factor as a Function of Frequency and Film Thickness for Standard Glass Devices.

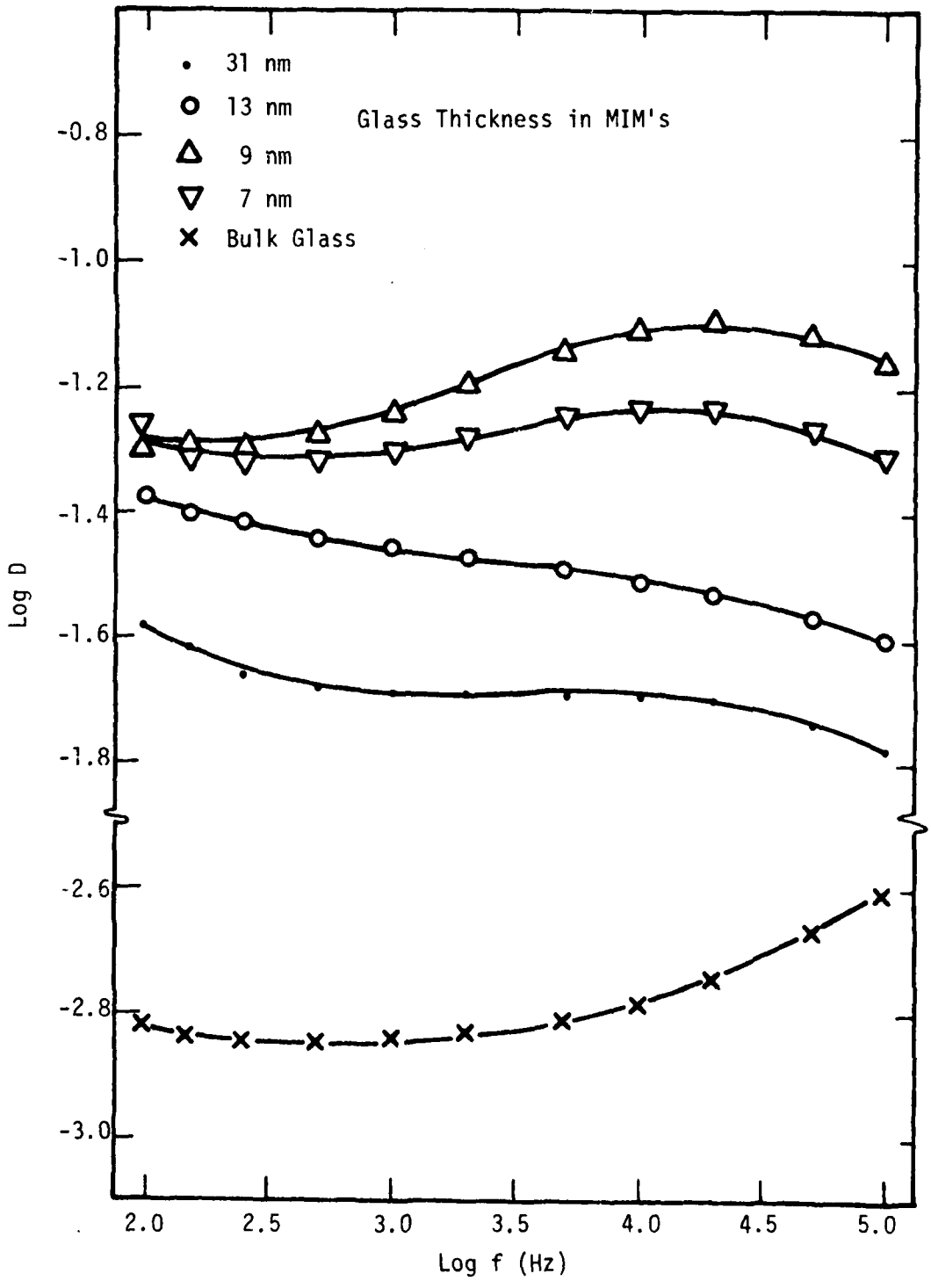

Figure 3.8. Dissipation Factor as a Function of Frequency and Film Thickness for 10 w/o Substrate Glass Devices.

The complex admittance results can be attributed to localized conduction resulting from the physical damage done by sputtering. As the thickness increases, the number of localized conduction sites will decrease. The increasing dissipation factor for decreasing frequency at low frequency can be ascribed to dc conduction losses.

3.2.5 Dielectric Constant and Dielectric Breakdown

The dielectric constant, k, and dielectric strength, E_b, were measured for all glass compositions and thicknesses. The dielectric constant was determined by measuring the capacitance at 1 MHz, and the breakdown field strength was measured by applying a dc bias to the 1 MHz capacitance meter until breakdown occurred. The results of these experiments appear in Table III.2 for all thickness of both glass compositions. Included with k and E_b is also the capacitance per unit area, and the average thickness, s. It is interesting to note the variation of the dielectric constant with decreasing film thickness; for the standard glass MIM's, k decreased from 3.4 to 2.8 and then increased to 4.3, while for the 10 w/o substrate glass, k decreased monotonically from 5.4 to 2.5. This variation could be due to structural discontinuities in the glass. The dielectric strength remained essentially constant for each composition as the thickness varied, but the 10 w/o substrate glass breakdown field was over twice that of the standard glass for similar thicknesses. The fact that the bulk glass sample's dielectric constants of about 11 are twice the dielectric constants of the 10 w/o substrate glass MIMs and 4 times that of the standard glass MIMs could be due to thickness variations within the electrode areas of the MIMs.

TABLE III.2. Dielectric Constant and Dielectric Breakdown

Glass	s(nm)	C_p ($\mu F/m^2$)	k	E_b(V/m)
STD	130	233.	3.4	3.9×10^8
	65	408	3.0	2.8×10^8
	37	670	2.8	2.6×10^8
	15	2300	3.9	2.5×10^8
	10	3800	4.3	2.5×10^8
	Bulk GL	.240	11.5	-----
10 w/o Subst.	31	1540	5.4	4.0×10^8
	13	3030	4.4	5.1×10^8
	9.5	4000	4.3	5.8×10^8
	7.0	3180	2.5	5.7×10^8
	Bulk GL	9.70	11.2	-----

3.2.6 DC Measurements

3.2.6.1 Experimental: The thin film MIM's were very susceptable to many forms of failure. Chemically, the glass is etched by any acid or base, and even DI water will attack it slowly. Mechanically, the probe tips must be lowered gently, taking care not to load the springs too much and cause them to punch through. Electrically, transient noise of a few volts can cause fields high enough for breakdown. Several steps were taken to reduce the loss of devices. Line voltage noise was eliminated by using two electrometers and a power supply that were battery operated. The samples were biased by the power supply with the device voltage (V) measured by one electrometer and current (I) measured by the other.

Samples were tested in a vacuum system specially built for temperature cycling. A mechanical pump was used to keep the pressure at 6 Pa during testing. The MIM chips were inserted in a brass collar, which was attached to a larger brass block. The block was hollow and contained an inlet and an outlet for liquid nitrogen cooling. Under vacuum, the block could easily reach -180°C with a constant flow of LN_2. In addition to the cooling capabilities, a heating element was inserted below the cooling cavity.

The device's top electrode was accessed by a spring-loaded probe mounted to an x-y-z motion micropositioner. However, a problem was encountered with the probe due to the expansion and contraction of the brass block. As the system was cooled, the brass block contracted, causing the probe to lose contact with the device. During heating cycles, the block drove the probe into the device leading to breakdown. These physical limitations forced most of the temperature testing to be done between -20°C and + 50°C.

The dc analysis consisted of two basic experiments; measuring current as a function of voltage at a constant temperature, and measuring current as a function of temperature at constant voltage. All devices were fully annealed at 440°C unless otherwise noted. The dc experiments were performed on both the 10 w/o substrate glass and the standard glass devices. However, because of breakdown problems associated with the standard glass, reproducable data could not be obtained for this dielectric at temperatures other than room temperature. Three dielectric thicknesses of the 10 w/o substrate glass were sufficiently thin to get measurable currents and reproducable data over several orders-of-magnitude of current and voltage.

3.2.6.2 Results and Analysis: In general, it was determined that the log of current density was dependent on the square root of voltage and inversely proportional to temperature. This was observed independent of film thickness, electrode metal (Au and Al), temperature, direction of the field, or glass composition. Figures 3.9-3.11 are plots of the log of current density versus the square root of voltage across the glass for three devices at room temperature. Figure 3.9 is a standard glass film 15 nm thick, Fig. 3.10 a 10 w/o substrate glass film 13.0 nm, and Fig. 3.11 a 10 w/o substrate glass film with Al as the top metal. Each curve is linear for almost 4 orders-of-magnitude in current, and there is no perceptable change in reversing polarity. As later results will show, the slope is dependent on film thickness, temperature and voltage.

The other interesting behavior associated with these results is the low field characteristic, where the current decreases rapidly with voltage. It was observed in all thicknesses tested for both glass compositions.

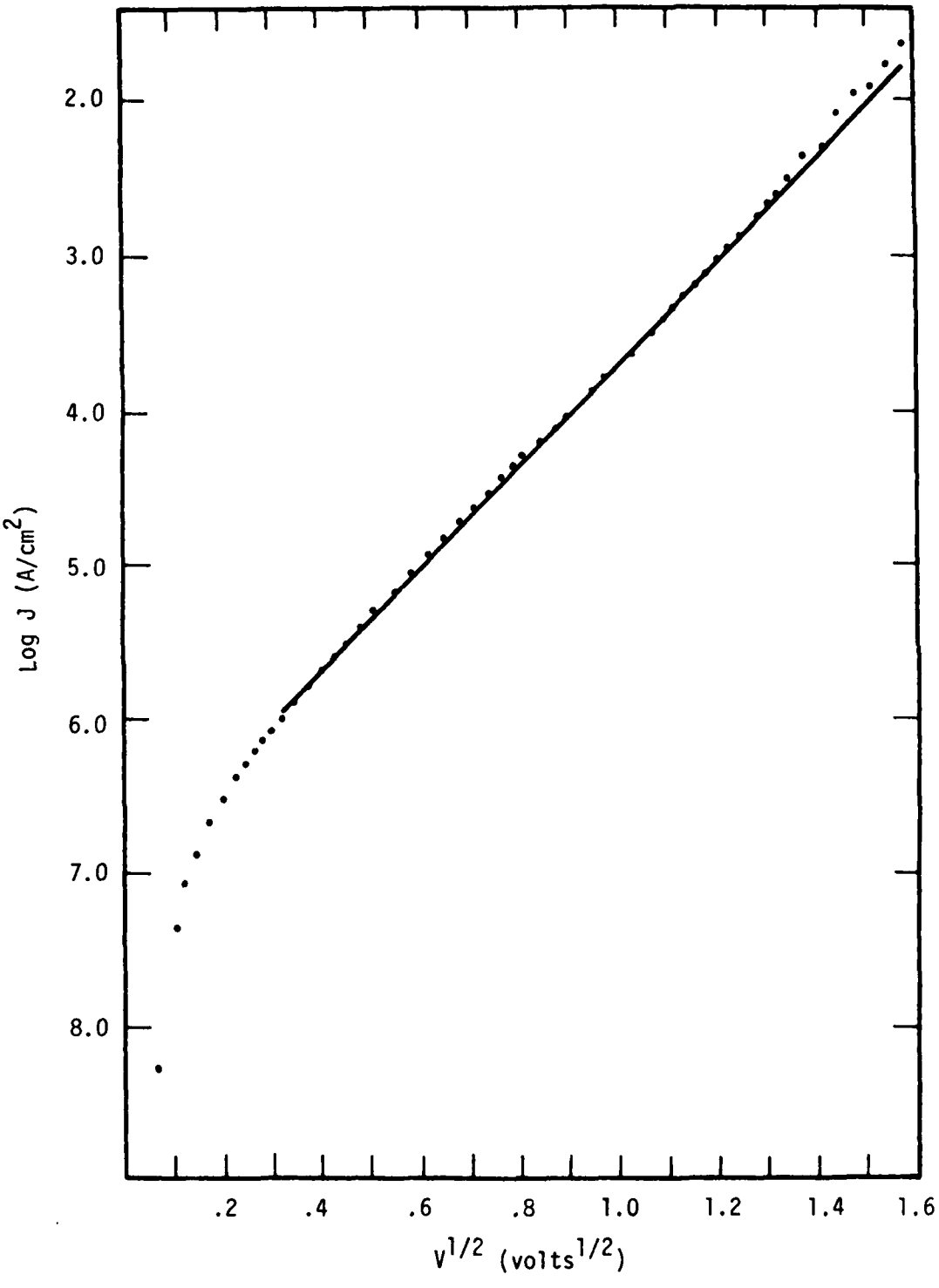

Figure 3.9. Current Density as a Function of Voltage for a Standard Glass (15 nm) MIM at 25°C.

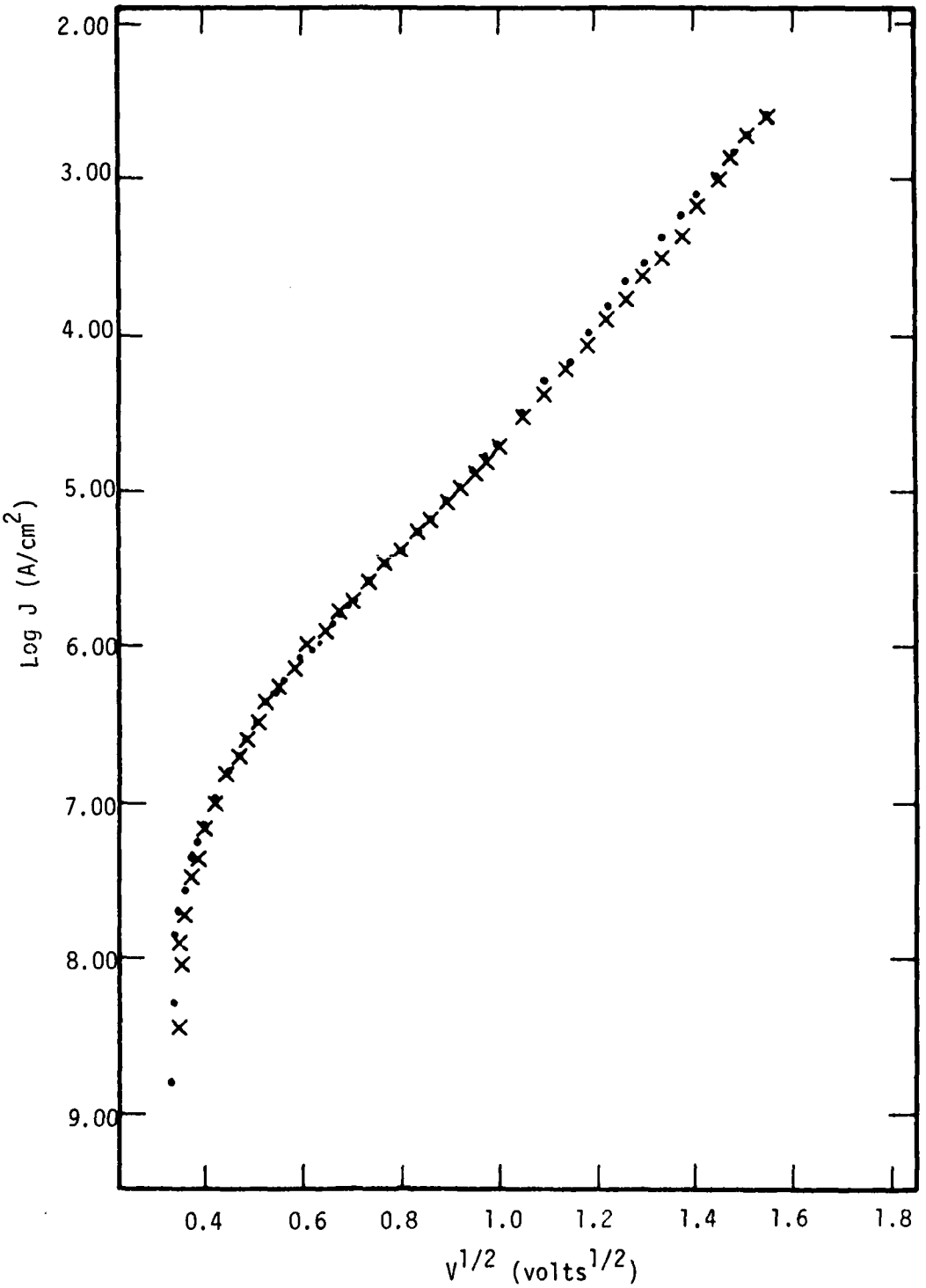

Figure 3.10. Current Density as a Function of Voltage for a 10 w/o Substrate Glass (13 nm) MIM at 25°C.

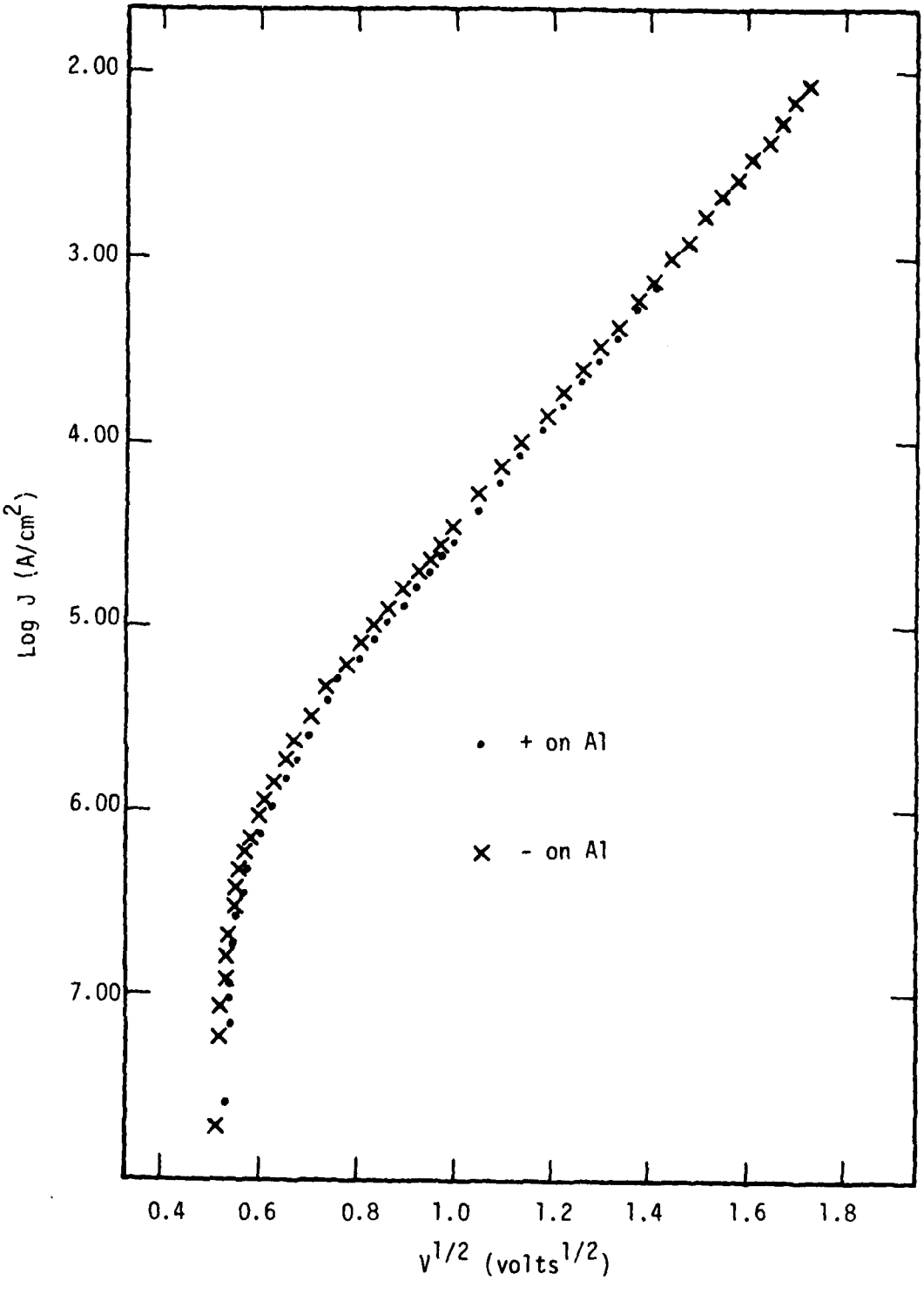

Figure 3.11. Current Density as a Function of Voltage for a 10 w/o Substrate Glass MIM with an Aluminum Top Electrode at 25°C.

Reversing polarity had no effect, nor did changing the top electrode metal. Gold and aluminum electrodes were used and a different threshold was observed for the two metals, but differences in threshold as large as this were observed for the same metal from sample-to-sample.

The anneal raised the dc current density of the film for a given voltage and in-so-doing improved the device stability. It is believed this was due to improving the interface between the top gold electrode and the glass. Figure 3.12 is a plot of the standard glass film current-voltage characteristic before and after the anneal. The anneal has shifted the curve-up by two orders-of-magnitude. The low slope region has not changed appreciably, but the steeper sloped region is no longer visible. This region has either been shifted up beyond the testing limits or it has been annealed out.

In Fig. 3.13, two 10.0 nm standard glass MIN's that were annealed at 380°C for 10 minutes, showed the same shape and position of the threshold voltage, but the magnitude of the current was different by 4 orders-of-magnitude. The slopes of the curves are almost identical to each other, but they are lower than the slope of the 15.0 nm films (Figs. 3.9-3.12) by about a factor of two. The lower conductivity sample was cooled down to -37°C, and the temperature was slowly decreased from that point. The x's on Fig. 3.13 represent points taken as the sample was cooled down to -60°C. These results are coincident with the room temperature values which suggests a temperature independent transport mechanism. Unfortunately, no other standard glass samples were tested successfully at varying temperatures because of the instability of the electrical characteristics.

The 10 w/o substrate glass devices were much more thermally stable and provided a great deal of information. Figures 3.14 and 3.15 show the

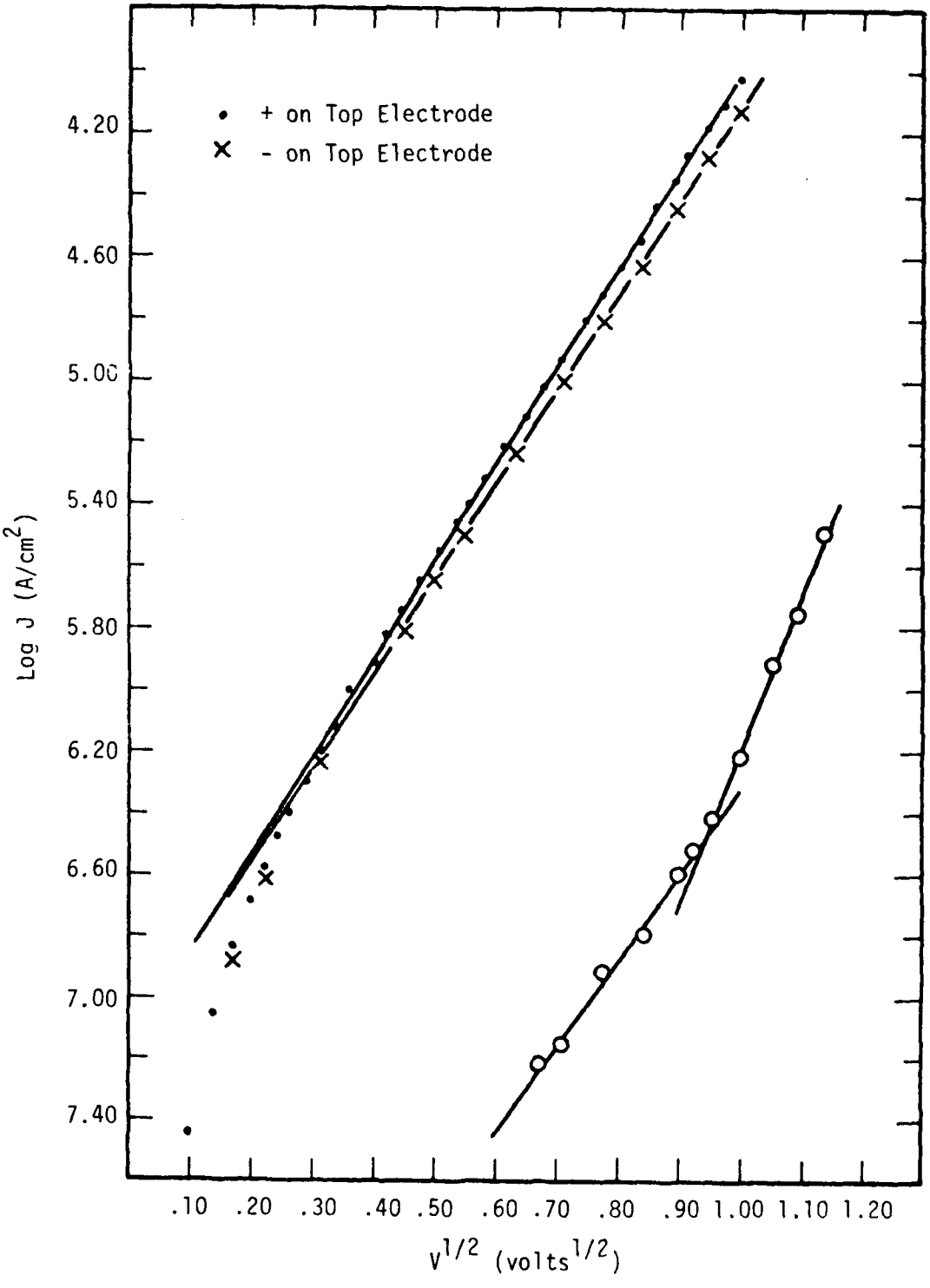

Figure 3.12. Current Density as a Function of Voltage for a Standard Glass MIM (15 nm) Before and After Annealing.

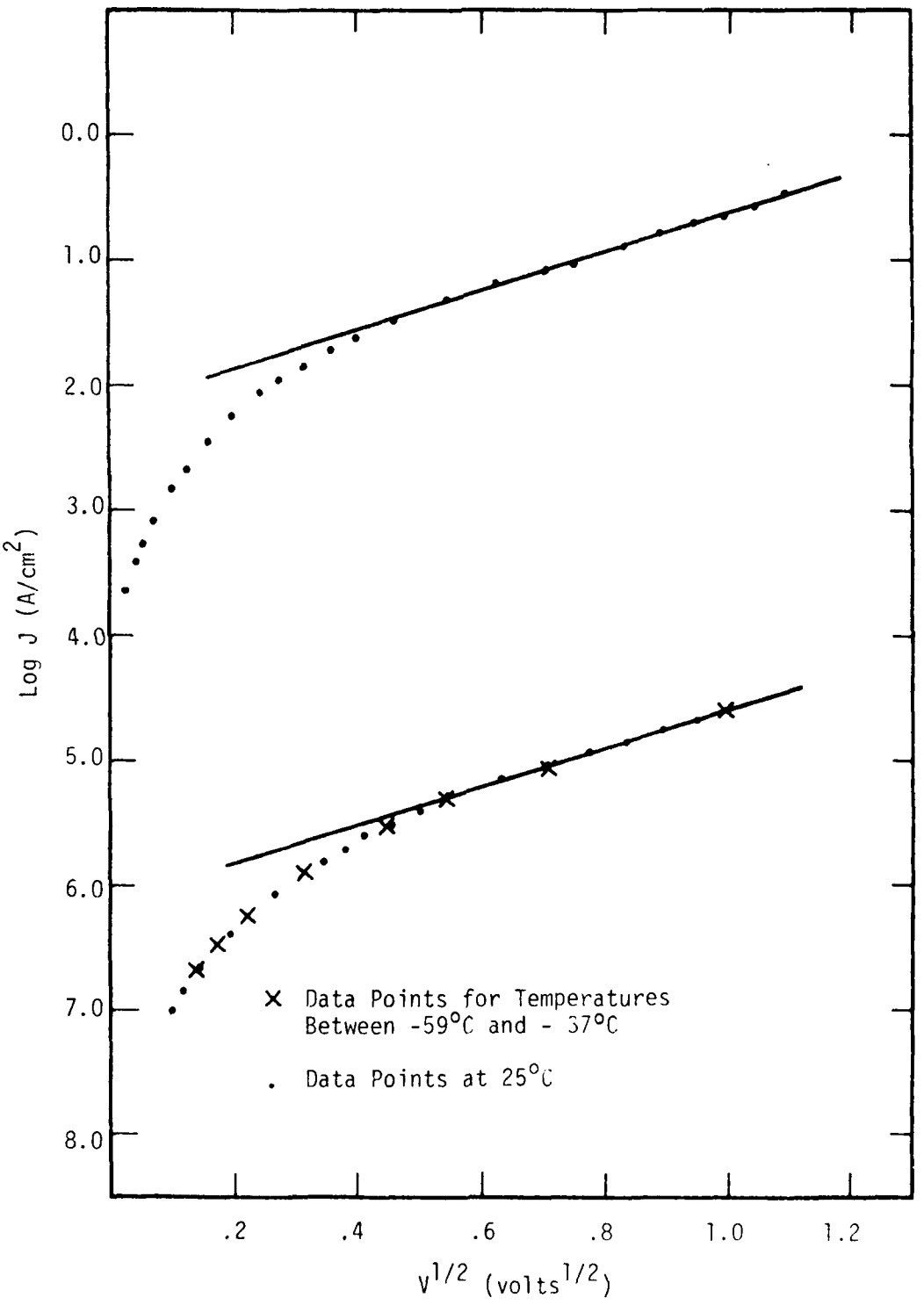

Figure 3.13. Current Density as a Function of Voltage for Two Standard Glass (10 nm) MIMs Annealed at 380°C.

AD-A084 261 PURDUE UNIV LAFAYETTE IN TURNER LAB FOR ELECTROCERAMICS F/G 9/1
THE EFFECTS OF SUBSTRATE COMPOSITION OF THICK FILM CIRCUIT RELI--ETC(U)
FEB 80 R W VEST N00019-79-C-0240
UNCLASSIFIED NL

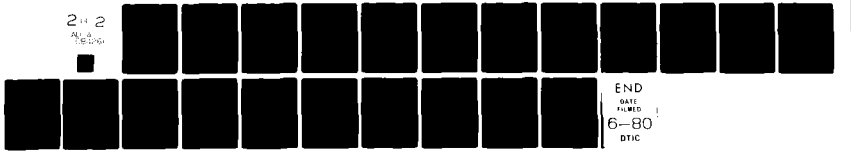

END
DATE FILMED
6-80
DTIC

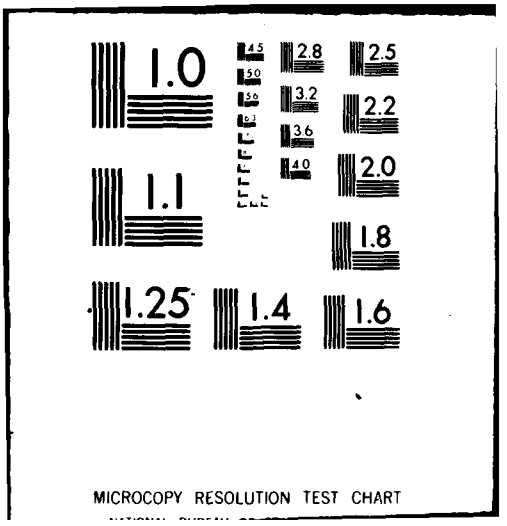
1.0
1.1
1.25
1.4
1.6
1.8
2.0
2.2
2.5
2.8
3.2
3.6
4.0
4.5
5.0
5.6
6.3
MICROCOPY RESOLUTION TEST CHART

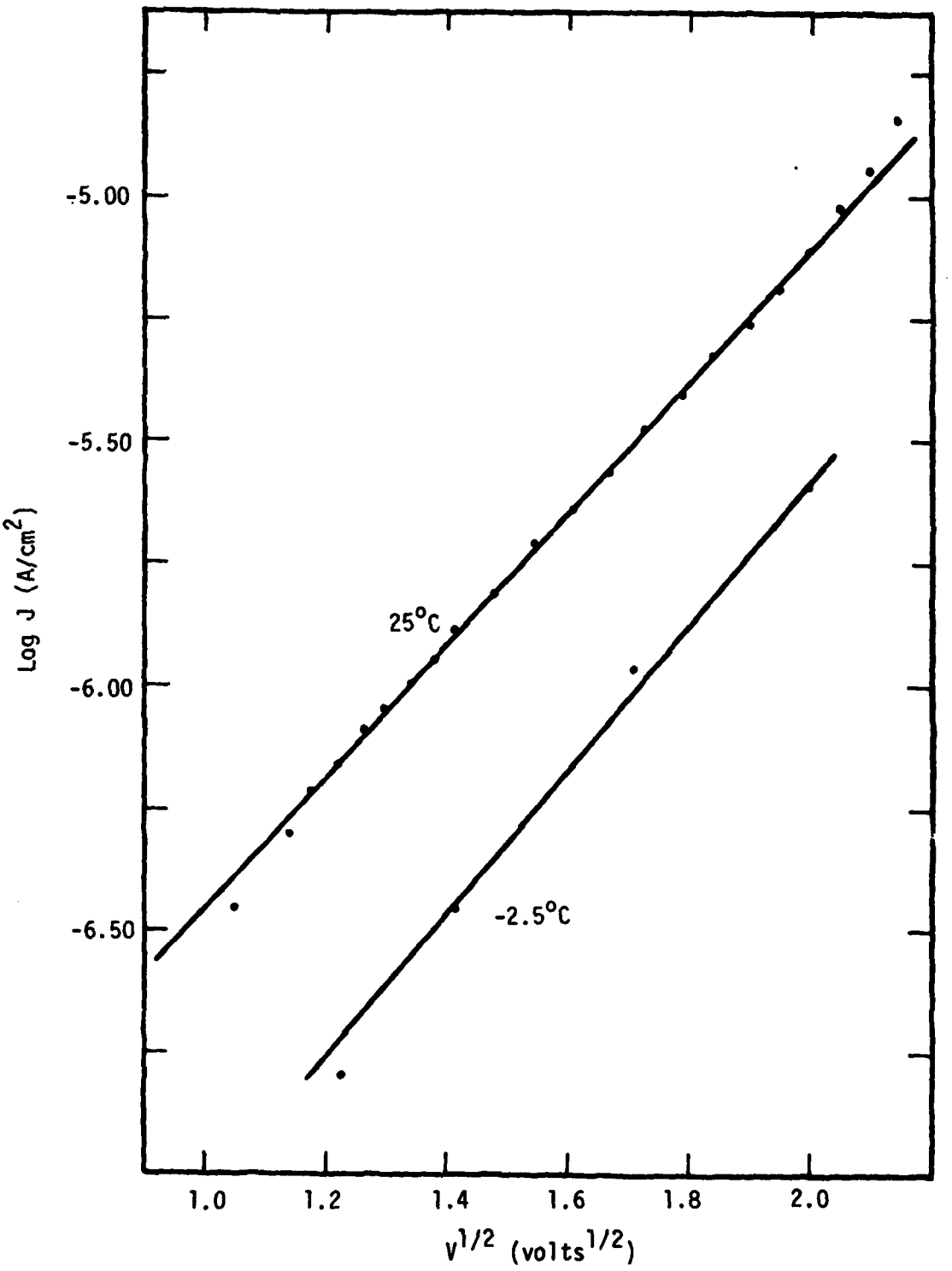

Figure 3.14. Current Density as a Function of Voltage for a 10 w/o Substrate Glass (13 nm) MIM at Two Temperatures.

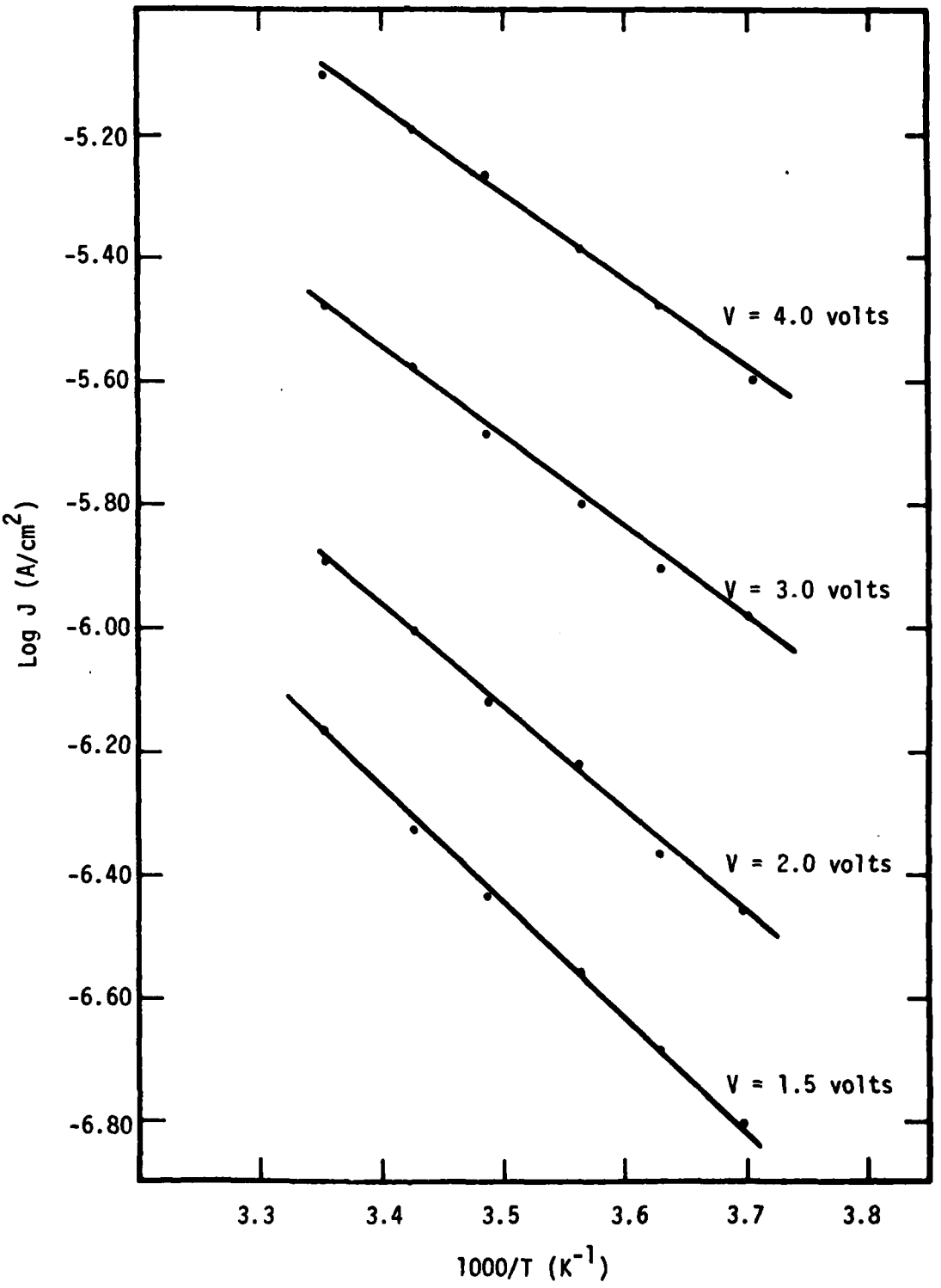

Figure 3.15. Current Density as a Function of Temperature for a 10 w/o Substrate Glass (13 nm) MIM at Four Voltages.

dependence of current density on voltage and temperature, respectively, for a 10 w/o substrate glass device that was 13.0 nm thick. The current-voltage data appear as straight lines at both 25° and -2.5°C, and the lower temperature curve has a higher slope than the room temperature one. In Fig. 3.15, the data for log of the current density versus 1000/T plot as straight lines at all four applied voltages, each with a successively lower slope for increasing V. Similar results of an experiment on a 9.5 nm, 10 w/o substrate glass film are presented in Figs. 3.16 and 3.17. Again, the slopes decrease for increasing temperature and increasing voltage, but a comparison of the room temperature curves of Figs. 3.14 and 3.16 shows that the slopes have increased for a decrease in film thickness.

The current-voltage and current-temperature results for 10 w/o substrate glass devices that were approximately 7.0 nm thick are presented in Figs. 3.18-3.21. In general, the characteristics are similar to the previously described results: linear plots of log J vs. $V^{1/2}$ and log J vs. 1000/T. However, additional information was obtained from these devices which warrants their inclusion. Figure 3.18 is a log J vs. $V^{1/2}$ plot that is linear over 4 1/2 orders-of-magnitude of current at room temperature and 3 orders-of-magnitude at 0° and 50°C. The slope of these three lines decreases for increasing temperature, but also note that the separation of the curves is not as large as previously observed in the thicker films. The temperature dependence is decreasing as the film thickness decreases. This becomes even more obvious when examining Fig. 3.19. The slopes of the log J versus reciprocal temperature curves are much lower than the corresponding slopes of the 13.0 and 9.5 nm films. Figure 3.20 shows the linearity of the 7.0 nm films and the decreasing slope for increasing temperature which is consistant

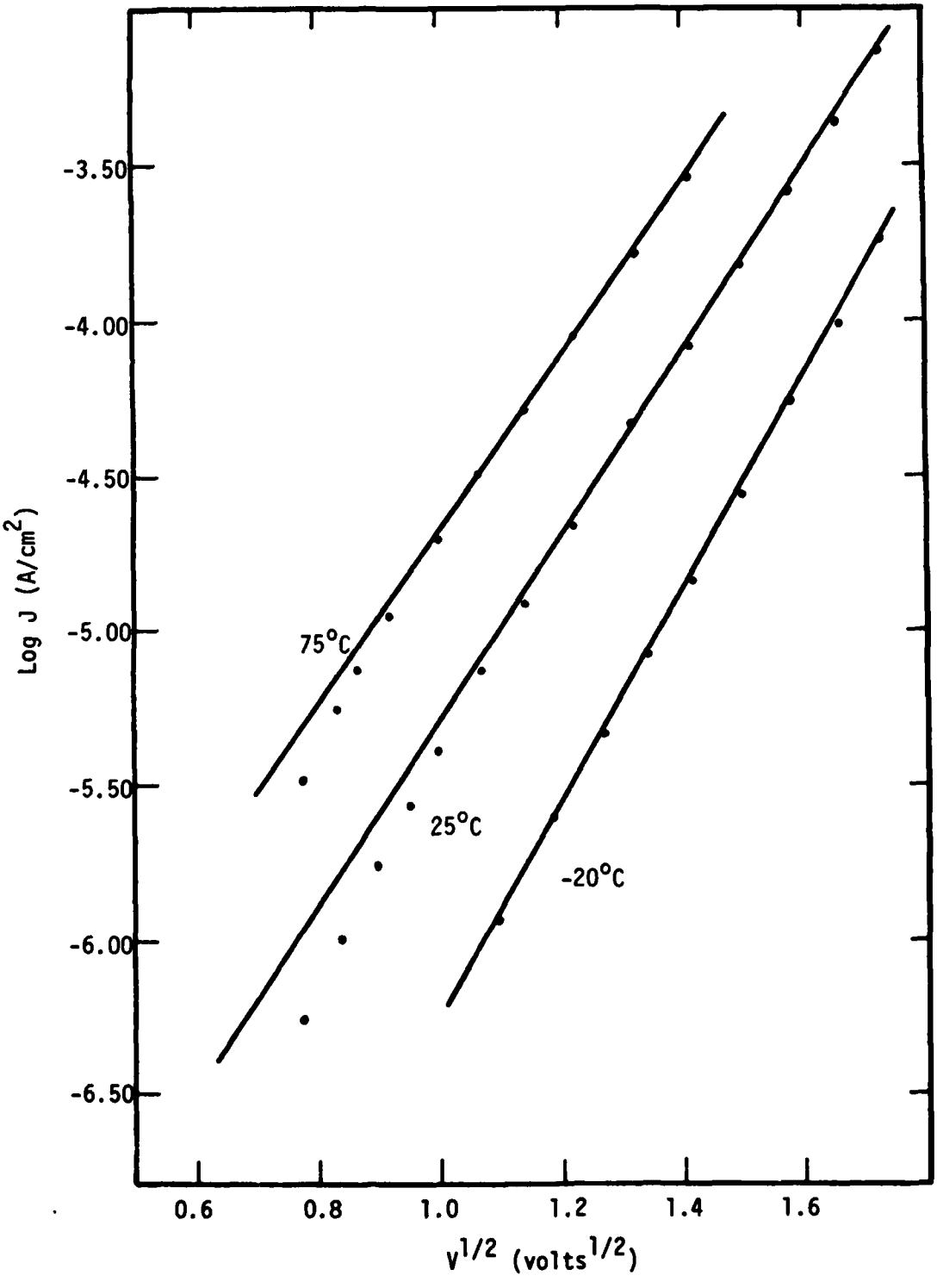

Figure 3.16. Current Density as a Function of Voltage for a 10 w/o Substrate Glass (9.5 nm) MIM at Three Temperatures.

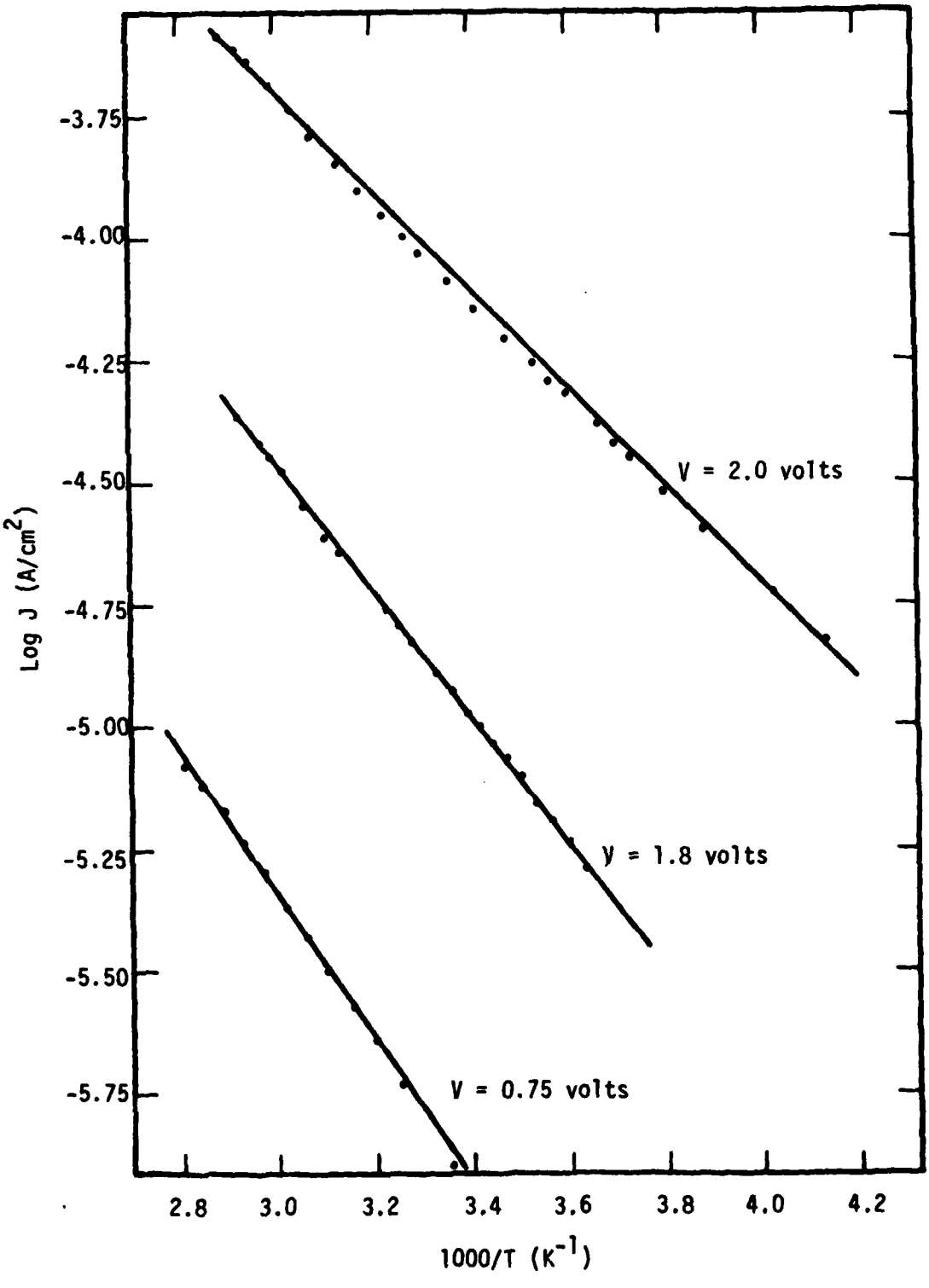

Figure 3.17. Current Density as a Function of Temperature for a 10 w/o Substrate Glass (9.5 nm) MIM at Three Voltages.

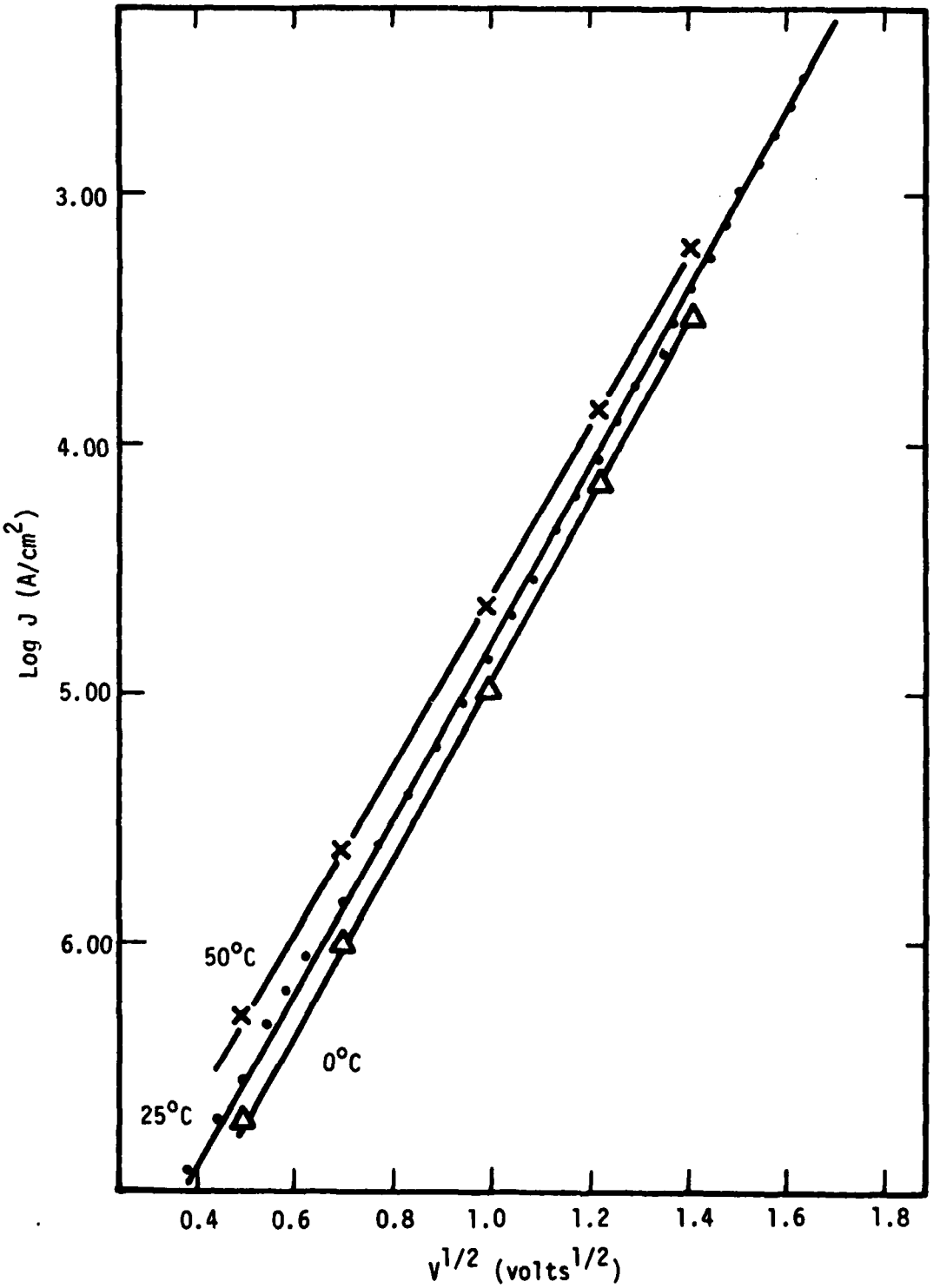

Figure 3.18. Current Density as a Function of Voltage for a 10 w/o Substrate Glass (7 nm) MIM at Three Temperatures.

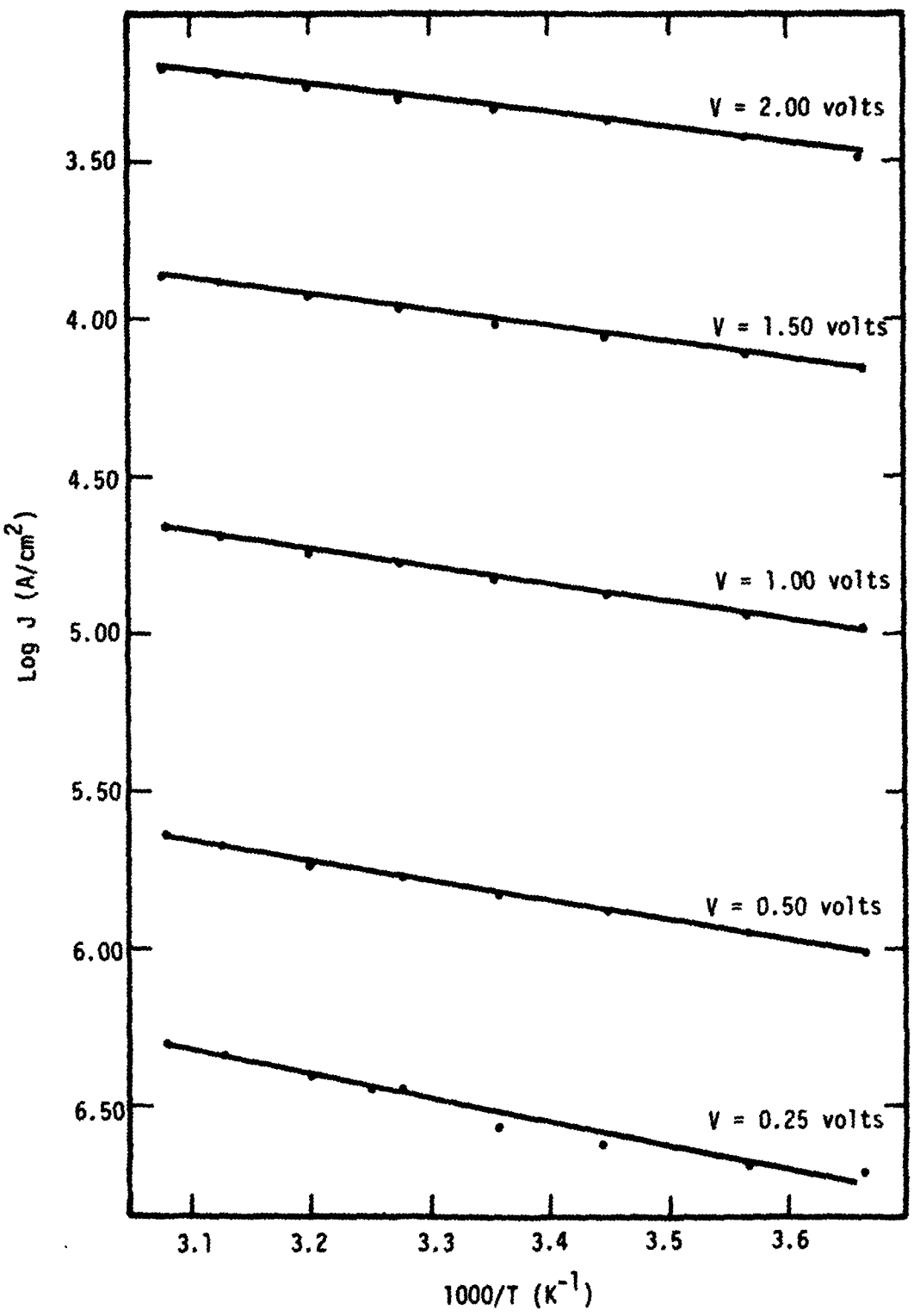

Figure 3.19. Current Density as a Function of Temperature for a 10 w/o Substrate Glass (7 nm) MIM at Five Voltages.

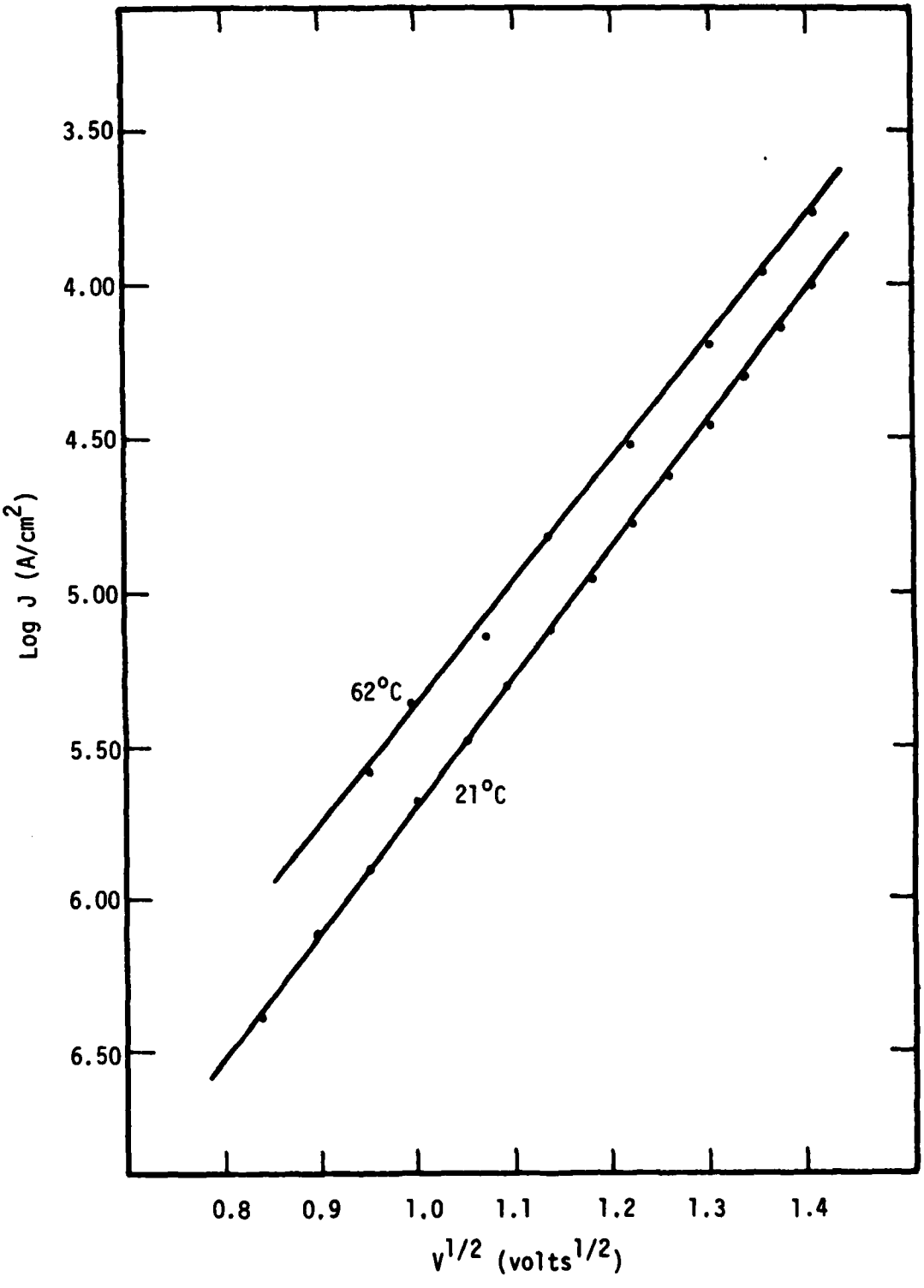

Figure 3.20. Current Density as a Function of Voltage for a 10 w/o Substrate Glass (7 nm) MIM at Two Temperatures.

with the previous results. However, the current-temperature plot of this device (Fog. 3.21) is noticeably different. Above room temperature the curve is a straight line with the predictably low slope, but at lower temperatures the current remains above the straight-line region. It may be postulated that the curve will level off at some point, and the device current would be independent of the temperature. For the given thickness and applied field, this would indicate a tunneling mechanism for charge transport.

The results of the current-voltage and current-temperature measurements have consistantly demonstrated that the log of device current is dependent on the square root of voltage and inversely proportional to temperature, and that the voltage dependence is much stronger than the temperature dependence. The straight-line plots of the log of the current density versus the square root of the voltage over several orders-of-magnitude of current emphatically suggest a Schottky emission or Frenkel-Poole emission mechanism. One way to separate the two mechanisms is to calculate the dielectric constant (k) using the slope from the log J vs. $V^{1/2}$ plots with the sample thickness (s) and temperature. The current density for each mechanism is given by

$$J_S \propto T^2 \exp\{q[(qV/4\pi\epsilon_o\, ks)^{1/2} - \phi_s]/kT\} \qquad (3.1)$$

$$J_{F-P} \propto (V/s)\exp\, q[(qV\pi\epsilon_o ks)^{1/2} - \phi_{F-P}]/kT\} \qquad (3.2)$$

where q is the electronic charge, ϵ_o the permittivity of free space, ϕ_s the Schottky barrier height, and ϕ_{F-P} the Frenkel-Poole trap well depth both in volts, and k is boltzmann's constant.

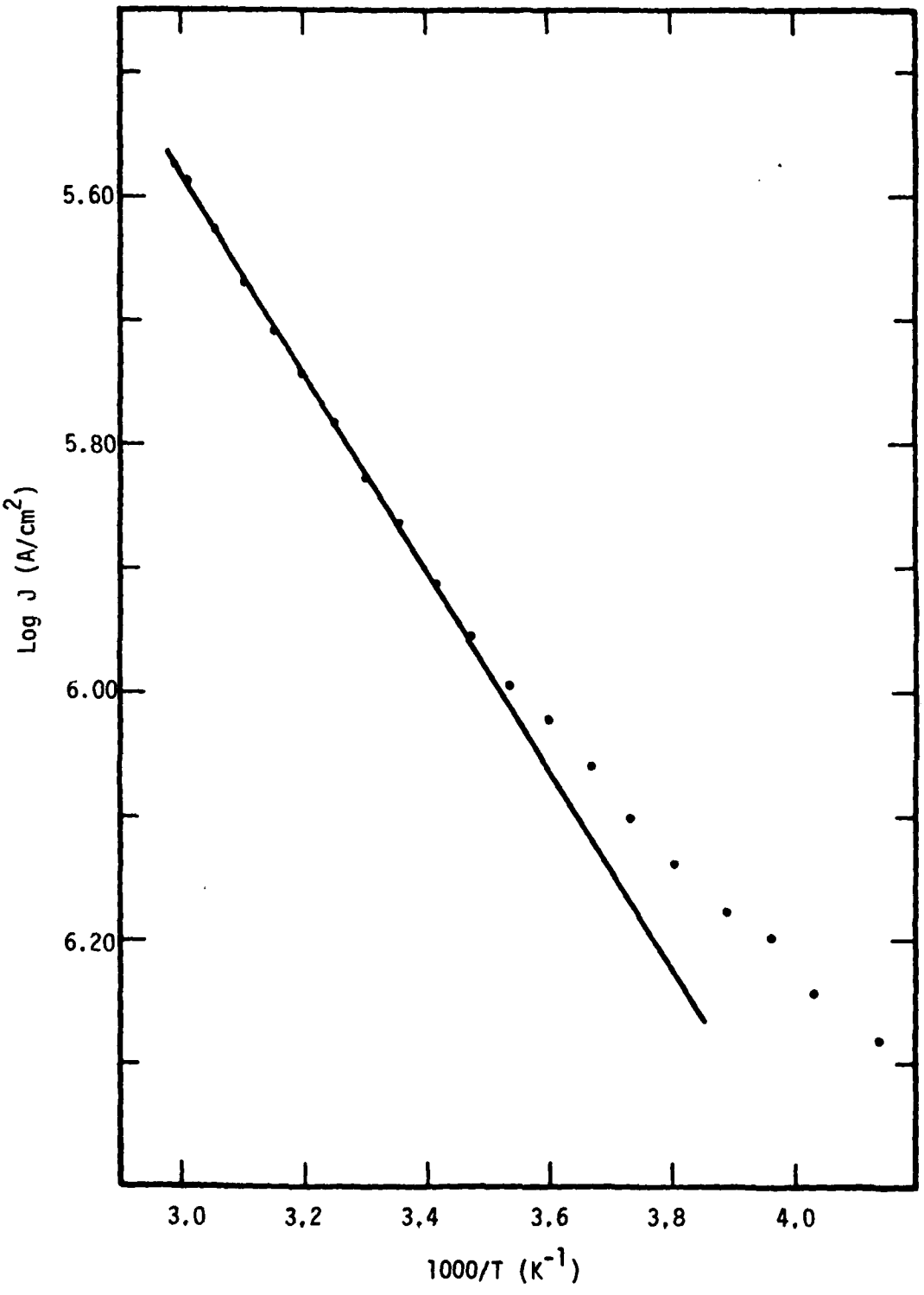

Figure 3.21. Current Density as a Function of Temperature for a 10 w/o Substrate Glass (7 nm) MIM at 0.5 Volt.

In graphing log J vs. $V^{1/2}$, the slope m_v of the linear portion corresponds to

(Schottky) $$2.3\, m_v = \frac{q}{kT}\left(\frac{q}{4\pi\varepsilon_0 k s}\right)^{1/2} \qquad (3.3)$$

(Frenkel-Poole) $$2.3\, m_v = \frac{q}{kT}\left(\frac{q}{\pi\varepsilon_0 k s}\right) \qquad (3.4)$$

For any given thickness, temperature, and corresponding slope, the dielectric constant can be calculated from:

(Schottky) $$k = (q\ 3/4\pi\varepsilon_0 k^2)\ (1/s(2.3\, m_v T)^2)$$

$$= 0.03645/(s(m_v T)^2) \qquad (3.5)$$

or $$k = (q\ 3/\pi\varepsilon_0 k^2)\ (1/s(2.3\, m_v T)^2)$$

(Frenkel-Poole)

$$= 0.1458/(s(m_v T)^2) \qquad (3.6)$$

A dielectric constant was calculated for each data set for each mechanism; for the Frenkel-Poole case the average k was 18 with a standard deviation of 18 percent, and for the Schottky case the average k was 4.5 with a standard deviation of 18 percent. Based on a comparison of these results with the measured dielectric constants (Table III.2) the more likely mechanism for conduction through the glass films is Schottky emission.

To calculate ϕ_s, the Schottky barrier height, the slopes ($m_{1/T}$) of the log J vs. 1000/T data were used along with Eq. 3.1 to yield:

$$\phi_s = (qV/4\pi\varepsilon_0 k s)^{1/2} - \frac{(2.3\times10^3)m_{1/T}k}{q}$$

$$= 1.20(10^{-5})(V/s)^{1/2} - 0.199\, m_{1/T} \qquad (3.7)$$

Averaging the values of ϕ_s calculated from Eq. 3.7 for each data set gave a barrier height of 0.38 volts, which is quite consistant with barrier heights reported for Schottky emission.

3.3 Change Transport Model

Thick film resistor formulations contain an electrically conducting RuO_2 powder and an electrically insulating glass powder. The processing is carried out at temperatures where a continuous glass matrix is formed, and a continuous RuO_2 phase must also form for electrical conduction to occur. The microstructure development model presented in Section 2.7 predicts that there will be a spectrum of neck diameters between RuO_2 particles, varying from sintered necks which approach the size of the initial RuO_2 particles to those in which no sintering has occurred and a glass film still separates the particles. It is the relative numbers and geometric arrangement in the RuO_2 network of the different types of contacts resulting from the varying degrees of sintering that will determine the sheet resistance and TCR of the resistors. One of the goals of this program was to determine the effect of the resistor-substrate interaction on these electrical properties, and to modify the model for charge transport to accommodate this effect.

To model charge transport through a sintered contact between RuO_2 particles, the problem is to develop a relationship for the effective resistivity (ρ_e) of RuO_2 particles of radius r joined by necks of radius x as a function of the bulk resistivity (ρ) and the ratio of neck radius to particle radius (x/r). Previous modeling studies [23] have argued that constriction resistance is dominant factor at values of x/r less than 0.1, and the problem was solved for this case to give:

$$\rho_e = \frac{\pi\rho}{2(x/r)(1-x^2/3r^2)^2} \qquad (\frac{x}{r} < 0.1) \tag{3.8}$$

For values of x/r greater than 0.7 it was argued [23] that a flux tube approximation is appropriate, and the problem was solved for this case to give:

$$\rho_e = \frac{(1 - x/r)^2\rho}{3(x/r)(1 - x^2/3r^2)\ D\ [1 - \cos(\frac{1-x/r}{D})]}$$

$$(\frac{x}{r} > 0.7) \tag{3.9}$$

where $$D = [(1 - x/r)^2 + (1 - x^2/3r^2)^2]^{1/2}$$

From these two boundary conditions, a graphical solution was obtained for F(x/r) in the equation:

$$\rho_e = \rho\ F(x/r) \qquad (0 \leq \frac{x}{r} \leq 1) \tag{3.10}$$

The resistance (R_e) of the RuO_2 in two half particles of radius r joined by a neck of radius x can be obtained [23] from:

$$R_e = \frac{3\rho_e}{\pi r}(1 - x^2/3r^2)^2 = \rho[\frac{G\ (x/r)}{r}] \tag{3.11}$$

Thus, R_e can be calculated for any values of x and r.

The total resistance (R_s) of an individual sintered contact is given by:

$$R_s = R_e + R_b \tag{3.12}$$

where R_b is the resistance due to enhanced electron scattering by the grain boundary formed by sintering of the crystalline particles. The grain

boundary resistance cannot be calculated from first principles, and must be obtained from experimental data. Combining Eqs. 3.11 and 3.12, and the resistivity (ρ) of bulk RuO_2 [23] gives

$$R_s = \frac{\rho_o\ (1 + 5.67\ X\ 10^{-3}\ \theta)}{r}\ G(\frac{x}{r}) + R_b \qquad (3.13)$$

where θ = T-298K and ρ_o is the defect-free resistivity.

The non-sintered contacts, where a thin glass film separates adjacent RuO_2 particles, were modeled by the MIM devices as discussed in Section 3.2. The results of these studies demonstrated that charge transport through the non-sintered contacts near room temperature was by Schottky emission with a barrier height of approximately .38 ev for film thicknesses the order of 7 nm and greater. For thinner films and/or lower temperatures, the barrier height (ϕ_s) decreased until finally a temperature independent, quantum mechanical tunneling mechanism became dominant. The resistance of these two types of contacts can be represented by:

(Schottky) $$R_{sc} = (A/T^2)\exp(\phi_s/kT) \qquad (3.14)$$

(tunneling) $$R_t = R_t \qquad (3.15)$$

where ϕ_s will have a distribution of values from 0 to .38 ev, and A is a constant.

In order to develop a model for conduction through the RuO_2 network in a thick film resistor, it is assumed that the network is made up of units which have a resistance (R_u) given by:

$$R_u = R_u(n_s R_s,\ n_t R_t,\ R_{sc}) \qquad (3.16)$$

where n_s is the ratio of the number of sintered contacts to Schottky contacts, and n_t is the ratio of the number of tunneling contacts to Schottky contacts. Several possible series-parallel combinations of n_sR_s, n_tR_t and R_{sc} could be selected to represent the unit resistance, but none of these could be solved in closed form because of the unknown distribution of barrier heights which enters into R_{sc}. However, the relative behavior of the parameters of interest can be determined from the temperature dependence of R_u as discussed in the next paragraphs.

The total RuO_2 network in a resistor is made up of a large number of the resistance units arranged in various series and parallel combinations, and the complexity of this arrangement makes modeling of the measured resistance impossible. However, for a resistance, R, made up of <u>any</u> series and parallel combination of unit resistances, R_u, it can be shown that:

$$\frac{1}{R}\frac{dR}{dT} = \frac{1}{R_u}\frac{dR_u}{dT} \tag{3.17}$$

Therefore, the variation with temperature of the unit resistance can be determined from experimental data such as those given in Section 3.1

The relative resistances plotted in Figs. 3.1-3.4 are well represented by a parabolic equation of the form:

$$\frac{R}{R_o} = 1 + a\theta + b\theta^2 \tag{3.18}$$

Since

$$\frac{1}{R_u}\frac{dR_u}{dT} = \frac{1}{R}\frac{dR}{dT} = \frac{1}{(R/R_o)}\frac{d(R/R_o)}{dT} \tag{3.19}$$

then

$$\frac{1}{R_u}\frac{dR_u}{dT} = \frac{a + 2b\theta}{1 + a\theta + b\theta^2} \qquad (3.20)$$

The 20 data sets plotted in Figs. 2.1-3.4 were analyzed according to Eq. 3.18, and the TCR at room temperature was calculated from Eq. 3.20. The results of these calculations are plotted in Fig. 3.22 as a function of firing time for the four resistor glass compositions. There are some striking similarities between the curves of Fig. 3.22 and those of Fig. 2.16, which show the amount of substrate dissolved in the glass as a function of firing time. The solid lines of Fig. 2.16, which are for a firing time of 760°C, show that there is a large difference in glass composition between the standard glass and a 5 w/o substrate glass during the first few minutes of firing, but the curves converge rapidly, and beyond 10 minutes there is little difference in the glass compositions. The identical behavior is shown by the TCR's of the standard and 4 w/o substrate glass resistors in Fig. 3.22. Identical behavior is also seen in Figs. 2.16 and 3.22 for the composition and TCR of the resistor glass which initially contained 10 w/o substrate; the amount of dissolved substrate is always higher and the TCR is always more negative, and both parameters show a linear increase with firing time.

The strong correlation between the extent of the resistor-substrate interaction and the temperature dependence of the unit resistance means that n_s and n_t in Eq. 3.16 will be reduced, and the distribution of barrier heights in R_{sc} (Eq. 3:14) will be shifted to higher values. The more constant the glass composition, the more constant the parameters in the model equation become.

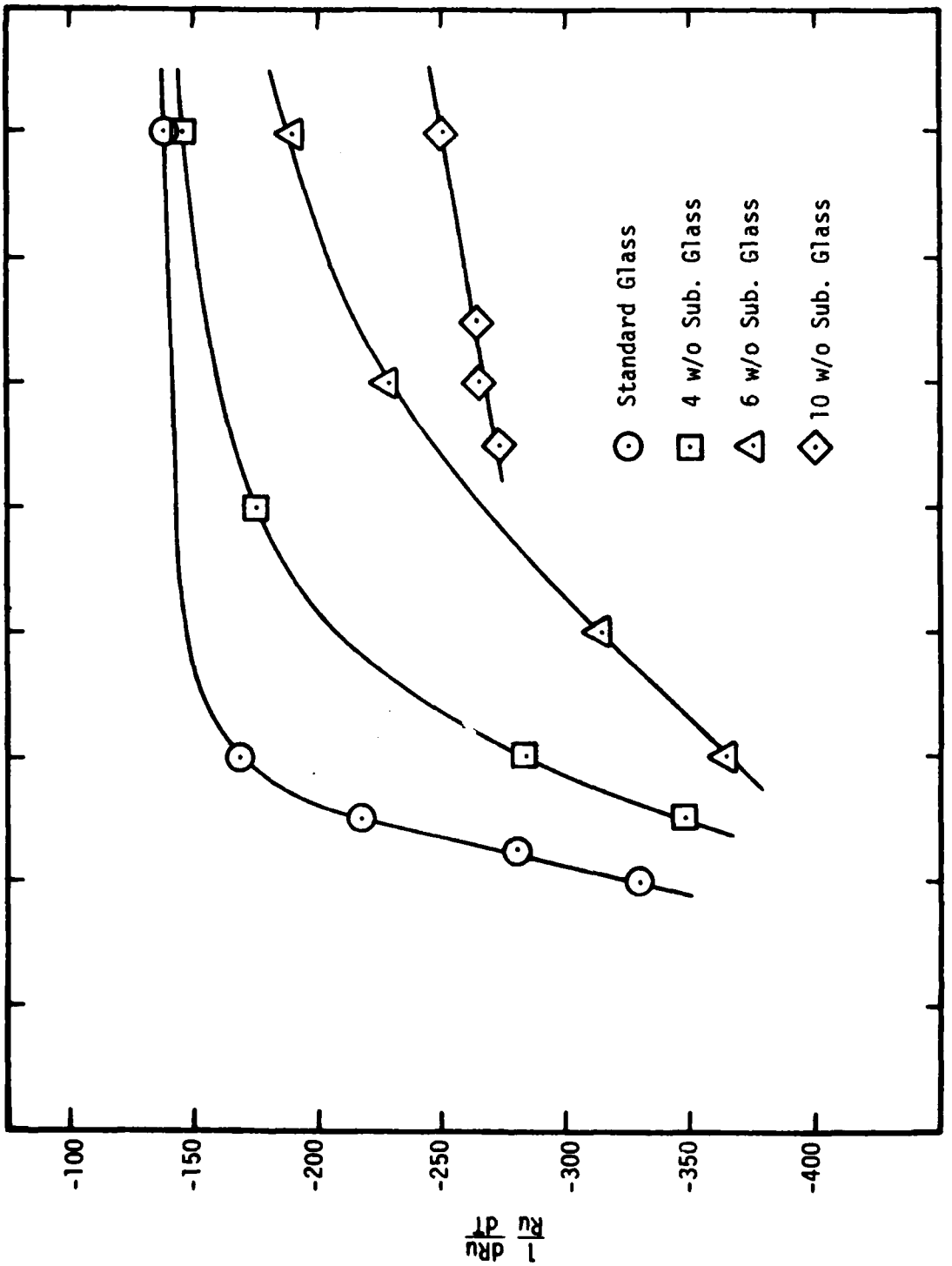

Figure 3.22. TCR at 25°C as a Function of Firing Time at 800°C for Four Resistor Glass Compositions.

4. SUMMARY AND RECOMMENDATIONS

The major findings of this research program can be summarized as follows:

1. The amount of alumina substrate which dissolves into the glass during processing of a thick film resistor is a very strong function of temperature. For 15 minutes at maximum temperature, the final glass composition will contain 18 w/o dissolved substrate at 920°C, but less than 1 w/o dissolved substrate at 640°C.
2. The isothermal viscosity of the resistor glass increases by a factor of 20 or more as the amount of dissolved substrate goes from 0 to 14 w/o, and the temperature dependence of the viscosity also increases.
3. The high temperature surface tension of the resistor glass decreases by 20% as the amount of dissolved substrate goes from 0 to 14 w/o.
4. The high temperature density of the resistor glass decreases by 10% as the amount of dissolved substrate goes from 0 to 14 w/o.
5. The minor constituents (SiO_2, MgO, CaO, and Fe_2O_3) in the alumina substrate have a larger influence on raising the viscosity, and on lowering the surface tension and density than their concentrations would suggest.
6. The time to reach equivalent degrees of sintering and ripening of RuO_2 in the resistor glass increases by a factor of 5 as the amount of dissolved substrate goes from 0 to 14 w/o.

7. For equivalent resistor compositions and firing conditions, the sheet resistance increases and the TCR decreases as the amount of substrate dissolved in the resistor glass increases.
8. As the amount of substrate dissolved in the resistor glass increases, the radius of the sintered neck between adjacent RuO_2 particles is smaller for equivalent firing conditions, which causes an increase in resistance of individual sintered contacts in the RuO_2 network.
9. Charge transport across non-sintered contacts in the RuO_2 network was shown to occur by Schottky emission for film thicknesses of 7 nm and greater. As the film thickness decreases, the Schottky barrier height decreases until finally a temperature independent, quantum mechanical tunneling mechanism becomes dominant.
10. The primary modifications made to the microstructure development model in order to accommodate the effect of substrate dissolved in the resistor glass were to the kinetic equations for glass densification and bubble release, and a minor modification was made to the equation for RuO_2 sintering kinetics.
11. The modifications of the charge transport model which were required in order to accommodate the effect of substrate dissolved in the resistor glass were to shift the distribution of Schottky barrier heights to higher values, and to increase the density of non-sintered contacts relative to sintered contacts in the unit resistances which make up the RuO_2 network.

Based on the results of this study, the following recommendations are made in order to keep changes in electrical properties of thick film

resistors due to the resistor-substrate interaction within the range expected from other process variables.

1. The chemical composition of the substrate should be subjected to quality control. After a nominal composition is agreed on between the user and the substrate manufacturer, the lot-to-lot variation should be less than ± 0.1% for Al_2O_3 and less than ± 10% for any minor constituent that constitutes more than 0.1% of the nominal composition.
2. For nominal substrate compositions containing less than 99% Al_2O_3, the surface composition should also be subjected to the same quality control as detailed in Recommendation No. 1 for the bulk composition.
3. The thick film paste manufacturers can minimize the detrimental effects of the resistor-substrate interaction by using glass frit compositions which contain 10% Al_2O_3. This would be of particular help for hybrid circuits where refire of resistors is required during fabrication.

5. REFERENCES

1. R. W. Vest, "The Effects of Substrate Composition on Thick Film Circuit Reliability," Final Technical Report on Contract No. N00019-76-C-0354, 28 February 1977.

2. R. W. Vest, "The Effects of Substrate Composition on Thick Film Circuit Reliability," Final Technical Report on Contract No. N00019-77-C-0327, 28 February 2978.

3. R. W. Vest, "The Effects of Substrate Composition on Thick Film Circuit Reliability," Final Technical Report on Contract No. N00019-78-C-0236, 28 February 1979.

4. L. Shartis and S. Spinner, "Viscosity and Density of Molten Optical Glasses," J. Res. Nat. Bur. Std., 46, 176 (1951).

5. G. S. Fulcher, "Analysis of Recent Measurements of the Viscosity of Glasses," J. Amer. Ceram. Soc., 8, 339 (1925).

6. G. W. Morey, "Properties of Glass," Amer. Chem. Soc., Monograph No. 77, Reinhold Publishing Corp., New York, N. Y. (1938).

7. A. Abou-El-Azm and H. A. El-Batal, "Studies on the Softening Points of Some Borate and Cabal Glasses, and Glasses Containing High Proportions of Lead Oxide in Relation to Their Structure," Phys. Chem. Glass, 10, 159 (1969).

8. L. Shartis, S. Spinner, and A. W. Smock, "Surface Tensions and Compositions in the Systems $PbO-B_2O_3$ and $PbO-SiO_2$," J. Amer. Ceram. Soc., 31, 23 (1948).

9. A. Prabhu, G. L. Fuller, R. L. Reed, and R. W. Vest, "Viscosity and Surface Tension of a Molten Lead Borosilicate Glass," J. Amer. Ceram. Soc., 58, 144 (1975).

10. H. F. Shermer, "Surface Tension of Molten Glasses in the System Barium Oxide-Boric Oxide-Silica," J. Res. NBS, 56, 155 (1956).

11. G. W. Parmelee and C. G. Harman, "The Effect of Alumina on the Surface Tension of Molten Glass," J. Amer. Ceram. Soc., 20, 224 (1937).

12. S. Akhtar and M. Cable, "Some Effects of Atmosphere and Minor Constituents on the Surface Tension of Glass Melts," Glass Technol., 9, 145 (1968).

13. S. Brunauer, P. H. Emmett, and E. Teller, "Adsorption of Gas in Multimolecular Layers," J. Amer. Chem. Soc., 60, 309 (1938).

14. G. W. Greenwood, "The Growth of Dispersed Precipitates in Solutions," Acta Met., 4, 243 (1956).

15. I. M. Lifshitz and V. V. Slyozov, "The Kinetics of Precipitation from Supersaturated Solid Solutions," J. Phys. Chem. Solids, 19, 35 (1961).

16. C. Wagner, "Theorie der Alterung von Niederschlägen durch Umlosen (Ostwald-Reifung)," Z. Electrochemic, 65, 581 (1961).

17. H. Fischmeister and G. Grimvall, "Ostwald Ripening - A Survey," Mater. Sci. Res., 6, 119 (1973).

18. J. White (Ed. G. H. Stewart), "Science of Ceramics," Vol. II, Academic Press, London (1964).

19. A. Prabhu and R. W. Vest, "Investigation of Microstructure Development in RuO_2-Lead Borosilicate Glass Thick Films," Mater. Scie. Res., 10, 399 (1975).

20. J. W. Gibbs, "Scientific Papers," Vol. I, Dover, New York, N. Y. (1961).

21. A. R. Cooper, Jr., and W. D. Kingery, "Dissolution in Ceramic Systems: I, Molecular Diffusion, Natural Convection, and Forced Convection Studies of Sapphire Dissolution in Calcium Aluminum Silicate," J. Amer. Ceram. Soc., 47, 37 (1964).

22. R. A. Greenkorn and D. P. Kessler, "Transfer Operations," McGraw-Hill, New York, N. Y. (1972).

23. R. W. Vest, "Conduction Mechanisms in Thick Film Microcircuits," Final Technical Report, Purdue Research Foundation Grant Nos. DAHC-15-17-G7 and DAHC-15-73-G8, ARPA Order No. 1642, December 1975.